

DESIGN OF A RECONNAISSANCE AND SURVEILLANCE ROBOT

A THESIS SUBMITTED TO
THE GRADUATE SCHOOL OF NATURAL AND APPLIED SCIENCES
OF
MIDDLE EAST TECHNICAL UNIVERSITY

BY

ERMAN ÇAĞAN ÖZDEMİR

IN PARTIAL FULFILLMENT OF THE REQUIREMENTS
FOR
THE DEGREE OF MASTER OF SCIENCE
IN
MECHANICAL ENGINEERING

AUGUST 2013

Approval of the thesis:

DESIGN OF A RECONNAISSANCE AND SURVEILLANCE ROBOT

submitted by **ERMAN ÇAĞAN ÖZDEMİR** in partial fulfillment of the requirements for the degree of **Master of Science in Mechanical Engineering Department, Middle East Technical University** by,

Prof. Dr. Canan Özgen
Dean, Graduate School of **Natural and Applied Sciences**

Prof. Dr. Süha Oral
Head of Department, **Mechanical Engineering**

Prof. Dr. Eres Söylemez
Supervisor, **Mechanical Engineering Dept., METU**

Examining Committee Members:

Prof. Dr. Kemal İder
Mechanical Engineering Dept., METU

Prof. Dr. Eres Söylemez
Mechanical Engineering Dept., METU

Prof. Dr. Kemal Özgören
Mechanical Engineering Dept., METU

Ass. Prof. Dr. Buğra Koku
Mechanical Engineering Dept., METU

Alper Erdener, M.Sc.
Project Manager, Unmanned Systems, ASELSAN

Date: 29/08/2013

I hereby declare that all information in this document has been obtained and presented in accordance with academic rules and ethical conduct. I also declare that, as required by these rules and conduct, I have fully cited and referenced all material and results that are not original to this work.

Name, Last name: Erman aęan ZDEMİR

Signature:

ABSTRACT

DESIGN OF A RECONNAISSANCE AND SURVEILLANCE ROBOT

Özdemir, Erman Çağın

M.Sc., Department of Mechanical Engineering
Supervisor: Prof. Dr. Eres Söylemez

August 2013, 72 pages

Scope of this thesis is to design a man portable robot which is capable of carrying out reconnaissance and surveillance missions. Due to design needs, the study is mainly focused on throw impact damage mitigation and hopping potential with carbon dioxide gas. Also, electromechanical design of the robot is carried out according to the design specifications.

Keywords: Robot, Reconnaissance, Surveillance, Hopping

ÖZ

BİR KEŞİF VE GÖZETLEME ROBOTUNUN TASARIMI

Özdemir, Erman Çağın

Yüksek Lisans, Makina Mühendisliği Bölümü
Tez Yöneticisi: Prof. Dr. Eres Söylemez

Ağustos 2013, 72 sayfa

Bu tezin kapsamı bir insanın taşıyabileceği boyutlarda bir keşif ve gözetleme robotunun tasarımıdır. Tasarım gerekleri sebebi ile tezin odağı özellikle atış şokundan gelecek hasarı en aza indirmek ve karbondioksit gazı ile zıplama potansiyelinin araştırılmasıdır. Ayrıca robotun elektromekanik tasarımı da istelere uygun olacak şekilde yapılmıştır.

Anahtar Kelimeler: Robot, Keşif, Gözetleme, Zıplama

To My Parents

ACKNOWLEDGMENTS

The author wishes to express his deepest gratitude to his supervisor Prof. Dr. Eres Söylemez for his guidance, advice, criticism, encouragements and insight throughout the research.

The author is also grateful to ASELSAN Inc. for the all the support the company provided.

The author would like to thank Ezgi Berfin Ünsal, without her support the author would not be in this point now.

The author also offers special thanks to the his colleagues Deniz Mutlu, Uğur Doğan Gül and Çiğdem Çakıcı Özkök for their help throughout the thesis.

Finally, the author thanks to Middle East Technical University for educating him.

TABLE OF CONTENTS

ABSTRACT	iv
ÖZ.....	v
ACKNOWLEDGMENTS.....	vii
TABLE OF CONTENTS	viii
LIST OF FIGURES	xi
LIST OF SYMBOLS AND ABBREVIATIONS.....	xiv
CHAPTERS	
1. INTRODUCTION	1
1.1. Motivation.....	1
1.2. Technology Assesment.....	2
1.2.1. Commercial Microbots.....	3
1.2.1.1. iRobot FirstLook 110	3
1.2.1.2. Recon Robotics Scout XT	3
1.2.1.3. MacroUSA Armadillo	4
1.2.1.4. Boston Dynamics Sand Flea.....	4
1.2.1.5. Comparison of the Commercialized Robots	6
1.2.2. Robots Which Are On Their Development Phases	6
1.2.2.1. Mini-Whegs	6
1.2.2.2. Jollbot	7
1.2.2.3. Shape Memory Alloy Based Robots.....	8

1.2.2.4. MSU Jumper	10
1.2.2.5. Mowgli.....	11
1.2.2.6. Grillo.....	12
1.2.2.7. MIT Microbot	12
1.3. Design Specifications	13
1.4. Overview of the Thesis.....	13
2. LOCOMOTION SYSTEM	15
2.1. Introduction.....	15
2.2. Cone Wheel Design Concept.....	17
2.3. Detailed Design of the Cone Wheel System	19
2.4. Parameter Selection for the Wheel	21
2.5. Skid Steering And Timing Belt Transmission	22
2.6. Results of the Manufactured Locomotion System	22
3. HOPPING SYSTEM.....	26
3.1. Introduction.....	26
3.2. Preliminary Calculations for Jumping with a Piston Cylinder Arrangement	27
3.2.1. Using CO ₂ Gas for Jumping	28
3.2.2. Preliminary Calculations with CO ₂ as source.....	30
3.3. Detailed Model of the CO ₂ system.....	31
3.3.1. CO ₂ Cartridge	32
3.3.2. Orifice	32
3.3.3. Actuator	34
3.4. Matlab Model of the System	38
3.5. Mechanism to Pierce the Cartridge.....	44
3.5.1. Screw Part of Piercing Mechanism	44
3.5.2. Slider Crank Part of Piercing Mechanism.....	46
3.5.3. Actual Piercing Mechanism	47

3.6. Tilt Mechanism	49
3.6.1. Analysis of Tilting Mechanism	50
3.6.2. Actual Tilt Mechanism.....	51
3.7. Results of the Overall Hopping System	53
4. ELECTRONICS SYSTEM	55
4.1. Introduction.....	55
4.2. Microcontroller And Wireless Communication Board.....	55
4.3. Battery.....	57
4.4. Motor Drivers.....	58
4.5. Compass Unit.....	58
4.6. Software	59
4.6.1. Graphical User Interface for Test Purposes	59
4.7. Remarks	60
5. CONCLUSION AND RECOMMANDATIONS	61
5.1. Conclusions and Recommendations	61
5.2. Future Work and Recommendations.....	63
REFERENCES	64
APPENDIX: SELECTED PRODUCTS.....	67
A.1. Linear Bearings of the Cone Wheel and Piercing Mechanism ...	67
A.2. Wave Spring of the Cone Wheel.....	68
A.3. Rabbit 5400w Microcontroller Board Datasheet	69
A.4. Lipo Battery	70
A.5. Motor Driver Datasheet	71
A.6. Ocean Server OS5000-S Compass Datasheet	72

LIST OF FIGURES

Figure 1-1: AMCB UGV 2011 Marine Requirements Capability Plan	2
Figure 1-2: Conceptual Drawing of a Small Robot Sent Inside a Collapsed Building [5]	2
Figure 1-3: iRobot FirstLook 110 performing a mission with IDAC accessory	3
Figure 1-4: Recon Robotics Scout XT Throwable Robot	4
Figure 1-5: MacroUSA's Armadillo shown with Additional Flipper and Track Options	4
Figure 1-6: Image of Boston Dynamics Sand Flea	5
Figure 1-7: Sand Flea Positioning Itself Before A Jump	5
Figure 1-8: Family of Mini-Whlegs	7
Figure 1-9: MiniWhlegs Robot during its Jump	7
Figure 1-10: High speed camera images illustrating the jumping performance of Jollbot; (a) Resting state of Jollbot (b) 1.44 s later, Jollbot is ready to jump (c) 0.24 s later, (d) 0.22 s later Jollbot hits the ground and absorbs impact energy in the slight compressing of the sphere.	8
Figure 1-11:Flea Like Jumping Mechanism – a)Flexor muscle is contracted. b)Extensor is pulled beyond Joint1 and lower femur is stopped by stopper. c)Trigger muscle is pulled, changing the torque direction of the extensor muscle d)All Energy is released and jumping occurred.....	9
Figure 1-12: Flea-Like Robot Preparing For a Jump.....	9
Figure 1-13: SMA Hoop Structure for Jumping	10
Figure 1-14: MSU Jumper a) Prototype b)Solid Model	10
Figure 1-15: Bi-Articulated Jumping Mechanism of the Mowgli.....	11
Figure 1-16: Mowgli Performing a Jump on a Chair	11
Figure 1-17: Schematic of the Jumping Mechanism of the Grillo	12
Figure 1-18: MIT Microbot with Dielectric Polymer Performing a Jump	12
Figure 1-19: Block Diagram of the Robot.....	14
Figure 2-1: Resilience in wheel is achieved through curved arches in this iRobot Negotiator	16
Figure 2-2: Resilient Wheel with Curved Arches as Springs and Dampers inside the Wheel [30]	16
Figure 2-3: Two Wheel configurations developed for Boston Dynamics Sand Flea Wheels. On the left wheel is made out of soft foam and right shows the final wheel from polyurethane.	17
Figure 2-4: Cone Wheel Concept, left sides shows sketches and right shows the 3D model; on top a) natural state of the wheel can be seen, whereas part b) depicts deflected state is on the right	18
Figure 2-5: Spline Shaft Alternative, which would outperform key and linear bushing [Courtesy of Thomson Linear].....	19
Figure 2-6: Free Body Diagram of the Cone Wheel	19
Figure 2-7: Cone Design Angle vs. Required Spring Strength and Spring Compression Length	21
Figure 2-8: Locomotion System of the Robot, Showing the wheels, bearings, belt and pulleys. Wheel taken from the “dumbbell” is left wheel in the picture.	22
Figure 2-9: Shock response of the 3m Drop-down test on robot	24
Figure 2-10: Cone Wheel shown in natural state in top and deflected state on bottom.....	24
Figure 2-11: Marks of wear on the cone wheel	25
Figure 3-1: Boston Dynamics Sand Flea Hopping System Using Combustion	26

Figure 3-2: Sketches demonstrate the phases of hopping; a) At initial condition piston is at the end of cylinder, b) Gas pressure is applied and piston accelerates, c) Piston collides with ground and kinetic energy of piston passes to whole robot, d) Robot jumps with the kinetic energy	27
Figure 3-3: Typical CO2 cartridges found on the market, many seen with black foams on them to avoid frostbite	29
Figure 3-4: CO2 Triple Point Graph [32].....	29
Figure 3-5: CO2 Vapor Pressure versus Temperature	30
Figure 3-6: Theoretical Jumping Heights with CO2 with a Cylinder stroke of 50 cm ³	30
Figure 3-7: Schematic States of the Elements	31
Figure 3-8: Matlab Model of the Orifice.....	33
Figure 3-11: Ideal Gas Law Subsystem of the Actuator	35
Figure 3-12: Rod Mechanics Subsystem of the Actuator	35
Figure 3-9: First Law of Thermodynamics Subsystem of the Actuator.....	36
Figure 3-10: Matlab Model of the Actuator	37
Figure 3-13: Overall Matlab Model of the System	38
Figure 3-14: Measurement of the Maximum Possible Orifice Area of the 12g CO2 cartridge	38
Figure 3-15: Pressure in the cylinder vs. time graph for the base run	39
Figure 3-16 Temperature in the cylinder vs. time graph for the base run.....	40
Figure 3-17: Acceleration, Speed and Position of the Piston vs. Time	40
Figure 3-18: Orifice Diameter vs. Robot Jump Height.....	41
Figure 3-19: Initial Cartridge Temperature versus Piston Exit Velocity and the Robot Jump Height	42
Figure 3-20: Piston Diameter versus Piston Exit Velocity at Various Stroke Lengths and 2.8mm Orifice Diameter	43
Figure 3-21 Piston Diameter versus Piston Exit Velocity at Various Stroke Lengths and 2.8mm Orifice Diameter	43
Figure 3-22: Overall CAD Drawing of the Piercing Mechanism	44
Figure 3-23: Cut-Away Section of the Screw Part of the Piercing Mechanism	45
Figure 3-24: Due to Shape of Hammer, Detent Ball Exerts a Force in the Desired Direction	45
Figure 3-25: Skeleton Diagram of the Slider Crank Mechanism.....	46
Figure 3-26: Free Body Diagrams of the Link 2 and Link 3	47
Figure 3-27: Striker Stroke and Multiplication Factor vs. Crank Angle.....	48
Figure 3-28: Components of the Manufactured Piercing Mechanism	48
Figure 3-29: Two Possible Design Concepts for Providing Thrust a) Rotating Piston with Respect to Ground b) Rotating Robot with Respect to Ground.....	49
Figure 3-30: Skeleton Diagram of the Tilting Mechanism	50
Figure 3-31: Free Body Diagrams of a) Leg and b) Robot Body	50
Figure 3-32: CAD drawing of the Tilt Mechanism	52
Figure 3-33: Tilt Mechanism in Action during Tests	52
Figure 3-34: Measurement of the Weight of the Robot	53
Figure 3-35: Figure Showing the Actual Jump of the Robot at its Highest Point.....	54
Figure 3-36: Fractured Gears of the Left Tilt Motor's Gearbox	54
Figure 4-1: Rabbit RCM5400w Board	55
Figure 4-2: Cabling Work Done at the Back Side of the Prototyping Board	56
Figure 4-3: Mounting the PCB with the O-Rings [36]	56
Figure 4-4: Li-Po Battery used in the Robot	57
Figure 4-5: Balanced Battery Charger	57
Figure 4-6: Schematic of the Motor Driver Breakout Board.....	58
Figure 4-7: Ocean Server OS-5000S Compass Unit	59
Figure 4-8: Placement of the Compass Unit inside the Robot.....	59
Figure 4-9: A Screenshot of the GUI Designed for Testing the Robot.....	60

Figure 5-1: Main reason behind length L was the author's inability to develop his own linear bearings and his inability to find suitable tires for a smaller wheel	62
Figure 5-2: Main joints of the hopping system are supported with liquid seal.....	62
Figure 5-3: Heaters could be used to reliably jump at cold temperatures	63
Figure A-1.1: Selected Linear Bearing of the Wheel	67
Figure A-1.2: Selected Linear Bearing for the Hammer Mechanism	67
Figure A-2: Selected Wave Spring of the Cone Wheel [40]	68
Figure A-3: Datasheet of the Rabbit RCM5400w	69
Figure A-4: Datasheet of the Lithium Polymer Battery from the THK Store	70
Figure A-5: Datasheet of Texas Instruments DRV8833	71
Figure A-6: Specifications of the OS5000-S	72

LIST OF SYMBOLS AND ABBREVIATIONS

SYMBOLS

g	:	Gravitational Acceleration
a_i	:	Related Link Length
P_0	:	Ambient Pressure
T_0	:	Ambient Temperature
P_A	:	Pressure in Cylinder
m_{piston}	:	Mass of Piston
m_{robot}	:	Mass of Robot
P_S	:	Supply Pressure of the Cartridge
T_{OR}	:	Temperature of the gas exiting the orifice
\dot{m}	:	Mass flow rate from the orifice to the cylinder
V_A	:	Volume of the pressurized side of the cylinder
$V_{0,A}$:	Initial (dead) volume of the cylinder
x	:	Position of piston inside the cylinder
f	:	Dry friction between the cylinder and piston
c	:	Viscous friction coefficient between cylinder and piston
α	:	Heat transfer coefficient of the cylinder
A_{OR}	:	Orifice Area (Pierced area of the cartridge)
s	:	Stroke Length of the Piston

ABBREVIATIONS

UGV	Unmanned Ground Vehicle
UAV	Unmanned Aerial Vehicle
AMCB	Army Marine Corps Board
OCU	Operator Controller Unit
FOV	Field of View
IDAC	Integrated Deployment and Camera
THK	Türk Hava Kurumu
CO ₂	Carbon Dioxide
DEA	Dielectric Elastomer Actuators

CHAPTER 1

INTRODUCTION

1.1. Motivation

With the advance of the robotic technology, small scale robots started to find use for reconnaissance and surveillance missions in two new fields; military operations and urban search and rescue operations.

With the current technology, land based unmanned ground vehicles (UGV) are preferred for these operations rather than their rivals unmanned aerial vehicles (UAV). UGV's can operate longer than UAV's as they consume less energy, since UAV's consume considerable amount of energy even while hovering. Besides that, UGV's are less silent and harder to notice compared to UAV's. Moreover, in an urban area, especially inside a building, UGV's are much easier to operate than UAV's. For these reasons, scope of this thesis is limited to land based mobile robots.

In military operations, the way to stop soldiers being ambushed or falling into traps during battle is to help them look before they leap. When equipped with remote control robots which can look around dangerous corners, explore dark tunnels or be first into caves, armed forces will know the level of threat and make better decisions on the field. Also, with the current state of art warfighters can share the visual feedback from the robot with the command center, thus enable better tactical command and more integrated responses over the missions.

For the last few years, armed forces around the world are quite interested in such robots. Recon Robotics' Scout XT, iRobot's 110 First Look, MacroUSA's Armadillo V2 Micro Unmanned Ground Vehicle, and QinetiQ North America's Dragon Runner are all "field tested" in Afghanistan [1]. Among the tested equipment's 1100, quite a huge number for a still a developing field, Scout XT was ordered by U.S. Army Rapid Equipping Force for 13.9 Million \$ in 2012 [2]. Also, U.S. Army Marine Corps Board (AMCB) also announced that microbots are in their current and future plans of unmanned ground vehicles [3] as shown in Figure 1-1 which demonstrates that there will be a demand in similar robots over the following decades.

In addition to these military reconnaissance missions, these robots are also becoming more and more accepted in urban operations as well. Concept of sending a small robot in collapsed buildings to search for humans under the debris is gaining popularity and related schematic sketch is shown in Figure 1-2 . Removing the ruins takes huge amount of time however small robots can be used to quickly scan the disaster site and inspect the traces so that the rescue operations would be more targeted [4].

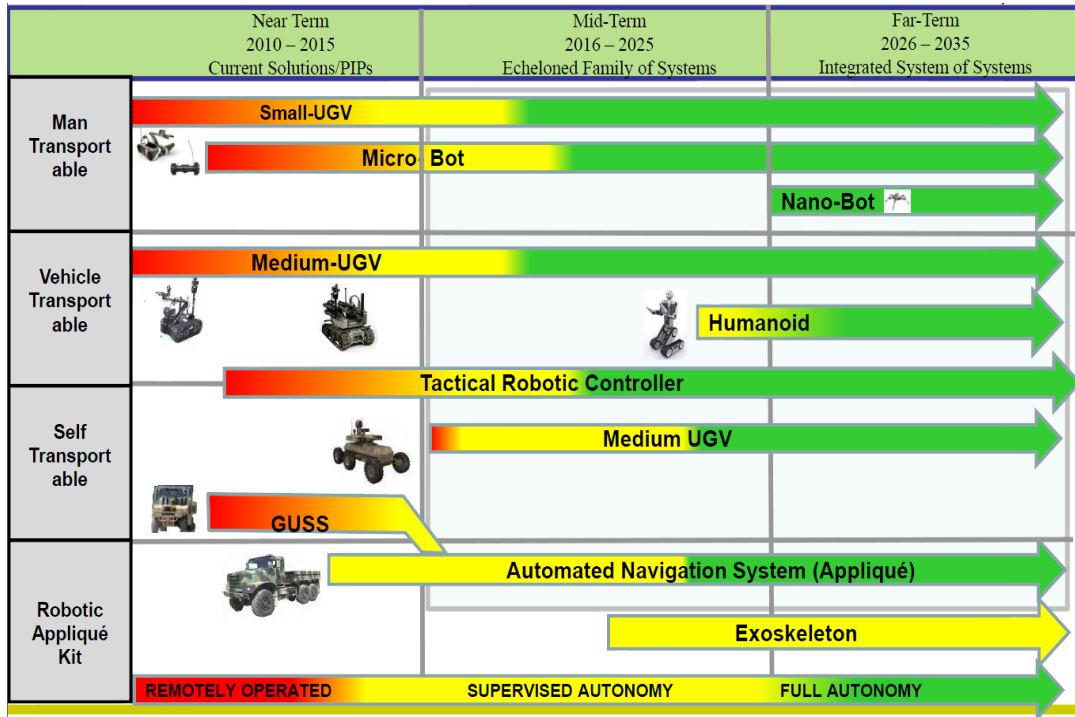


Figure 1-1: AMCB UGV 2011 Marine Requirements Capability Plan

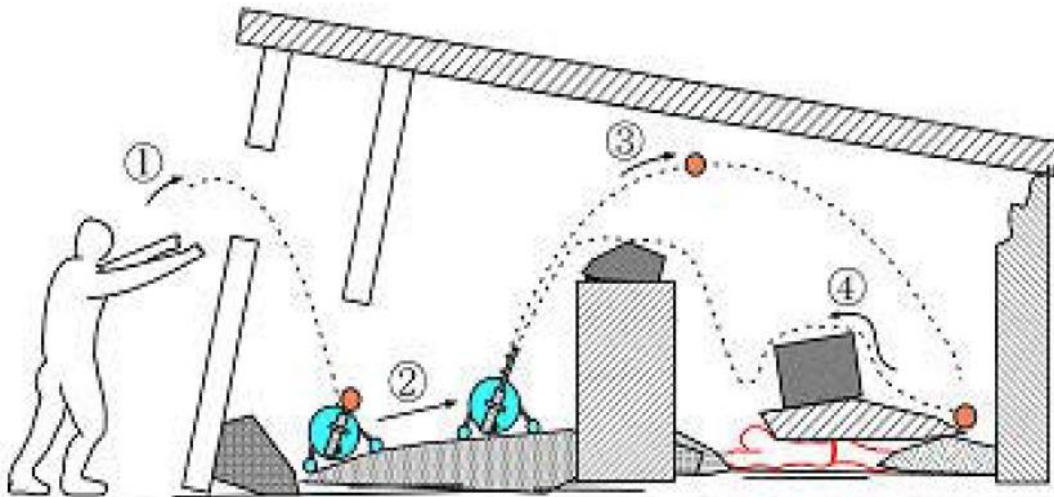


Figure 1-2: Conceptual Drawing of a Small Robot Sent Inside a Collapsed Building [5]

1.2. Technology Assessment

In this part, current state of art in man portable reconnaissance and surveillance robots is investigated. When looking into these robots, jumping ability is not taken as a must in currently available robots. There are also a few commercial robots available such as iSnoop [6] or Toughnot [7] and which are not very popular and somewhat based upon the robots presented here.

1.2.1. Commercial Microbots

This new emerging robotic market is currently controlled by the following robots. Summary of their capabilities are given in 1.2.1.5. Some of the robots presented here, also have low-cost models with less attributes, and they are not mentioned in this context.

1.2.1.1. iRobot FirstLook 110

Successful robotics firm iRobot was one of the pioneers of the throwable robot, with their FirstLook 110 which can be seen in Figure 1-3. FirstLook 110 has become a commercial success awarding iRobot 1.5M \$ contract from the U.S. Army after the field tests in Afghanistan. [8] The robot features 4 cameras including a Pan-Tilt-Zoom to perfectly fulfill the expectations in surveillance missions. This articulated tracked robot has no jumping facilities yet it has flippers to overcome obstacles up to 175 millimeters. Although the product is quite new, the firm's patent about the product has been there for the last 10 years, and the patent explains the precautions for impact resistance, dirt and traction [9]. Main disadvantages of this robot are its relatively higher cost and incapability of jumping. Also robot has much lower survival rate at drop down tests than its competitors.



Figure 1-3: iRobot FirstLook 110 performing a mission with IDAC accessory

1.2.1.2. Recon Robotics Scout XT

Scout robot was developed as a result of DARPA funded research in University of Minnesota, and the success of the research lead to the foundation of Recon Robotics Company. Many types of the robot were developed during 2000s, including the ones which can jump [10]; having spoked wheels or a hook [11].



Figure 1-4: Recon Robotics Scout XT Throwable Robot

1.2.1.3. MacroUSA Armadillo

Quite simple, yet effective Armadillo has incredible payload capacity (3kg) and creates perfect situational awareness with its 360° camera coverage but this robot can't jump or get past any obstacle. Nevertheless, MacroUSA has completed over 5000 orders of Armadillo over recent years. [12] Also, a new model "Beetle" which has almost same functionalities as Armadillo but smaller in size is developed. In addition to these, company is also developing a new model, "Stingray" to be used by navy for boarding operations in maritime applications, which is merely a copy of Armadillo but suitable for sea and ocean applications. [13]

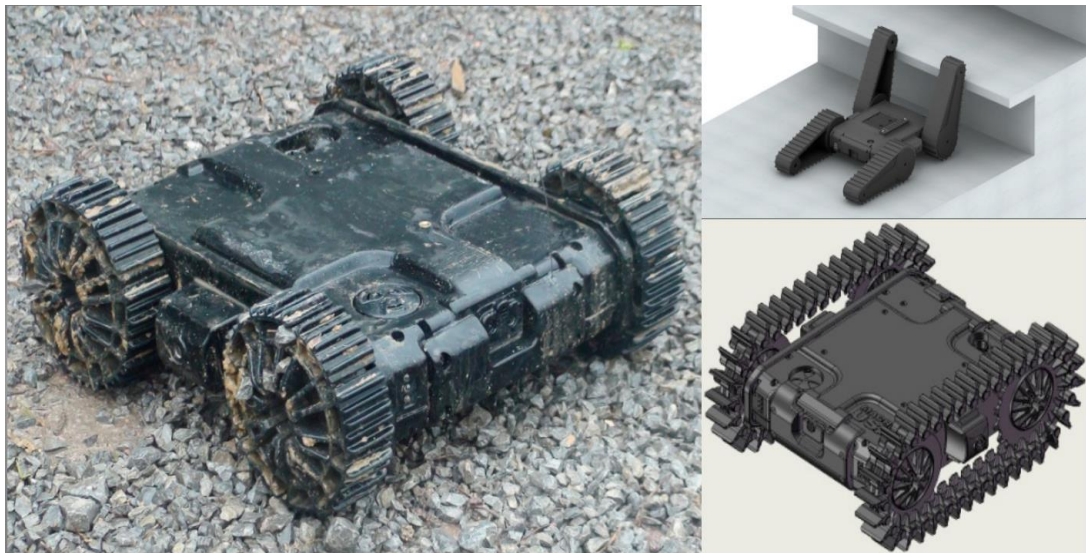


Figure 1-5: MacroUSA's Armadillo shown with Additional Flipper and Track Options

1.2.1.4. Boston Dynamics Sand Flea

Famous robotics firm Boston Dynamics has released their new robot "Sand Flea" in March 2012 which shows remarkable capabilities for its size. This robot's development goes far

beyond to the Sandia Laboratories when DARPA asked for a hopping robot in 1997; they first developed a combustion powered dome shaped hopping robot [14]. Hopping system of the robot is based on expansion of the combustion gases and additional details can be traced in in US 6,247,546 [15]

Over the years the project passed down to Boston Dynamics and they turned the robot into a 4 wheeled jumper with launch legs [16]. Although robot is a bit larger than its competitors, with its superb performance Sand Flea is the current state of art of the subject. Despite the disclosed information demonstrating the abilities of the robot, the robot is not for sale yet. In fact, there is not even any reported field trial of the robot.

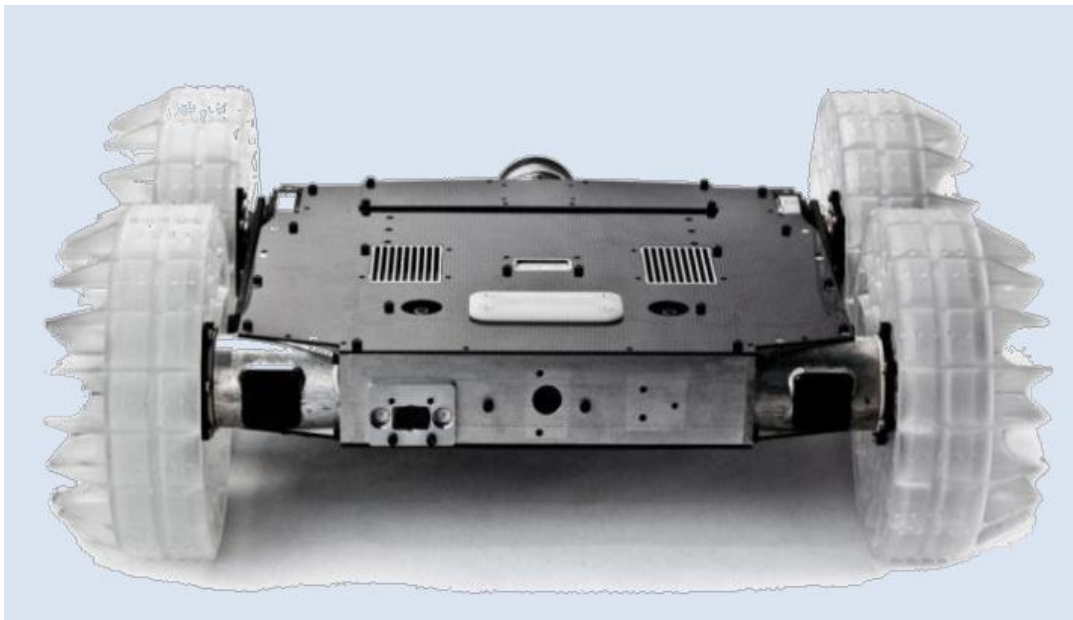


Figure 1-6: Image of Boston Dynamics Sand Flea



Figure 1-7: Sand Flea Positioning Itself Before A Jump

1.2.1.5. Comparison of the Commercialized Robots

Enlisted features of the commercialized robots are given in Table 1-1.

Table 1-1: Small reconnaissance robots which are already commercialized

Feature	FirstLook 110 [17]	Scout XT [18]	Armadillo [19]	Sand Flea [20]
Battery Life	6 hours	1 hour	1.5 to 2 hours	2 hours / 25 hops
Speed	3.4 mph (5.5 km/h)	1.0 mph (1.65 km/h)	3.11 mph (5 km/h)	3.4 mph (5.5 km/h)
Sound Level	N/A	22 dB @ 20m	N/A	N/A
Range	Up to 200m (LoS)	Up to 91m (LoS)	Up to 300m (LoS)	N/A
Max Obst. Height	7" (175 mm)	~ 50mm	-	Up to 8m
Weight	5.4 lbs (2.4 kg)	1.2 lbs (0.54 kg)	5.5 lbs (2.5 kg)	11 lbs (5.0 kg)
Length	10" (250 mm)	8.2" (209 mm)	11" (280 mm)	13" (330 mm)
Width	9" (221 mm)	7.6" (193 mm)	10.4" (260 mm)	18" (457 mm)
Height	4" (100 mm)	4.5" (114 mm)	5.1" (130 mm)	6" (152 mm)
Cost (Approx.)	15000 \$	4500 to 13000 \$	13000 \$	N/A
Drop Survival	16 feet (4.88m)	30 feet (9m)	8.2 feet (2.5m)	26.2 feet (8m)
Extras	4 camera, one has Pan, Tilt, 8x Zoom	Microphone inc., only 60deg FoV, black & white camera	5 camera, one has 4x Zoom, can carry 3kg payload, microphone inc. Can climb stairs with extra kit	Need to position itself before jumping

1.2.2. Robots Which Are On Their Development Phases

1.2.2.1. Mini-Whegs

Mini-Whegs is actually a series of small robots developed by the Case Western Reserve University over a few years and their evolution can be seen in Figure 1-8. It uses wheels for locomotion which enables the robot overcome relatively small obstacles easily [21]. The robots have around 200g mass and have 100mm length and 75mm width. It uses a four bar mechanism and a spring to store energy and release it by the means of a slip gear (Figure 1-9). As a result, it can achieve quite well jumps relative its size, yet the jumps are uncontrolled.



Figure 1-8: Family of Mini-Whegs



Figure 1-9: MiniWhegs Robot during its Jump

1.2.2.2. Jollbot

Jollbot is a spherical shaped, steerable robot which uses rolling as its primary locomotion. [22] Robot also has the capability to jump around %60 of its own height. Jumping idea

behind the Jollbot can be seen in Figure 1-10, a motor compresses the rods forming outer sphere and the rods store potential energy which is later released. Its slow speed and inability to carry any significant payload are main disadvantages of the robot.

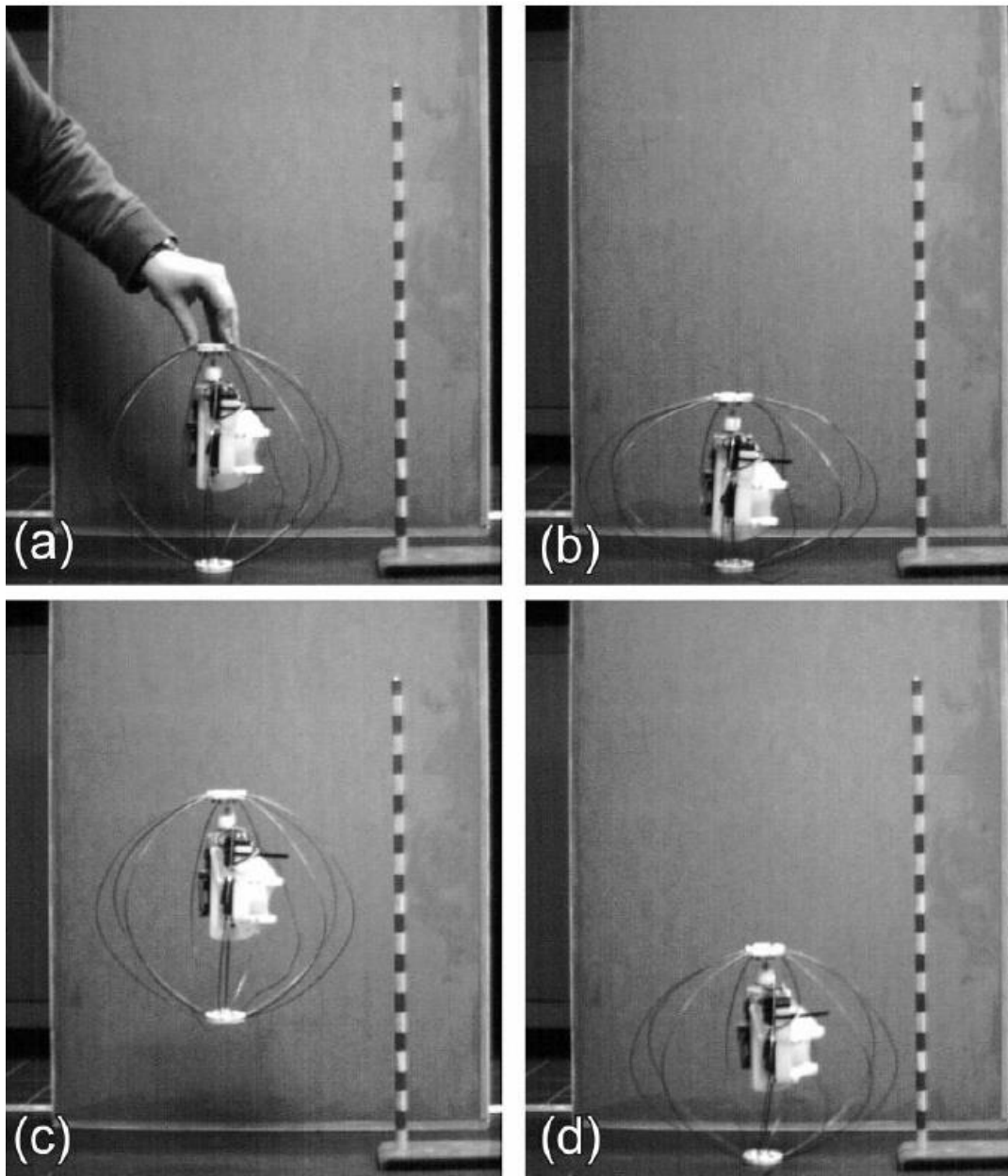


Figure 1-10: High speed camera images illustrating the jumping performance of Jollbot; (a) Resting state of Jollbot (b) 1.44 s later, Jollbot is ready to jump (c) 0.24 s later, (d) 0.22 s later Jollbot hits the ground and absorbs impact energy in the slight compressing of the sphere.

1.2.2.3. Shape Memory Alloy Based Robots

Using shape memory alloys to store potential energy, two very different kinds of small robots have been developed. One of them employs a catapult mechanism which is inspired by the jumping mechanism of flea as it can be seen in Figure 1-11 and Figure 1-12 [23]. The

robot has reported incredible jump to weight ratio but it lacks self-righting, locomotion and sensory devices.

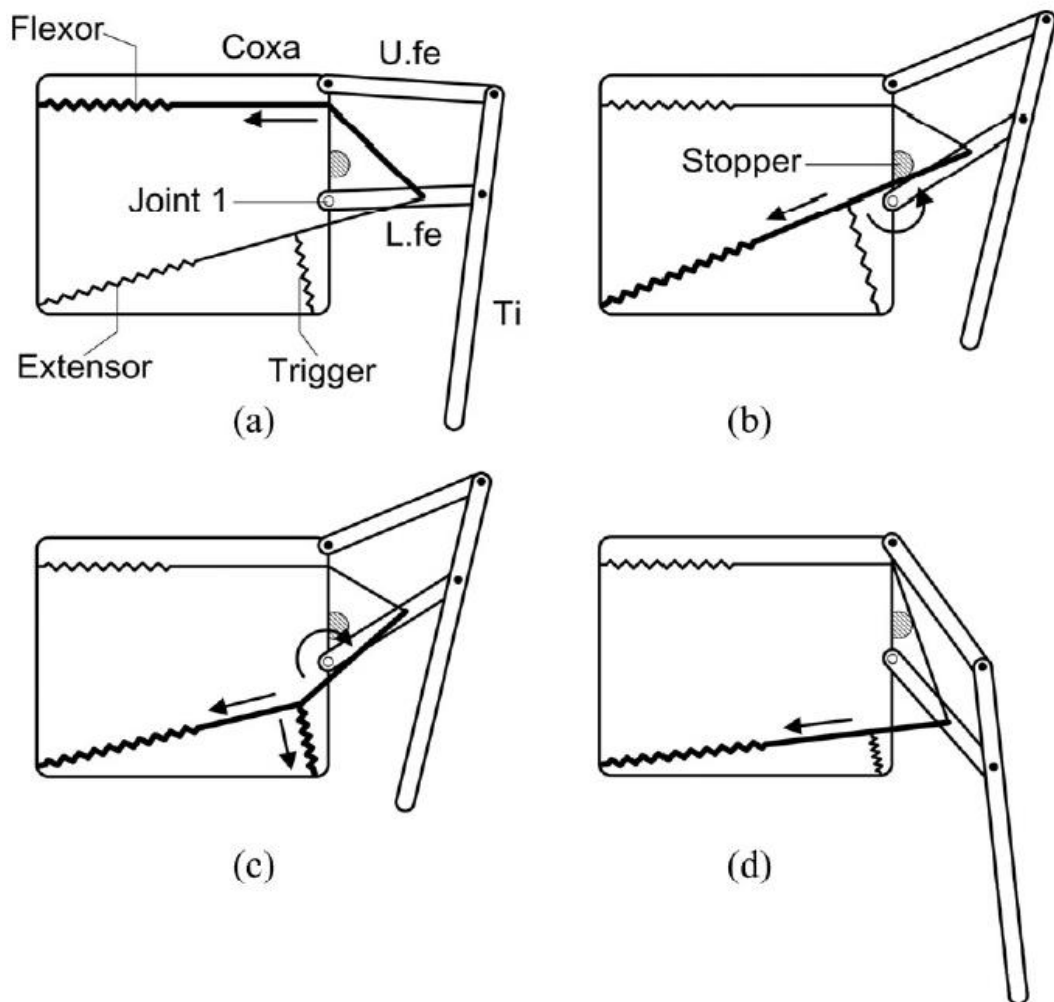


Figure 1-11:Flea Like Jumping Mechanism – a)Flexor muscle is contracted. b)Extensor is pulled beyond Joint1 and lower femur is stopped by stopper. c)Trigger muscle is pulled, changing the torque direction of the extensor muscle d)All Energy is released and jumping occurred.

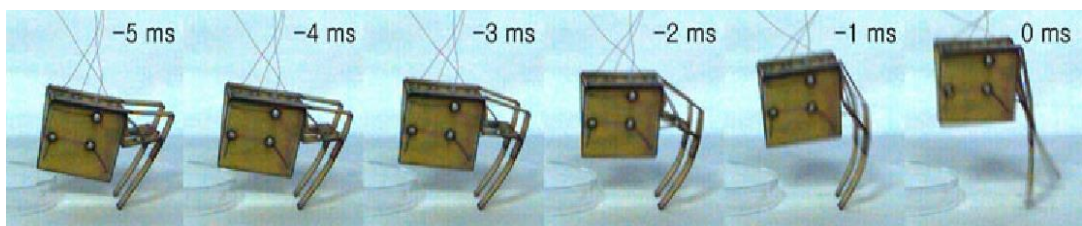


Figure 1-12: Flea-Like Robot Preparing For a Jump

Another use of shape memory alloys is to form a hoop or sphere with them to take the advantage of metastable structures. Using soft elastic shells with shape memory alloys, and

combining many of them to form a hoop or sphere robot; one can simply get a polymorphic robot. Using this structure, bistable structures can be formed to store potential energy and a small trigger will release all the energy.

Both of the SMA based robots suffer from slow thermal time constants of heating and cooling the SMA's. Also to be able to heat SMA's in acceptable amount of time, relatively high voltage levels are required. Of course, efficiency of the process is terrible as well, and SMA based locomotion and jumping has a long way to be used in actual systems.

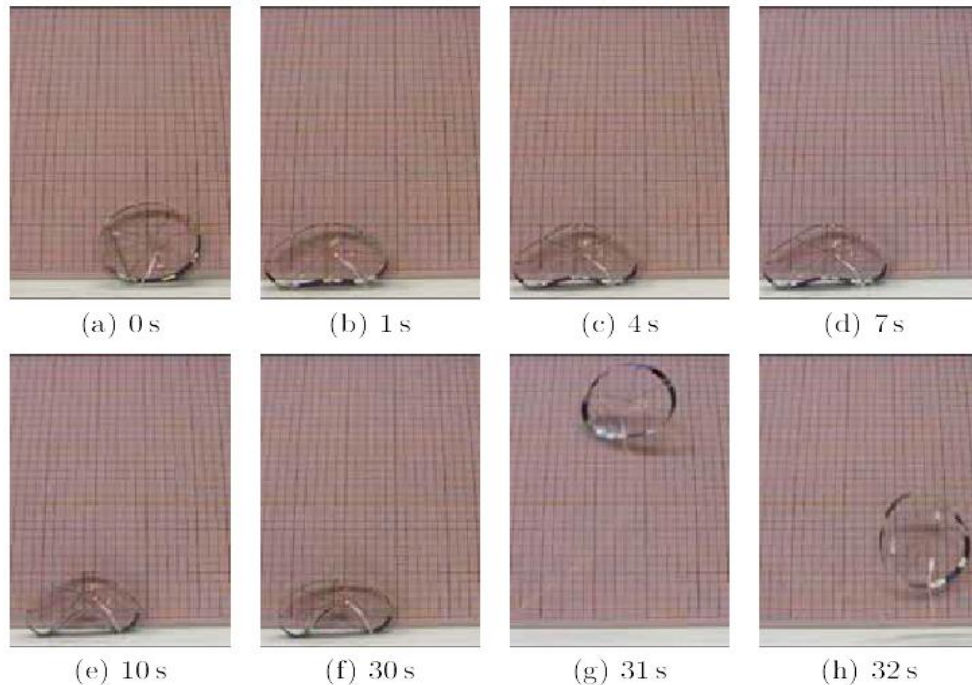


Figure 1-13: SMA Hoop Structure for Jumping

1.2.2.4. MSU Jumper

Jumping robot developed in the Michigan State University uses only a single motor to jump, self-right, travel and steer. Its interesting mechanical design includes a cleverly thought gear train and a capstan to achieve all of its functions. [24] Robot has very low weight for its size and using only a single motor makes its cost lower; yet it can't adjust its jumping power. The robot and its dimensions are not yet optimized; and its development is planned about making the robot a mobile sensor node.

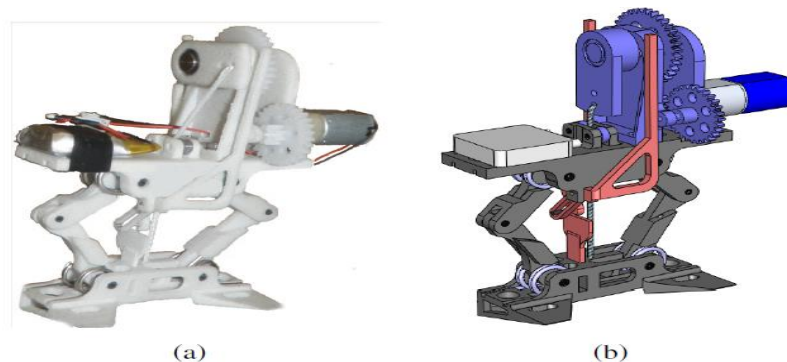


Figure 1-14: MSU Jumper a) Prototype b)Solid Model

1.2.2.5. Mowgli

Mowgli is a bio-inspired frog-like bipedal robot which can jump up to 40cm height. [25] Robot is pneumatically driven using McKibben air muscles. As it can be seen in Figure 1-15, each leg consists of 3 joints and 3 artificial muscles and 3 springs to store energy. Contracting and extending the air muscles using pneumatic valves, the robot can make rapid movements, yet can achieve quite soft landings due to the compliance of the legs and unactuated toe joint.

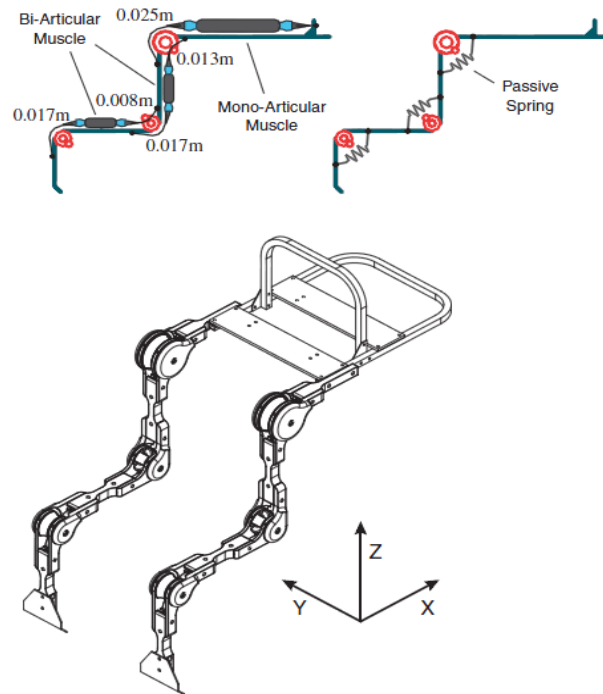


Figure 1-15: Bi-Articulated Jumping Mechanism of the Mowgli

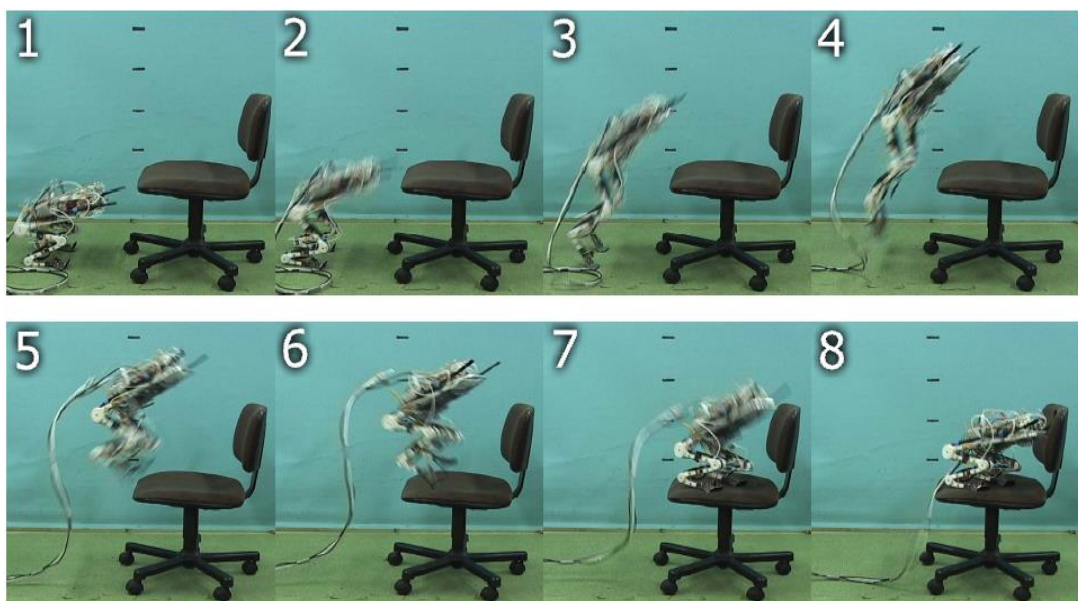


Figure 1-16: Mowgli Performing a Jump on a Chair

1.2.2.6. Grillo

Grillo is a small 50mm robot which uses a cam and springs to store potential energy [26]. Using the cam provides an easy way for the escapement mechanism; it also blocks the possibility of adjusting the jump itself.

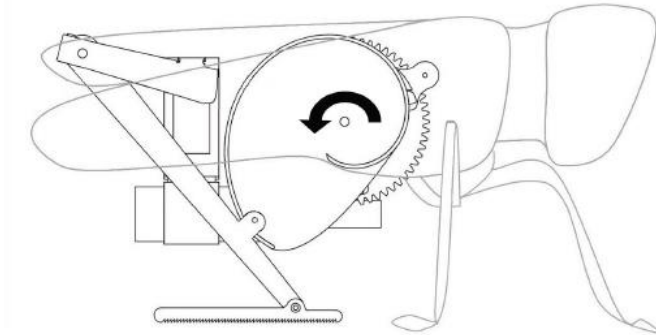


Figure 1-17: Schematic of the Jumping Mechanism of the Grillo

1.2.2.7. MIT Microbot

MIT Microbot is actually a robot in development for extraterrestrial mission yet it can be used for search and rescue operations as well [27]. This robot is not multimodal and its only type of locomotion is hopping. Hopping is achieved by Dielectric Elastomer Actuators (DEA), which convert electrical energy into strain energy. Unfortunately DEA's operate only at high voltage level, for the current Microbot they are pumped with 8.8kV; and this requires quite large DC-DC converters since battery voltage levels are much smaller. (The robot's high voltage needs are currently fed with external cables.) The robot's direction of jump is determined by 4 small DEA's and the main jumping power comes from ratchet mechanism which is charged by DEA.

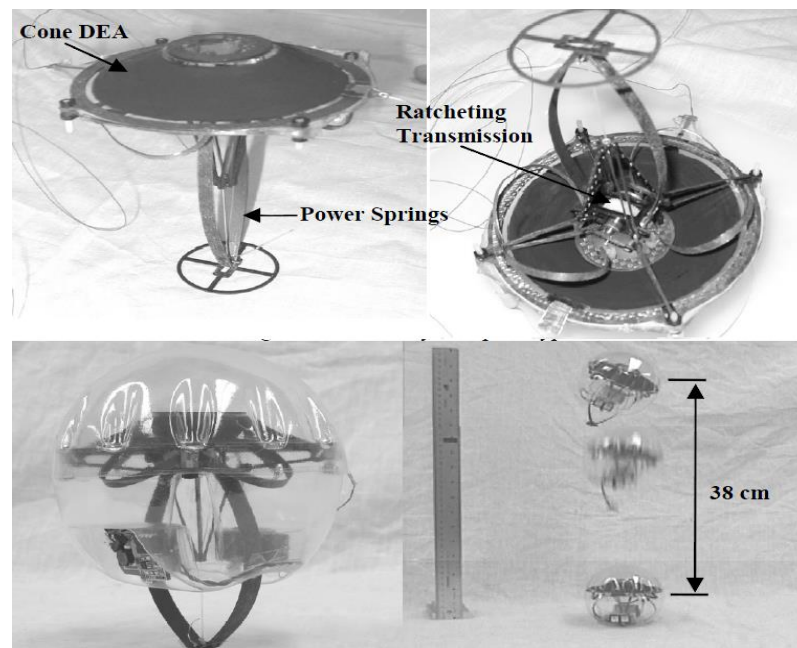


Figure 1-18: MIT Microbot with Dielectric Polymer Performing a Jump

1.3. Design Specifications

Concept of operation of such a robot should be quite simple; the user sets-up the robot in a base or vehicle, checking the batteries and any other sources of energy. Then, the user puts the robot in a cargo pocket, goes to the mission, throws the robot into action, and guides it using an operator controller unit (OCU).

Robot to be developed for this concept should be able to overcome obstacles both indoor and outdoor. Obviously, the stairs, one of the most common obstacles of the robotic world, comes to the mind. The stairs and other low profile obstacles in this scale of robots could be dealt with flippers or other useful mechanisms, but a more useful robot would be able to jump on a desk, or over a fence.

It never surprised anyone to see words “Throwing” and “Jumping” in the same sentence with “Impact”, and to cope with the impact energies mechanics must be resilient. Being rugged and being lightweight usually don’t mix together quite well, thus landing of the robot should be as soft as possible. Also, the robot has to continue operation when it lands, so either the robot must be operable in all possible landing configurations or some kind of self-righting mechanism has to be included.

Battery / resource life of such a robot is an important parameter as well; since robot is supposed to be featherweight, any unnecessary weight should be thrown out. Feedbacks coming from the testers makes it clear that 2 hours is much more than sufficient mission time for such a robot [28]. Also, they have figured out that 40 meters wireless communication range (non Line of Sight) is adequate for most of the missions.

Another design requirement is the strong desire of the users to control the camera view. Field reports demonstrate the fact that many users have desire to tilt the camera view for better view of the situation and the surrounding.

To sum up, the robot designed should,

- Survive at least 3m fall
- Jump at least 15 cm
- Weigh less than 5kg
- Has battery life of at least 2 hour
- Can tilt the camera position to get better view when desired

1.4. Overview of the Thesis

Scope of this thesis can be summarized by;

- Chapter 1 introduces the reader to the context, summarizes the current state of art in the field and provides main design requirements.
- Locomotion and suspension systems are highlighted in Chapter 2 as they are one of the key of concepts of such a vehicle. Suspension is built inside the wheel which has a similar operating principle of a cone clutch.
- Chapter 3 researches the possibility of hopping the robot through expanding carbon dioxide gas in a cylinder. Carbon dioxide gas is supplied by a cartridge similar to the paintball guns. Also, a striking mechanism is designed to be able pierce the cartridge to release the gas. Moreover, a tilting mechanism is designed for rotating the robot body with respect to ground to adjust the jumping ability and tilting the camera view.
- Electronic components and software of the robot are presented in Chapter 4.

- Last but not least, conclusion, recommendations and lessons learned from the thesis are summarized in Chapter 5. Also, future works are discussed as well.

Required components and the relationship between them are presented in Figure 1-19 which is the block diagram of the system.

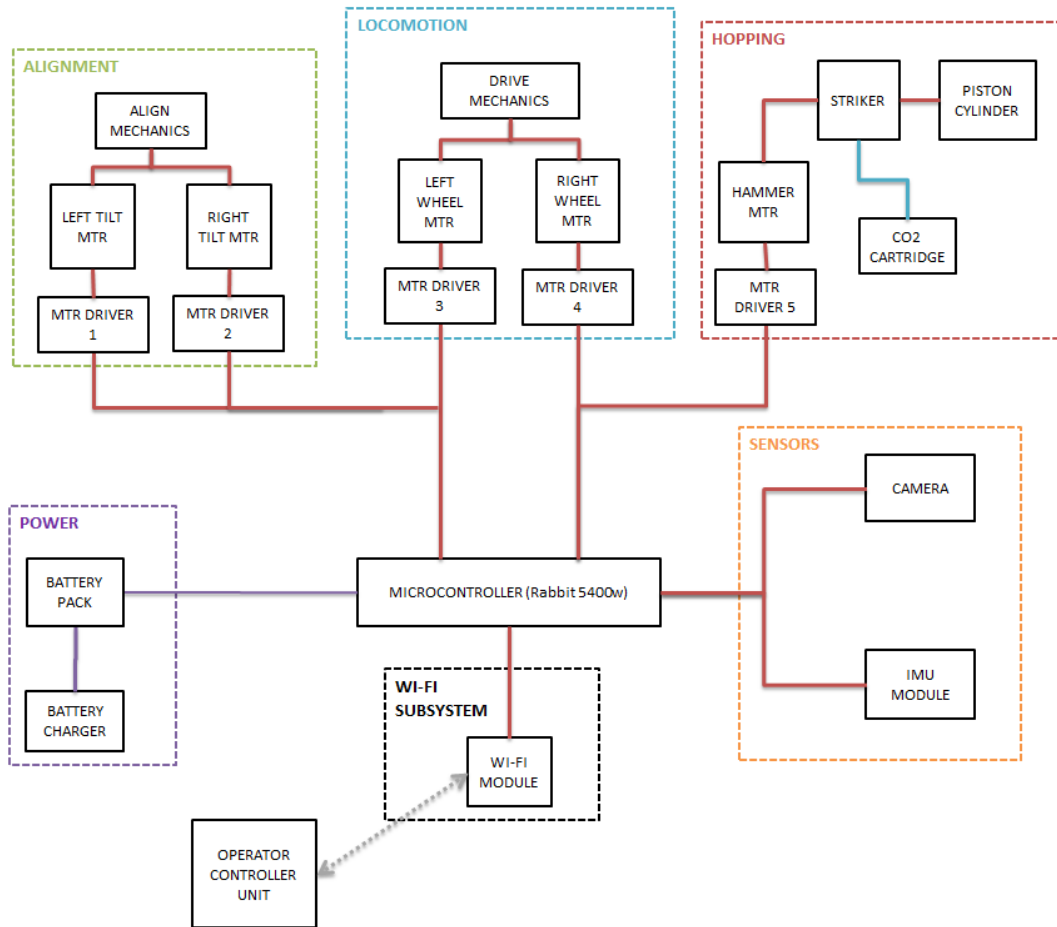


Figure 1-19: Block Diagram of the Robot

CHAPTER 2

LOCOMOTION SYSTEM

2.1. Introduction

In this chapter, the scope is to design an inexpensive and lightweight locomotion system for the robot which includes suspension inside the wheel. Many of the state of art locomotion system designs have been studied in the previous chapter and their design philosophy can be grouped as follows;

- Use plastic wheels which are resilient up to some degree, but other than that do nothing special; make the inner components as rugged as possible. (i.e. Scout XT, Armadillo)
- Use curved arches inside the wheel to achieve lower stiffness suspension (mostly used by iRobot such as Figure 2-1) or use the arches with hinges as shown in Figure 2-2. Sometimes wheels are segmented into parts aswell, mainly as these curved arches are good for compression, yet if the outer wheel is one piece, opposite side of the impact is loaded for tension, and will be the limiting factor for the deflection.
- Use viscoelastic polymers on a hub to achieve impact mitigation. Used as foam or molded into certain structural shapes such as honeycomb (i.e. Boston Dynamics Sand Flea Figure 2-3)

Among these design, the first option is obviously the simplest choice yet it fails to achieve required resilience expected from the wheel. Second option would be very low cost and easy to manufacture solution, unfortunately curved arches only allow for small deflections on the order of a few milimeters. To mitigate the impact shock received by the inner components the wheel should deflect a considerable amount, and with curved arches impact would be still severe. In third option, using foam would mitigate the shocks quite effectively and the wheels would be very low cost in mass production; and thats why foam is the favourite of the packing industry. Yet for a robot they are rather unsuitable, as foam would make the robot unable to move in wet or muddy terrain. Honeycomb type polyurethane or other viscoelastic material is the current state of art and satisfying results were reported in studies [29] ; yet they are extremely expensive and time consuming process to develop and prototype wheels according to the needs.

A rather different in wheel suspension system were designed and named “Cone Wheel” and it closely resembles cone clutch, and related work is presented in this chapter. At first, design concept is explained, then detailed design calculations and parameters are given and the chapter is concluded with the results of the actually manufactured wheels.



Figure 2-1: Resilience in wheel is achieved through curved arches in this iRobot Negotiator

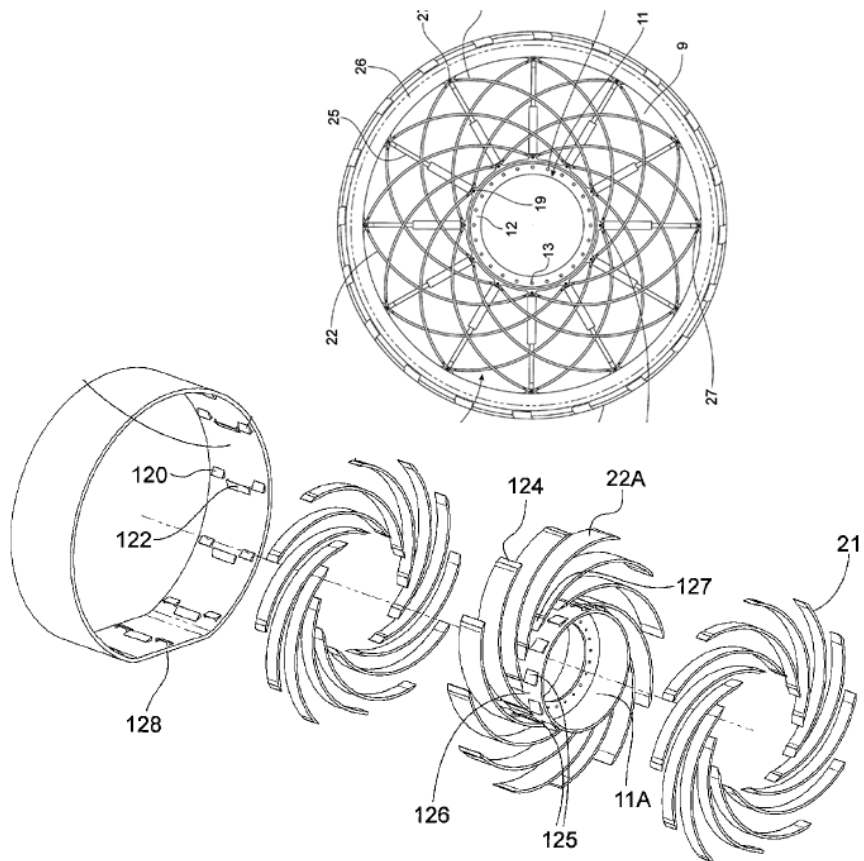


Figure 2-2: Resilient Wheel with Curved Arches as Springs and Dampers inside the Wheel [30]

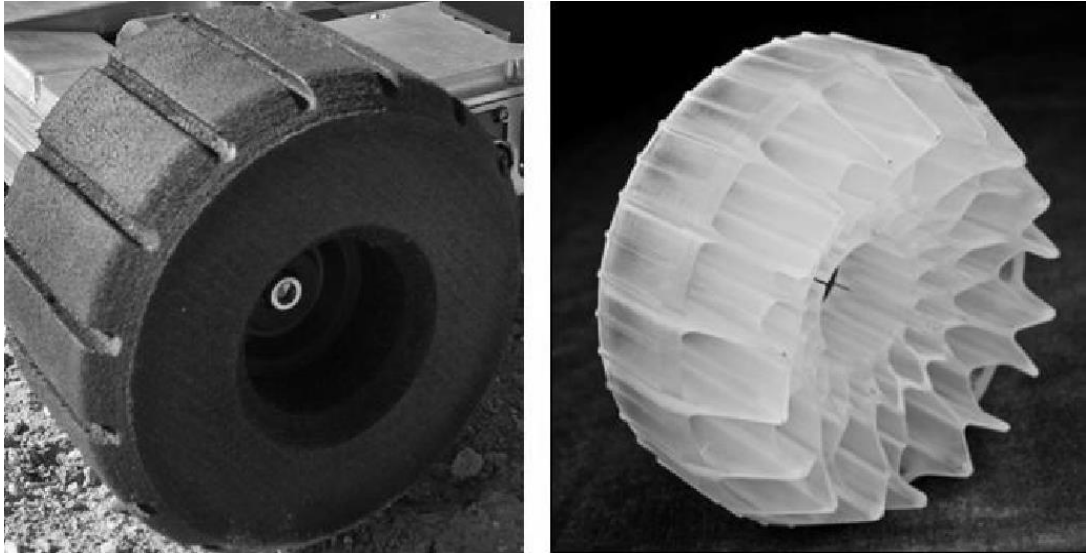


Figure 2-3: Two Wheel configurations developed for Boston Dynamics Sand Flea Wheels. On the left wheel is made out of soft foam and right shows the final wheel from polyurethane.

2.2. Cone Wheel Design Concept

Resilience required for the wheel could be achieved by using a wheel design similar to cone clutches.

The concept can be seen in Figure 2-4 the sketch on the left hand side helps to understand the actual components on the right hand side. The rim (green) has 2 female cone surfaces. Middle part of the rim is empty in an effort to reduce the weight. These cone surfaces mate with the two identical clutch male cones (yellow) which are pretensioned by the means of wave springs. Each male cone is fixed to a linear bushing (purple) and linear bushings are free to move linearly on the wheel shaft (grey) yet they rotate with shaft as they are screwed to the torque transmitter piece, any keyed to the shaft there through. Bottom of the key does not touch the shaft, therefore does not create any friction since it is held in place securely with screws. Instead of a key and linear bushings, a ball spline shaft and bushing could have been used, which would both simplify design and improve performance; however due to their high cost, spline shaft option was discarded.

Part (b) of the figure shows that when the wheel is impacted from the radial direction, inner cone surfaces slide on the outer cone surfaces, and springs are compressed. Friction associated with the sliding provides the friction to damp out the shock load. Initial tension, which is adjusted by the position of the nut, lets the cone surfaces return to their initial positions.

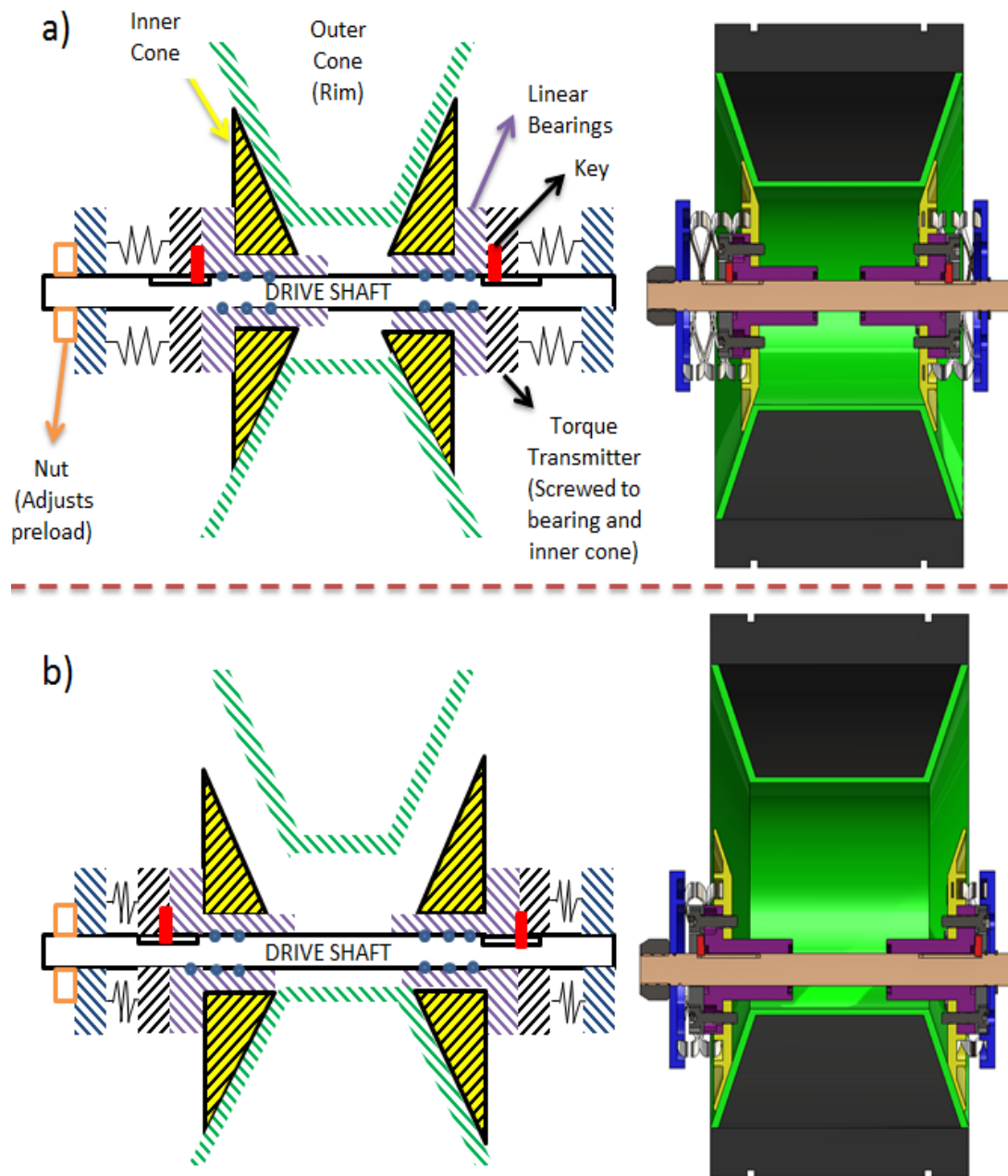


Figure 2-4: Cone Wheel Concept, left sides shows sketches and right shows the 3D model; on top a) natural state of the wheel can be seen, whereas part b) depicts deflected state is on the right



Figure 2-5: Spline Shaft Alternative, which would outperform key and linear bushing
[Courtesy of Thomson Linear]

2.3. Detailed Design of the Cone Wheel System

Assuming the inner cone and spring has no mass, static force equilibrium must exist between the wedge surfaces. Free body diagrams of the wedge surfaces is as follows;

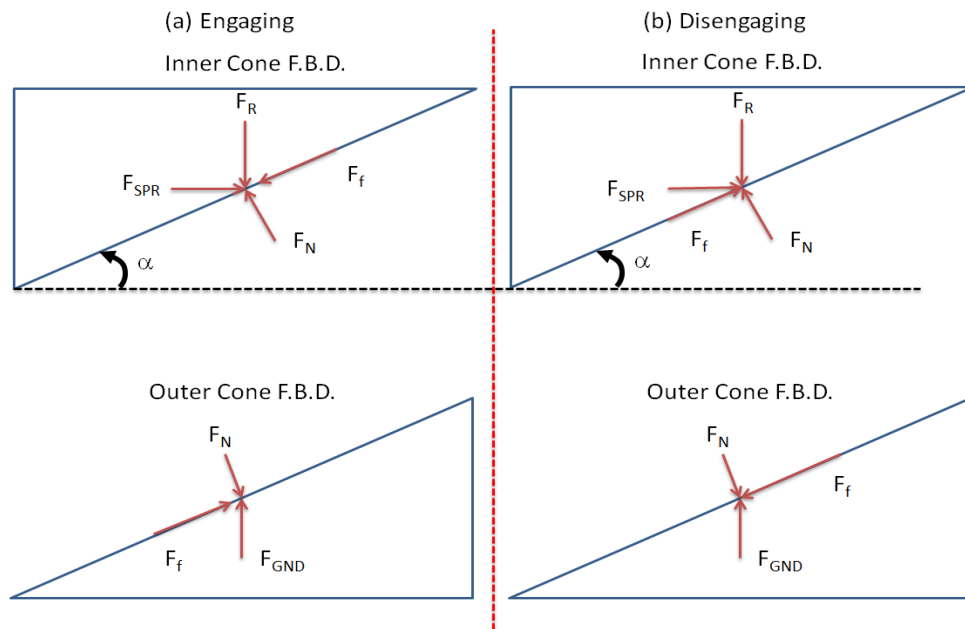


Figure 2-6: Free Body Diagram of the Cone Wheel

For disengaging the cones force equilibrium equations are,

$$\sum F_X = 0 = F_{Spr} - F_N \cdot \sin \alpha + F_f \cdot \cos \alpha \quad (1)$$

$$\sum F_Y = 0 = F_N \cdot \cos \alpha + F_f \cdot \sin \alpha - F_R \quad (2)$$

For engaging the cones force equilibrium equations are,

$$\sum F_X = 0 = F_{Spr} - F_N \cdot \sin \alpha - F_f \cdot \cos \alpha \quad (3)$$

$$\sum F_Y = 0 = F_N \cdot \cos \alpha - F_f \cdot \sin \alpha - F_R \quad (4)$$

Spring force is known with respect to position of the inner cone can be found in Eq. (5) where x_0 is the initial spring deflection.

$$F_{Spr} = k \cdot (x + x_0) \quad (5)$$

Friction force F_f is simply dependent on the normal force and friction coefficient as;

$$F_f = \mu F_N \quad (6)$$

Using (1), (2), (3), (4), (5), (6) the normal and radial force can be calculated as;

$$F_N = \frac{k \cdot (x + x_0)}{\sin \alpha - \mu \cdot \text{sgn}(\dot{x}) \cdot \cos \alpha} \quad (7)$$

$$F_R = F_N (\cos \alpha + \mu \cdot \text{sgn}(\dot{x}) \cdot \sin \alpha) \quad (8)$$

Applying Newton's second law for the vehicle and using (8) yields the following differential equation where $y/x = \tan(\alpha)$;

$$m \cdot \ddot{y} + 4 \cdot 2 \cdot k \frac{(\cos \alpha + \mu \cdot \text{sgn}(\dot{x}) \cdot \sin \alpha)}{(\sin \alpha - \mu \cdot \text{sgn}(\dot{x}) \cdot \cos \alpha)} (x + x_0) = 0 \quad (9)$$

The term x_0 has minor significance as it is quite small when compared to range of x . Solution to the differential equation has the form of;

$$y(t) = y_0 \cos(w_n t) + \frac{V_0}{w_n} \sin(w_n t) \quad (10)$$

And natural frequency of the system can be given as;

$$w_n = \sqrt{\frac{k_{eq}}{m}} \quad \text{where } k_{eq} = 8 \cdot k_{Spr} \cdot \frac{(\cos \alpha + \mu \cdot \sin \alpha)}{(\sin \alpha - \mu \cdot \cos \alpha)} (\tan \alpha) \quad (11)$$

Taking the derivative of the differential equation and equating to zero to find the maximum spring compression yields;

$$\dot{y}(t) = 0 = V_0 \cos(w_n t) \xrightarrow{\text{yields}} t = \frac{\pi}{2w_n} \quad (12)$$

$$y(t) = V_0 / w_n \quad (13)$$

Amount of the shock that will be reflected to the main chassis will be;

$$\ddot{y}\left(\frac{\pi}{2w_n}\right) = -w_n V_0 \quad (14)$$

Damped energy is the integral of friction force over the displacement and can be given by;

$$E_D = \int F_f ds = \frac{k \cdot \mu}{\sin \alpha - \mu \cdot \cos \alpha} \int_{x_0}^{x_f} \frac{x}{\cos \alpha} dx \quad (15)$$

Another thing to consider is the fact that the outer cone must be able to re-center itself in the rim. To achieve this initial spring force must be enough to lift the vehicle.

$$x_0 = \frac{m \cdot g \cdot \tan(\alpha)}{8 \cdot k_{eq}} \quad (16)$$

2.4. Parameter Selection for the Wheel

The system is designed to mitigate the shocks of falling from 3m heights. Due to design size limitations maximum displacement in the radial direction can be 20mm. Then from (13) it follows that natural frequency of the system should be around;

$$w_n = \frac{\sqrt{2 \cdot 9.81 \left(\frac{m}{s^2}\right) \cdot 3m}}{20mm} = 383 \frac{rad}{s}$$

Also, using (14) maximum shock system will experience is expected to be;

$$\dot{y}_{Max} \cong 300g$$

Since, natural frequency of the system is known, using (11) design chart for spring selection is presented in Figure 2-7. Design point of cone angle is selected as 70°.

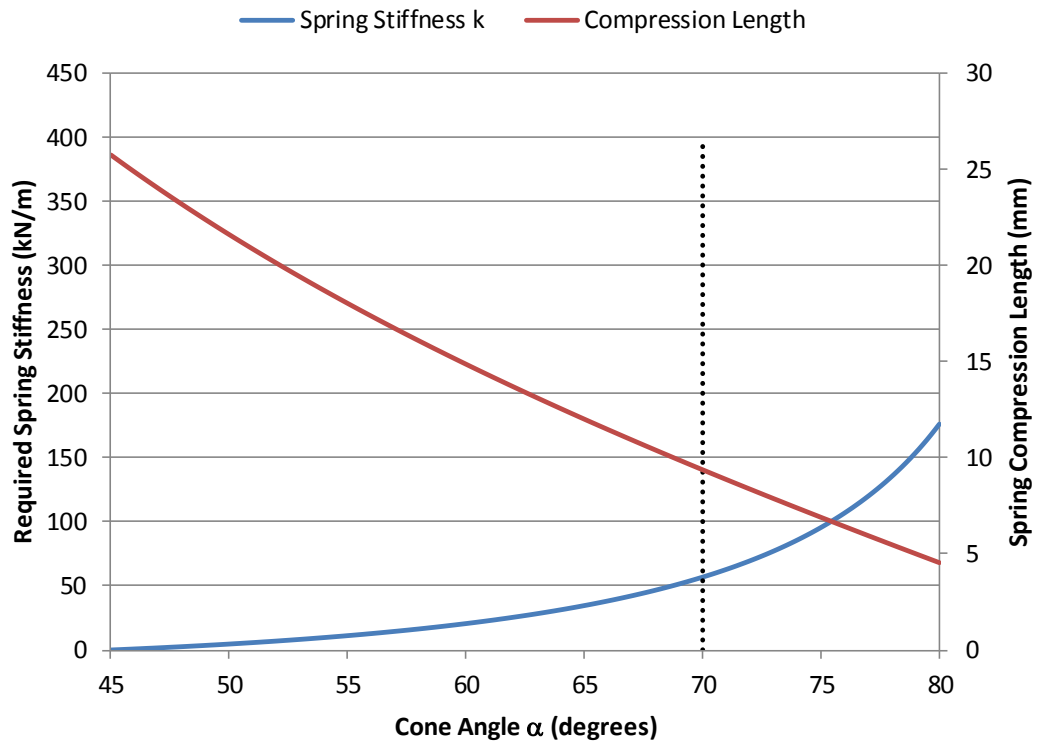


Figure 2-7: Cone Design Angle vs. Required Spring Strength and Spring Compression Length

2.5. Skid Steering And Timing Belt Transmission

To be able to make the robot take sharp, point turns; skid steering was selected as the steering method. As the robot does not have tracks outside of the wheels, an inner belt-pulley system was constructed. Also, wheel motors are not connected to wheel shafts to avoid the shock these shafts will get after the impact with the ground. Timing belt transmission also acts like a spring, protecting the fragile motor shaft and bearings from severe shocks. As the work pieces were already quite small, miniature ball bearings are used as idler pulleys. To get the motor a good angle of wrap, double sided belt had to be used. The constructed system is best represented in Figure 2-8. For wheel bearings, readily made bearing blocks were purchased and integrated into the system.

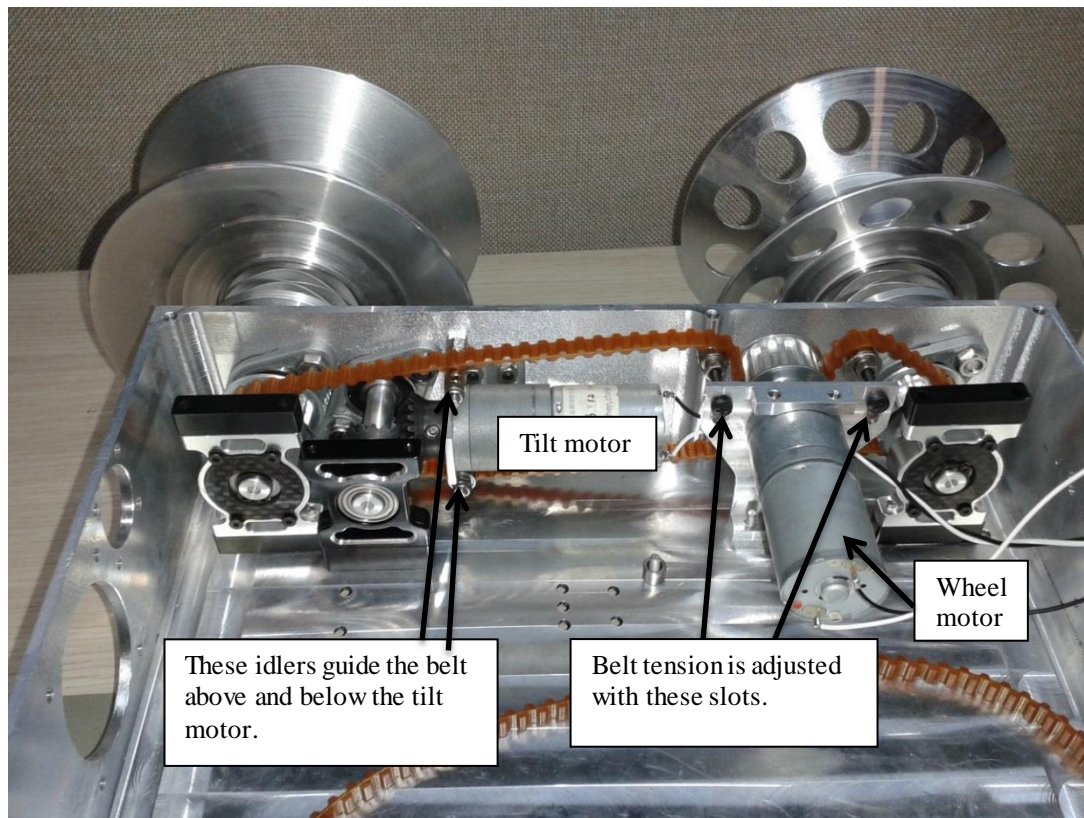


Figure 2-8: Locomotion System of the Robot, Showing the wheels, bearings, belt and pulleys. Wheel taken from the “dumbbell” is left wheel in the picture.

2.6. Results of the Manufactured Locomotion System

Material selection of the wheel was Aluminium 7075-T651, and mainly due to its superior strength when compared to its density. Shaft and other small pieces were also made from the same material.

Manufacturing the cone wheel was done incrementally. Firstly, the design was verified by making a dumbbell shaped shaft design with cone wheels at its end. Cone angles of the wheels were 70° and the dumbbell showed quite good results; when loaded, springs deflected in the close vicinity of their expected deflection.

When manufacturing the actual wheels, additional drilling operations were added to reduce weight, as one of the fallback of this design is its weight.

Figure 2-8 shows the left side of the robot's locomotion system, with timing belt, pulleys, motor and bearings. Left wheel in the figure is the first manufactured 70° cone, and right wheel has a cone angle of 60°. Belt is tensioned using the idlers pulleys, where idlers are rather small bearings attached to the screw and hold in place with two counter nuts pressing their inner part. Two other idlers were also used to guide the belt above and below the tilt motor. Timing belt pulleys were attached to the wheel shafts using setscrews.

Robot was subject to 3m tests and shock levels were measured with an accelerometer. The test results vary between 350g – 850g for two reasons and a sample measurement is presented in Figure 2-9. Firstly, number of wheels came to contact with ground has a huge impact on the measurements, the more balanced the robot drops, the less shock the robot is subjected. Also, the location of the sensor effected the measurements, higher shock levels were measured toward the center. Almost in all cases shock duration was around 1ms.

Cone wheel is depicted in Figure 2-10 with its natural and deflected states. Also, wear due to friction could be seen in the Figure 2-11. With appropriate coatings such as hardened eloxal wear problem could be minimized. Also, since the shafts were not hardened or coated; balls of the linear bushings caused wear problems on the shaft as well.

Table 2-1 reveals the weight of the each component in the wheel assembly. At first glance, linear bearings get the attention with their high weight. They are off-the-shelf products, and made of steel, thus contributing to the approximately %20 of the wheel weight. If custom linear bearings were manufactured, weight due to linear bearings could easily be halved; unfortunately the design and manufacture of a bearing is a cumbersome task which is beyond the scope of this thesis. With appropriate bearing and shaft design, torque transmitter piece would also be eliminated.

Table 2-1: Weight Contribution of the Cone Wheel

Wheel Assembly	Amount	Unit Weight (g)	Total Weight (g)
Wave Springs	2	12.30	24.6
Linear Bearings	2	40.00	80
Outer Cone	1	95.93	95.93
Inner Cone	2	24.47	48.94
Tire	1	80.00	80
Shaft	1	20.97	20.97
Spring Holder	2	12.24	24.48
Torque Transmitter	2	7.17	14.34
Wheel Total			389.26

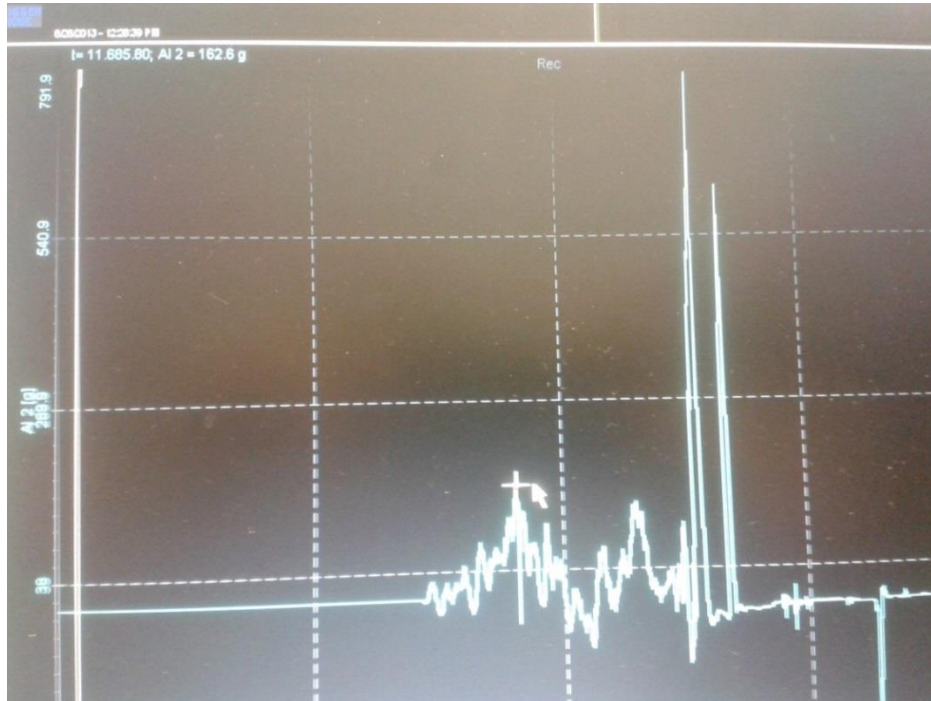


Figure 2-9: Shock response of the 3m Drop-down test on robot



Figure 2-10: Cone Wheel shown in natural state in top and deflected state on bottom



Figure 2-11: Marks of wear on the cone wheel

CHAPTER 3

HOPPING SYSTEM

3.1. Introduction

Aim of this chapter is to design an inexpensive hopping system for the robot. Hopping over obstacles would give reconnaissance and surveillance robots much more versatility as regular unmanned ground vehicles cannot overcome obstacles taller than their own height.

Many different actuated modes of jumping were studied which includes but not limited to sudden release of springs, shape memory alloys, di-electric polymer actuators, pneumatic air muscles, and utilization of combustion gases. Most of these technologies are still on their baby steps and up to date no mesoscale robot with hopping ability has been commercially sold.

Combustion of a hydrocarbon in a linear actuator and using the expansion of exhaust gases to provide the necessary thrust for piston is the current state of art for mesoscale robotics, and the system is still being developed by Boston Dynamics [31]. Concept of the combustion powered hopping ability is demonstrated in Figure 3-1, downside of this system is its high cost and complexity for a robot that is supposed to be inexpensive and expendable by the nature of its use.

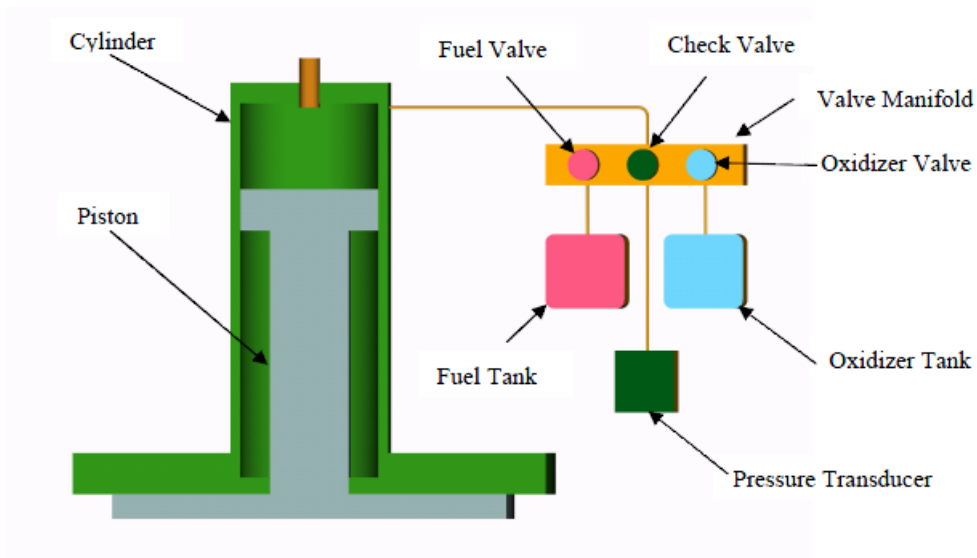


Figure 3-1: Boston Dynamics Sand Flea Hopping System Using Combustion

Charging mechanical springs or other spring like materials and mechanisms are also utilized in many different designs in the literature, and most of them are bio-inspired trigger

mechanisms. Mechanical energy storage mechanism are utilized for robots less than one kilogram as storing the energy by mechanical means increases the weight of robot, and it becomes unfeasible with the current technology for a non-miniature robot.

In an effort to make an affordable hopping system for the robot, this chapter, first focuses on jumping a robot with CO₂ gas which is abundant, cheap and less complex than combustion process. The chapter is continued with the design of a tilting mechanism to make the robot jump at any desired angle.

3.2. Preliminary Calculations for Jumping with a Piston Cylinder Arrangement

To start with, the robot considered throws a piston to ground and jumps with reaction from the ground, with schematic sketched as Figure 3-2.

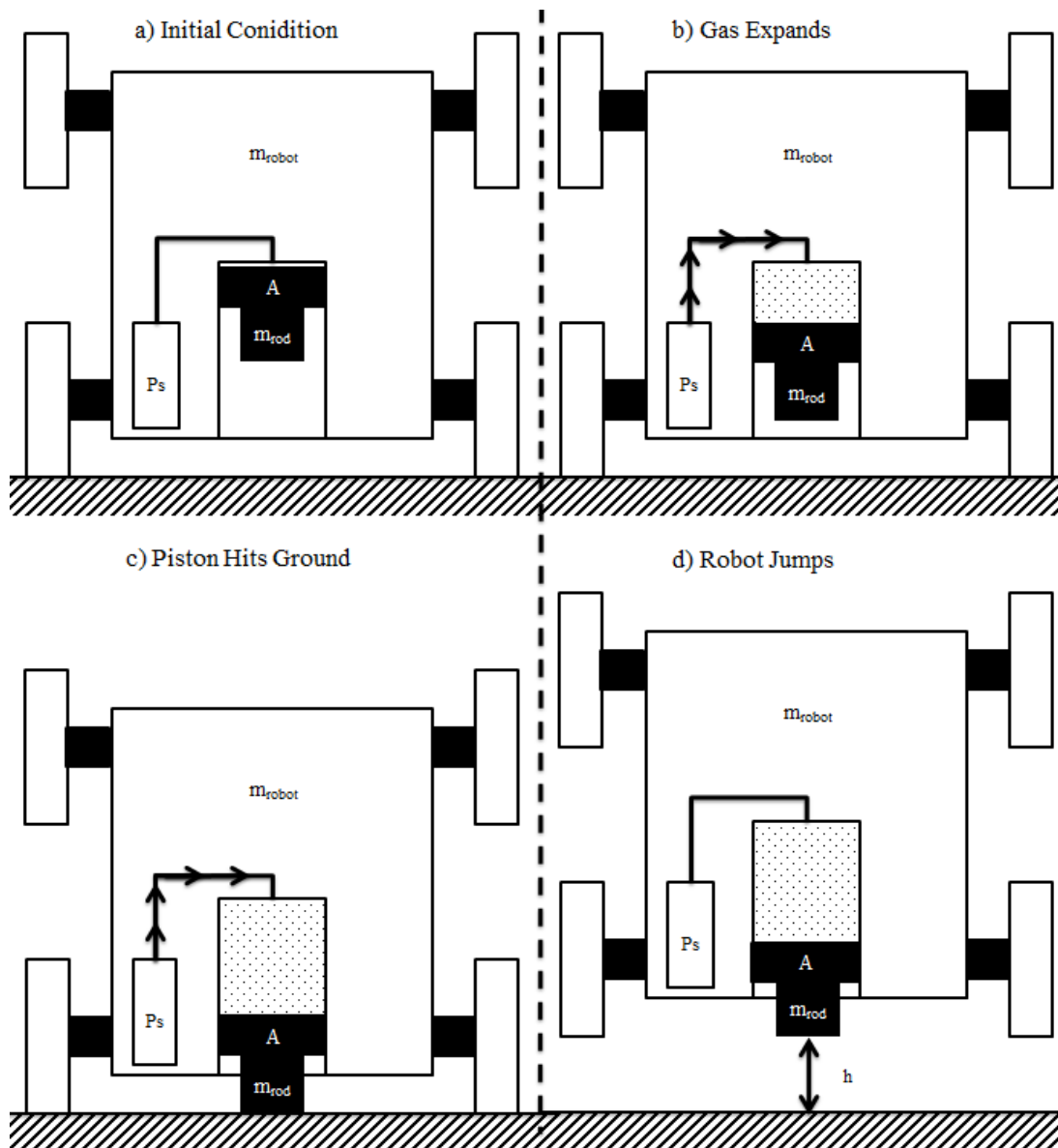


Figure 3-2: Sketches demonstrate the phases of hopping; a) At initial condition piston is at the end of cylinder, b) Gas pressure is applied and piston accelerates, c) Piston collides with ground and kinetic energy of piston passes to whole robot, d) Robot jumps with the kinetic energy

Ignoring compressibility effects, loss of pressure due to orifice, friction and assuming pressure in the cylinder is constant at P_s , using Newton's Second Law for the piston yields,

$$m_{piston} \cdot a_{piston} = A \cdot (P_s - P_o)$$

Exit velocity of the cylinder is given by where s is stroke length (assuming uniform acceleration),

$$V_{piston,Max}^2 = 2 \cdot a_{piston} \cdot s$$

Assuming the perfectly elastic collision with ground, momentum of the piston is equal to the momentum of the robot and initial velocity of the robot can be found as;

$$m_{robot} \cdot V_0 = V_{piston,Max} \cdot m_{piston}$$

$$V_0 = \sqrt{2 \cdot a_{piston} \cdot s} \cdot \frac{m_{piston}}{m_{robot}}$$

Ignoring air drag and other frictional terms slowing the robot, all of the initial kinetic energy is converted to potential energy at the highest point of jump, so jump height is calculated as

$$h = \frac{V_0^2}{2g}$$

Combining the jump height equation with the piston exit velocity yields;

$$h = \frac{m_{piston} \cdot A \cdot (P_s - P_o) \cdot s}{m_{robot}^2 \cdot g}$$

Using ideal gas law, consumption of the gas can be related with the same mechanical parameters;

$$m_{Gas} = \frac{PV}{RT} = \frac{P_s \cdot A \cdot s}{RT}$$

The preliminary equations demonstrate that during design process, piston area and stroke length should be maximized and a high enough supply pressure must be obtained to achieve jump.

3.2.1. Using CO2 Gas for Jumping

Compressed carbon dioxide is found to be the best alternative as a readily available compressed gas source due to its abundance and very low cost. In the market many different sizes of CO2 cartridges can be found starting from 8 gram cartridges to 88 gram large cylinders as some of them can be seen on Figure 3-3. They are commonly used in airguns to shoot pellets, cyclists use them as portable tire inflators, and aquarium hobbyists use it to control the level of pH of water; thus they are readily mass manufactured. Cartridges with or without threads at the neck part are available. At the top of neck a rather thinner cap has to be pierced when the cartridge is being used. Cap also serves as a safety precaution, if the cartridge is heated and the pressure inside increases, cap bursts around 150 bar.

12g cartridges are the most commonly utilized ones, and a single cartridge is priced around 60 cents. These cartridges are made out of recyclable steel, and have gross mass of 42g. Dimensions of 12g cartridges 83mmx15mm and they have inner volume of the 15cm³.



Figure 3-3: Typical CO₂ cartridges found on the market, many seen with black foams on them to avoid frostbite

CO₂ is colorless, odorless, non-toxic, non-flammable gas with almost no health hazards. Its phase diagram is given in Figure 3-4, and it can be seen that at room temperature, it has relatively high vapor pressure of around 60 bar, yet pressure drops rapidly at lower temperature. The critical point of CO₂ is 7.38 MPa at 31.1°C. Inside the cartridge, at room temperature liquid and gas states coexist and pressure of the gas is actually the vapor pressure of the CO₂. As the critical point is very close to room temperature, latent heat of evaporation is small. The vapor pressure can be approximated by the following equation and its graph is Figure 3-5:

$$\ln(P_{CO_2, vap}) = A \cdot \ln(T) + \frac{B}{T} + C + D \cdot T^2 \quad \text{where} \quad \begin{cases} A = -2.403761 \times 10^1 \\ B = -7.062404 \times 10^3 \\ C = 1.663861 \times 10^2 \\ D = 3.368548 \times 10^{-5} \end{cases}$$

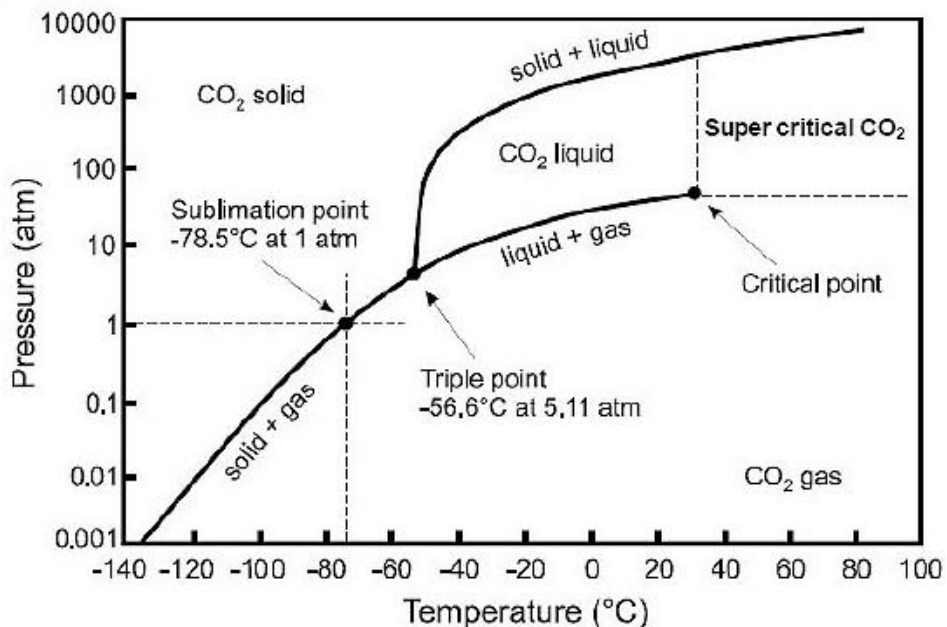


Figure 3-4: CO₂ Triple Point Graph [32]

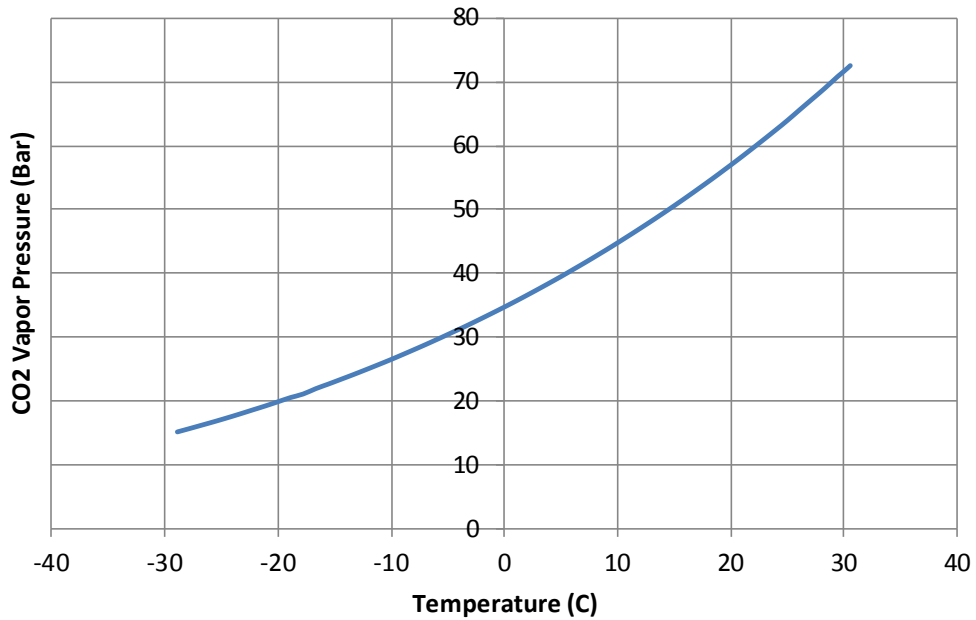


Figure 3-5: CO2 Vapor Pressure versus Temperature

3.2.2. Preliminary Calculations with CO2 as source

Before optimizing the design parameters, let us first see if CO2 is suitable for this job. This is achieved by guessing mechanical parameters considering the robot's size. First assumption to start with is taking ambient temperature as 20°C. Thus CO2 vapor pressure in the tank becomes; $P_{tank} = 5.73 \text{ MPa}$.

Let us assume a cylinder with 50cm^3 (i.e. diameter of 25mm and a stroke of 100mm gives a tube of 49 cm^3), and calculate the jumping height for various robot and rod mass parameters. The output of the carried out calculations is demonstrated in Figure 3-6.

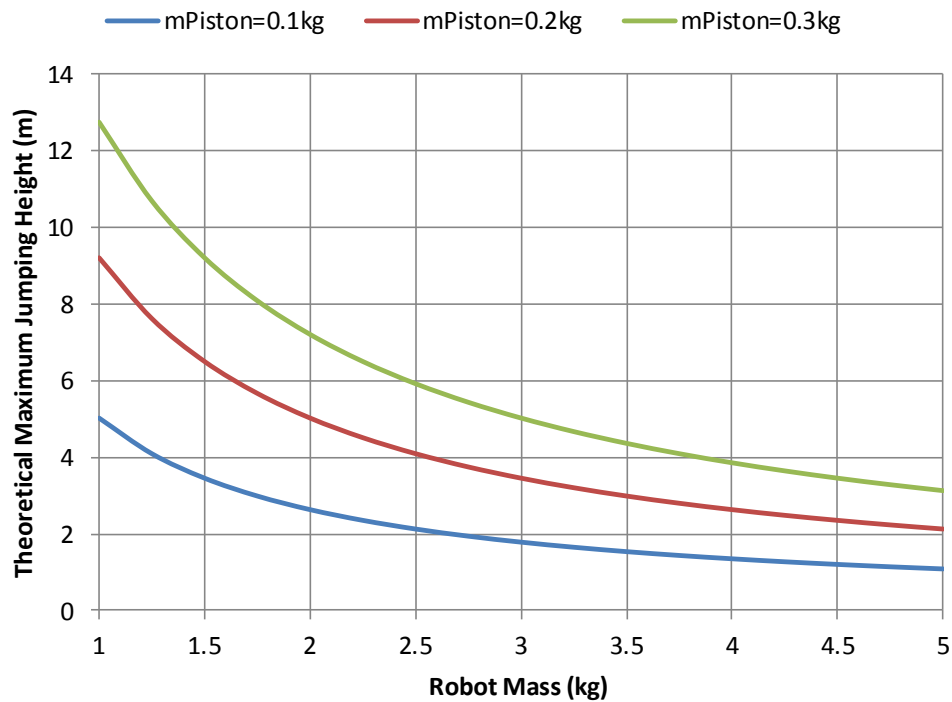


Figure 3-6: Theoretical Jumping Heights with CO2 with a Cylinder stroke of 50 cm^3

It can be seen that as the weight increases jumping height decreases rapidly, yet a 3kg robot can be hopped using CO2 cartridge as the power source. Note that with predicted volume, CO2 consumption is also 5 grams, which can be considered as feasible. After these preliminary calculations 12g CO2 cartridges are selected as the compressed gas source of the robot.

3.3. Detailed Model of the CO2 system

After seeing the object is attainable, let us go into further detailed calculations and develop a pneumatic model of the process to account for previously neglected factors. Major approximations of the previous model were;

- i. Constant pressure: Due to compressibility of the gas, actuator cannot exert full force especially at the start zone. In addition, the orifice area of the cartridge will limit the gas flow of CO2 and pressure in the cylinder will not be as high as the supply pressure. Thus effect of orifice area will be investigated.
- ii. Constant Temperature: Sudden expansion of the gas in the cylinder will lower its temperature; thus making the process to consume more CO2 than previous calculations. Also, heat transfer between the cylinder and the gas will be considered.
- iii. Friction: Friction will exist between cylinder and piston which in return slow down the piston's exit velocity and reducing robot jump.

Modeling of the system is carried out such that each component of the system is modeled independently and connected to other elements with causal relationships among them. Using Matlab Simulink, the differential equations governing the motion of the piston are solved. States of the elements of the system are shown in Figure 3-7, and the modeling process in Simulink is implemented according to it.

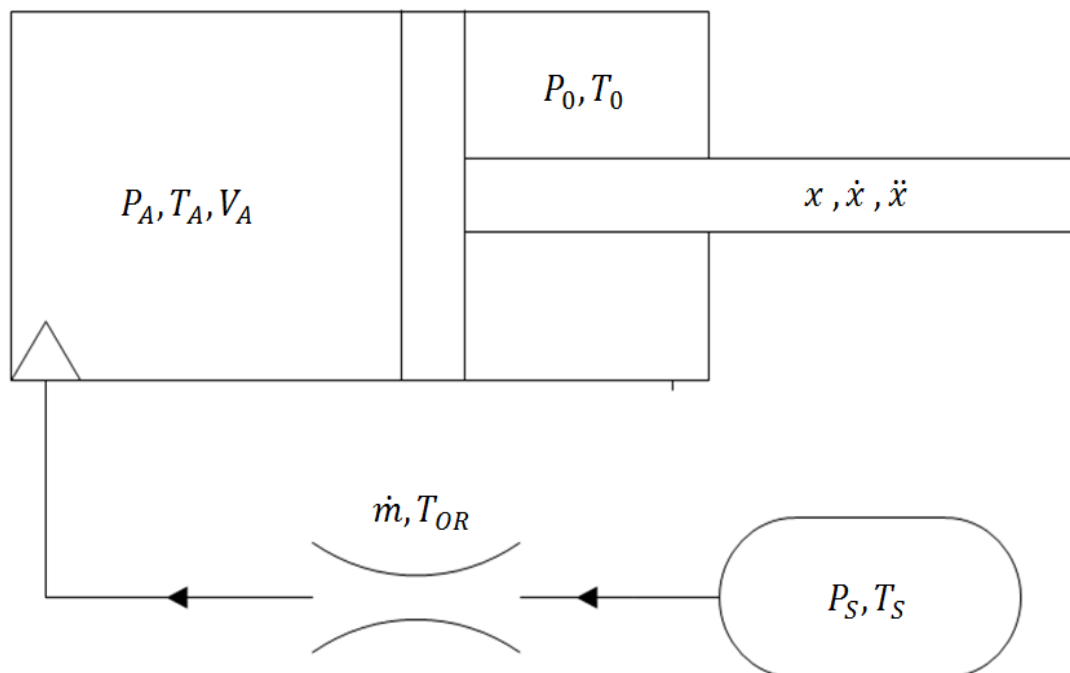


Figure 3-7: Schematic States of the Elements

3.3.1. CO2 Cartridge

Inside the cartridge, CO2 both liquid and gas states of the CO2 exists, and during the operation liquid would evaporate. CO2 has critical point at 304.25K at 7376kPa which is quite close to the working region we are assuming. Also, some of the gas to be consumed will be readily available as gas already, inside the cylinder. Using ideal gas law, it can be estimated that around 1.5g of CO2 is at gas state in room temperature

As the liquid phase start to evaporate, it would decrease its own temperature and thus vapor pressure. Yet, the heat transfer from the metal tube would lower the cooling rate. Thermodynamics of this process is rather complex and resides beyond the scope of this thesis. So, the cartridge is approximated as a supply tank with constant pressure and temperature.

3.3.2. Orifice

Orifice limits the gas flow rate from the cartridge to the actuator due to its passage area. For this analysis, orifice is the hole in the cartridge. To calculate the gas flow rate through the orifice, inputs are supply pressure, temperature of the cartridge, and backpressure on the actuator side.

Flow through the orifice is approximated using ISO standards [33] as;

$$Q = \begin{cases} 120.S.P_s \sqrt{\frac{293}{T_0}} \cdot \frac{10^{-3}}{60}, & \frac{P}{P_s} \leq 0.5 \text{ (choked flow)} \\ 240.S. \sqrt{P(P_s - P)} \sqrt{\frac{293}{T_0}} \cdot \frac{10^{-3}}{60}, & \frac{P}{P_s} > 0.5 \text{ (subsonic flow)} \end{cases}$$

So the mass flow rate of CO2 gas from the orifice can be calculated as follows where ρ is the density of the gas at the reference condition;

$$m = \dot{Q} \cdot \rho$$

Also, due to pressure drop, gas goes through an expansion which can be approximated to be adiabatic. Temperature of the gas exiting the orifice is given by;

$$T_{OR} = T_s \cdot \left(\frac{P_A}{P_s}\right)^{\frac{k-1}{k}}$$

Matlab model of the orifice is given in Figure 3-8 utilizing the equations given in this section.

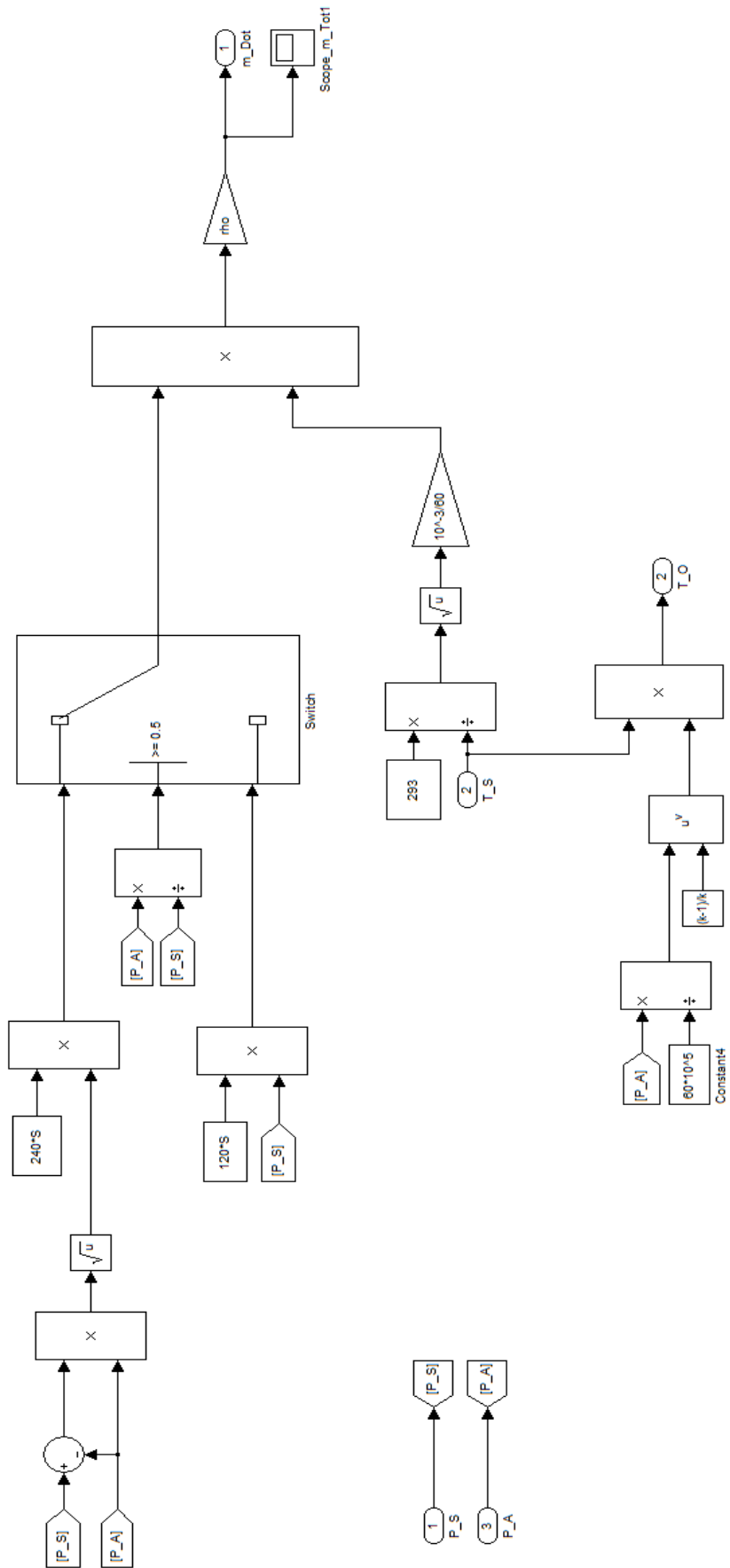


Figure 3-8: Matlab Model of the Orifice

3.3.3. Actuator

Actuator receives the gas from the orifice and the gas expands inside the cylinder, thus its inputs are the mass flow from the orifice and its temperature. Its outputs are the pressure in the chamber P_A , and the position of the piston x .

Firstly, continuity equation for the CO2 mass in the cylinder is simply;

$$m = \int \dot{m} \quad (17)$$

At any instant volume of the active chamber **A** in actuator is given by;

$$V_A = V_{0,A} + x \cdot A \quad (18)$$

Where $V_{0,act}$ is the dead volume of the actuator and the tubing between the orifice and the actuator, x is the position of the piston and A is the area of the pressurized side of the piston. Also, velocity and acceleration of the piston are \dot{x} and \ddot{x} , respectively.

Applying Newton's second law to the piston yields;

$$A(P_A - P_0) = m_p \cdot \ddot{x} + f + c\dot{x} \quad (19)$$

Also state equations for the velocity and position of the piston are simply;

$$\dot{x} = \int \ddot{x} \quad (20)$$

$$x = \int \dot{x} \quad (21)$$

In this equation, \dot{m} is the input and volume increase rate, \dot{V}_A , can be found by;

$$\dot{V}_A = \dot{x} \cdot A \quad (22)$$

Using first law of thermodynamics for the expansion of the gas in the cylinder;

$$dq = du + P_A \dot{V}_A \quad (23)$$

Energy flows into the actuator due to both mass flow rate from the orifice and the heat transfer from the cylinder body;

$$dq = C_V \dot{m} T_{OR} + \alpha(T_0 - T_A) \quad (24)$$

Where internal energy of the gas is given by $U = C_V m T_A$ and its derivative with respect to time with the assumption of constant specific heat;

$$dU = C_V \dot{m} T_A + C_V m \dot{T}_A \quad (25)$$

Combining equations (23), (24) and (25) yields;

$$\dot{T}_A = - \frac{P_A A \dot{x} + C_V \dot{m} (T_A - T_{OR}) - \alpha(T_0 - T_A)}{C_V m} \quad (26)$$

Also, state equation for T_A is simply;

$$T_A = \int \dot{T}_A \quad (27)$$

To find the pressure build-up, taking the first derivative of the Ideal gas law ($P_A V_A = m \cdot R \cdot T_A$) in the chamber yields;

$$\dot{P}_A = \frac{\dot{m} \cdot R \cdot T_A + m \cdot R \cdot \dot{T}_A - P_A \cdot \dot{V}_A}{V_A} \quad (28)$$

And the pressure state is simply;

$$P_A = \int \dot{P}_A \quad (29)$$

Unknown parameters are 10 unknowns ($x, \dot{x}, \ddot{x}, V_A, \dot{V}_A, m, T_A, \dot{T}_A, P_A, \dot{P}_A$) and there are 10 equations excluding (24) and (25).

Matlab model of the actuator is given in Figure 3-12, with its subsystem providing differential equations are given in Figure 3-11, Figure 3-9 and Figure 3-10. Also, it can be seen in Figure 3-11, variable specific heat approach is supported to make even more detailed analysis. Also note that, piston is not sealed and there will be some leakage around the piston, and it is not present in this model mainly due to the lack information about the leakage coefficient. Sealing the piston would increase the friction much more than the benefit it brings by eliminating the leakage.

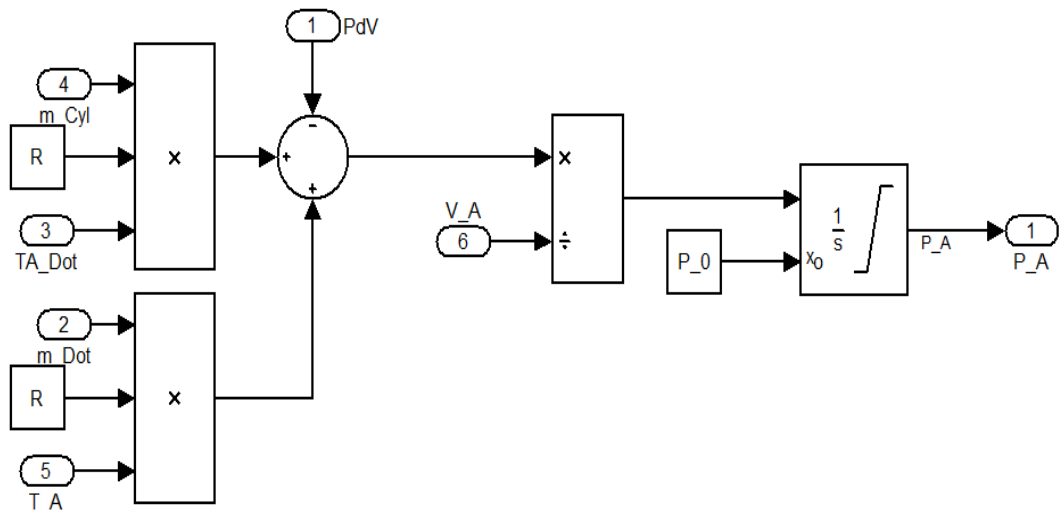


Figure 3-9: Ideal Gas Law Subsystem of the Actuator

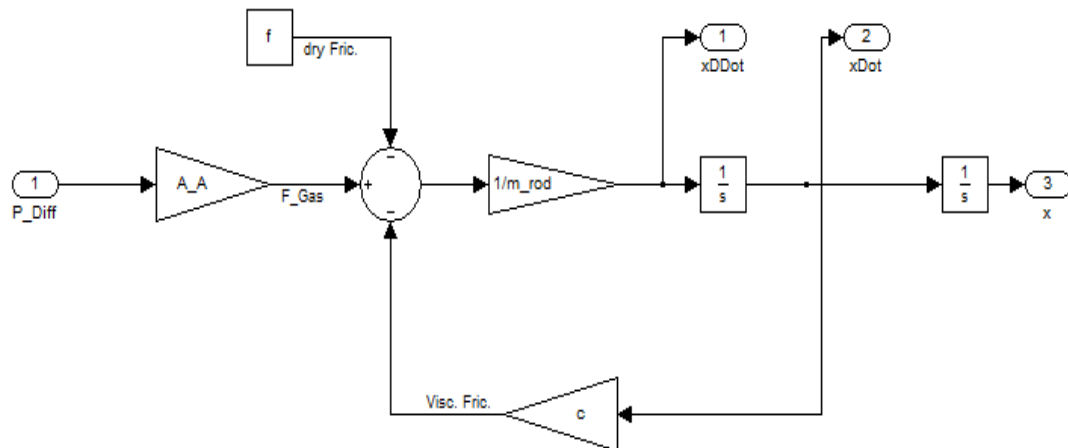


Figure 3-10: Rod Mechanics Subsystem of the Actuator

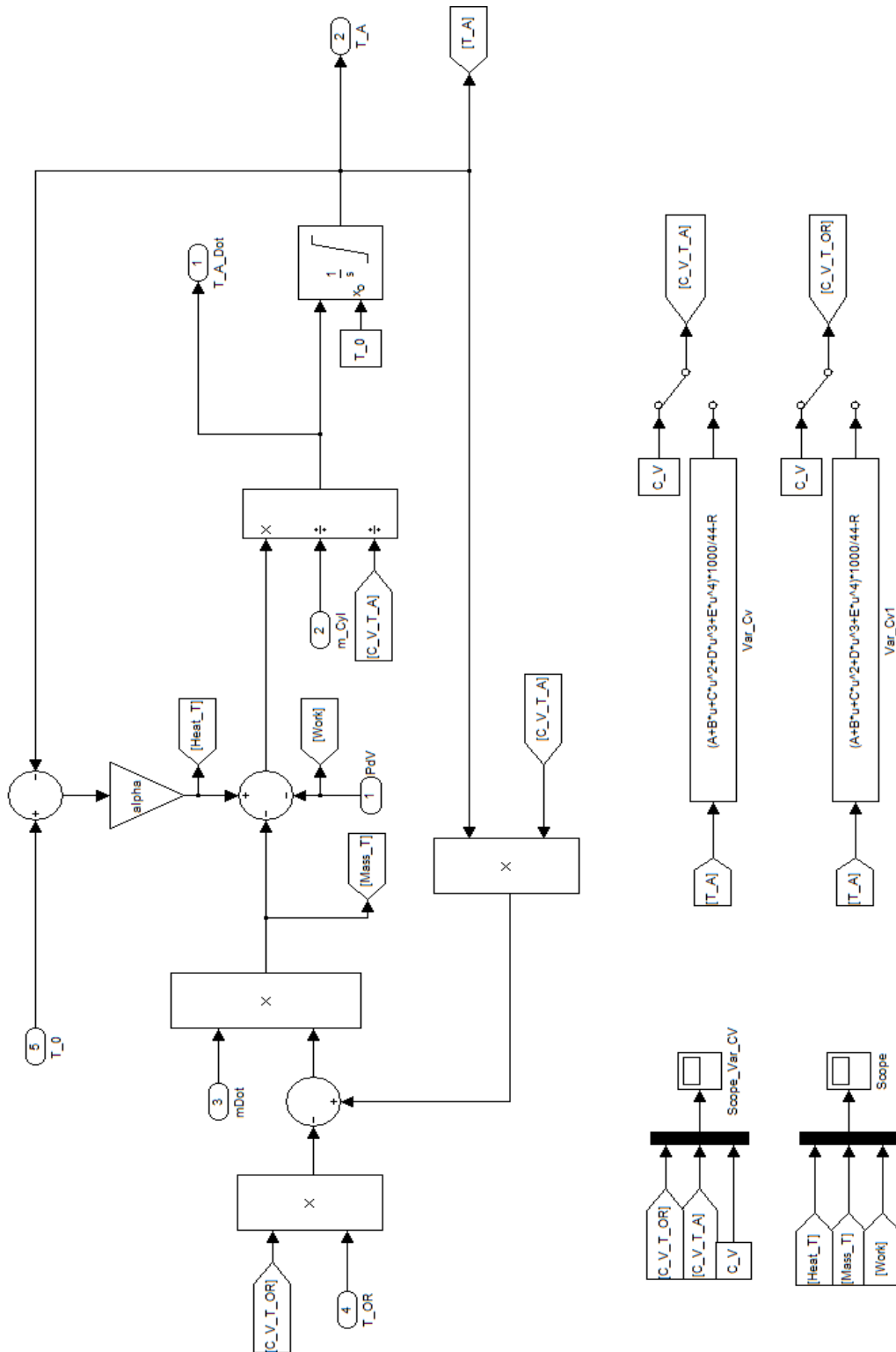


Figure 3-11: First Law of Thermodynamics Subsystem of the Actuator

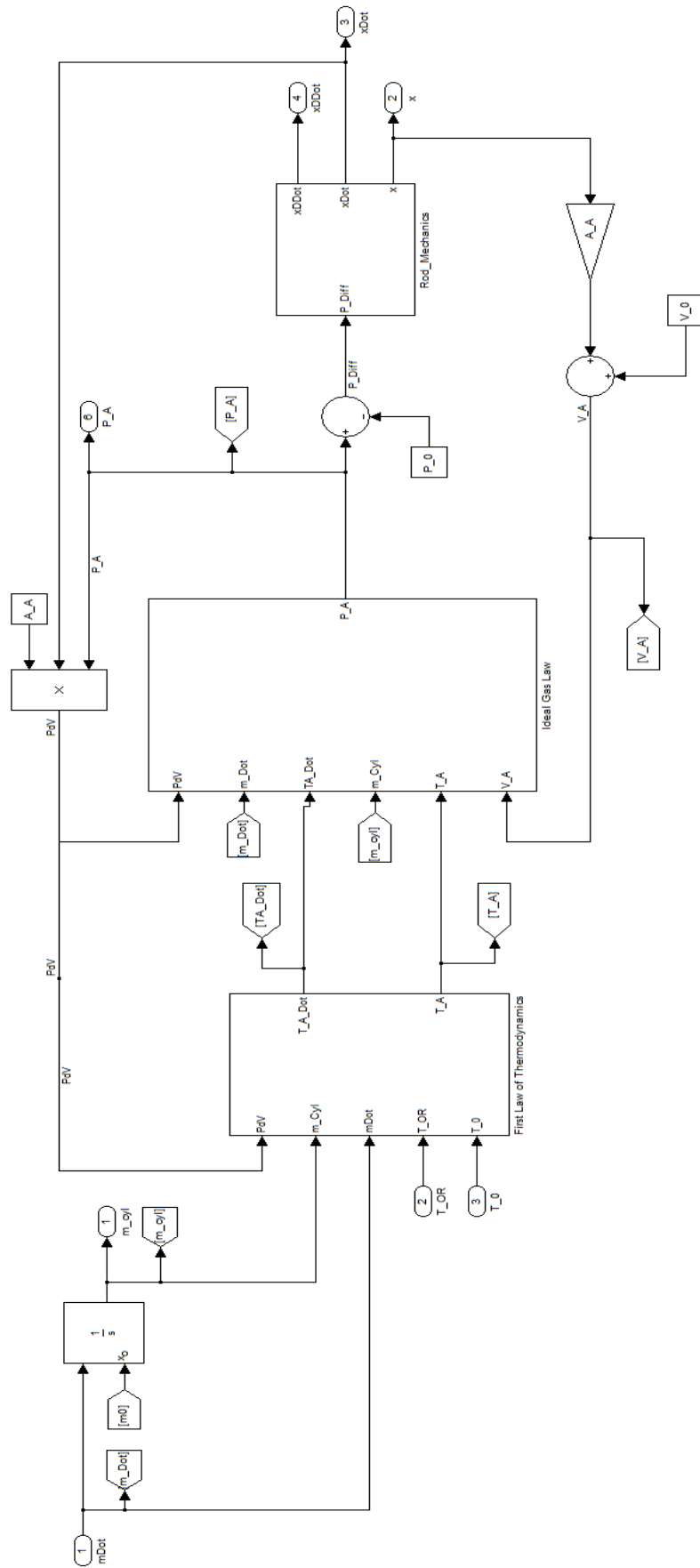


Figure 3-12: Matlab Model of the Actuator

3.4. Matlab Model of the System

Overall Matlab model of the system can be seen in Figure 3-13 as it is in accordance with the proposed model hierarchy before.

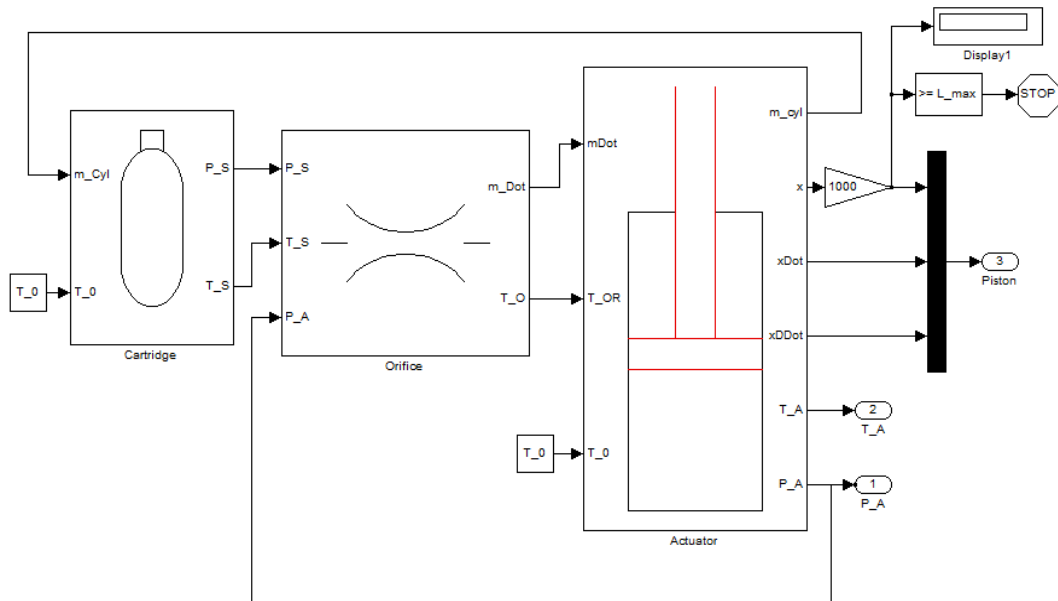


Figure 3-13: Overall Matlab Model of the System

Some constant parameters of the system are quite hard to estimate without prior experimentation or work in the field. The parameters for the heat transfer coefficient [34] and friction coefficients [35] in the actuator are taken from appropriate resources. It is also important to note that both of these are dependent proportionally on cylinder radius. Maximum orifice area is dependent on the CO2 cartridge exit and CO2 cartridge's pierceable part is measured as 3.65mm as shown in Figure 3-14. Yet due to wall thickness of the piercer itself, some of the orifice area would be unusable and the orifice radius is taken as 2.8mm in the analysis. Piston diameter and cylinder length are selected to be as large as possible while cylinder could still be able to fit in the robot; since jump height will increase with both of these parameters.

A base run with the parameters shown in Table 3-1 run and results of this run showing the pressure and temperature in the cylinder and motion of the piston are presented Figure 3-15, Figure 3-16 and Figure 3-17.



Figure 3-14: Measurement of the Maximum Possible Orifice Area of the 12g CO2 cartridge

Table 3-1: Parameters taken for the base run of the Matlab model

Parameter Name	Symbol	Value	Unit
Ambient Temperature	T_0	20	Celsius
Ambient Pressure	T_0	100	kPa
Orifice Area	A_{or}	4.9	mm ²
Stroke Length	s	100	mm
Piston Diameter	D_{pis}	35	mm
Rod Mass	m_{rod}	0.3	kg
Robot Mass	m_{robot}	3	kg
Friction Coefficient	f	$150 \cdot 2\sqrt{A\pi}$	N
Viscous Friction Coefficient	c	$50 \cdot 2\sqrt{A\pi}$	Ns/m
Heat Transfer Coefficient	α	$50 \cdot 2s\sqrt{A\pi}$	W/K

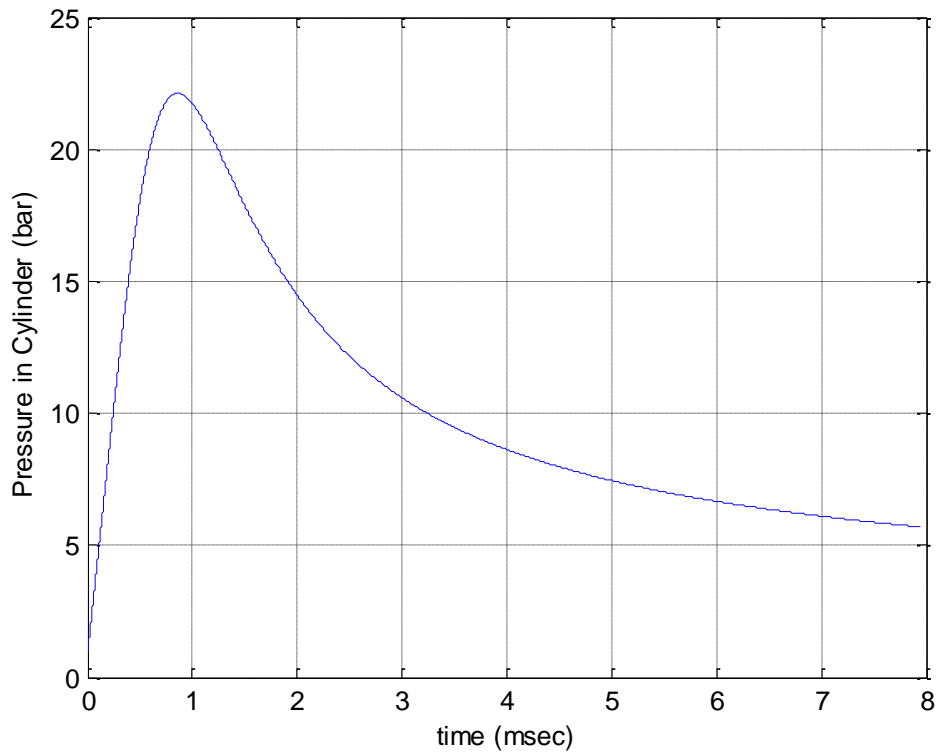


Figure 3-15: Pressure in the cylinder vs. time graph for the base run

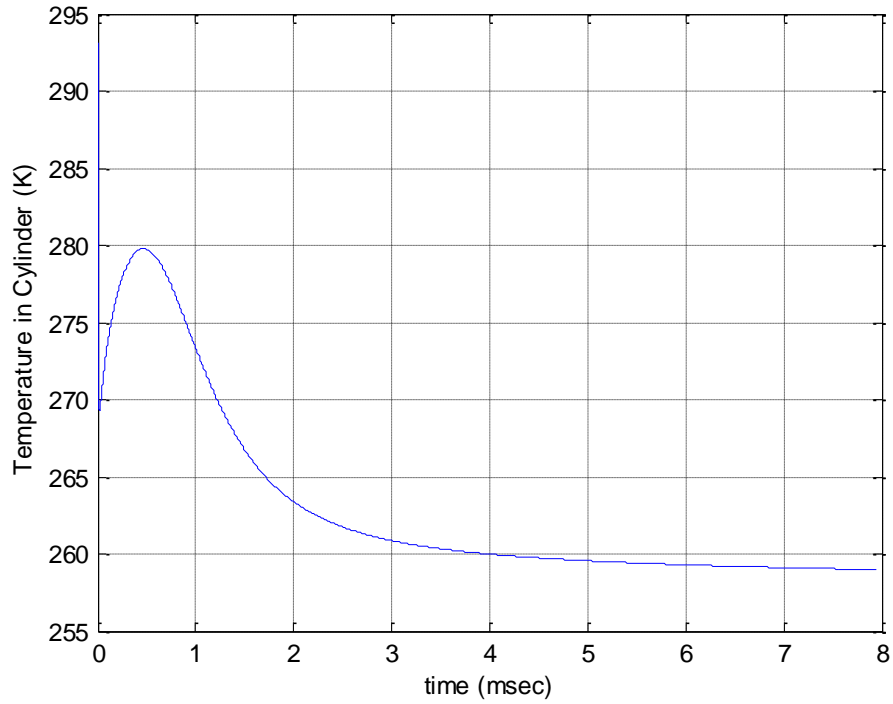


Figure 3-16 Temperature in the cylinder vs. time graph for the base run

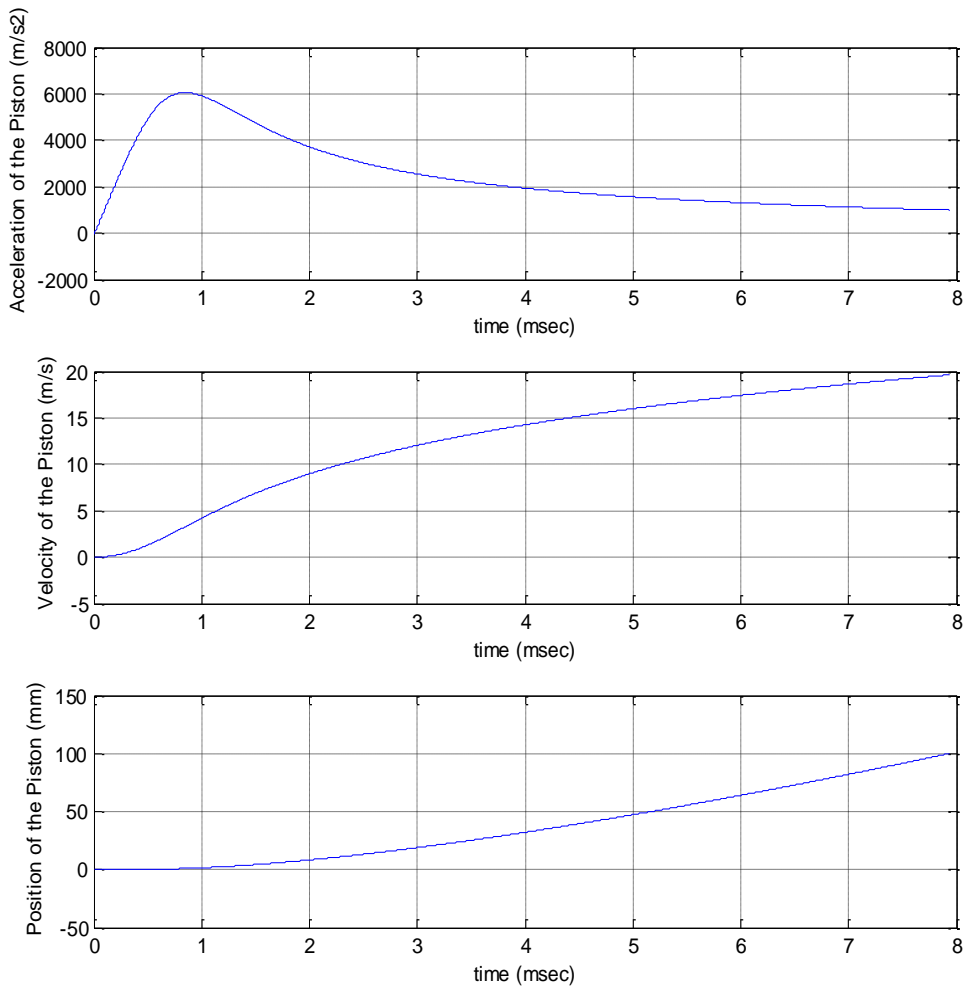


Figure 3-17: Acceleration, Speed and Position of the Piston vs. Time

Velocity of piston reached at the end of 100 mm stroke concludes that a jump of 197 mm could be achieved for a robot with 3kg weight. If a 2kg robot could be constructed, it would jump 442 mm. It should also be noted that both the pressure and the temperature graphics are resulted as expected. Pressure rapidly increases in the cylinder at start, yet after some point it starts reducing since the orifice area limits the gas flow whereas the piston velocity monotonically increases. Temperature crashes down as low as 260K because of the sudden expansion. During the faulty trials solid CO₂ formations were observed by the author, which supports the fact that gas undergoes a low temperature state as a result of the sudden expansion. Also mass of the carbon dioxide consumed in the process is found to be around 6 grams, which is only the half of the tube so constant pressure assumption of the tube is being supported more.

What-if scenarios and the effects of the following parameters are investigated independently:

i) Orifice Area,

Orifice area is the main factor affecting the flow, and it is the reason why the pressure in the cylinder is rather low when compared to the supply pressure. For the robot currently constructed, the orifice area is restricted due to the tube itself. Yet if larger tubes were utilized such 88g, much more orifice area could have been achieved. With other parameters kept constant, Figure 3-18 shows the huge impact of the orifice area on the performance of the system.

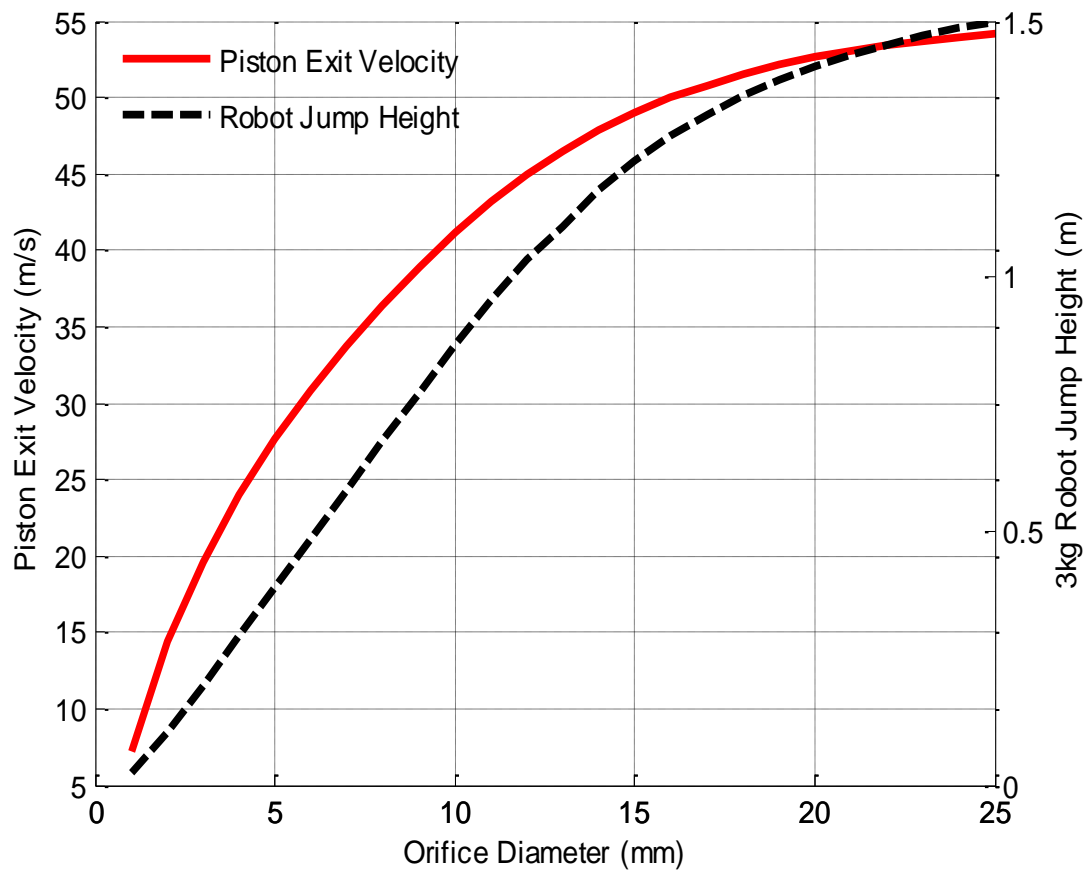


Figure 3-18: Orifice Diameter vs. Robot Jump Height

ii) Ambient Temperature,

It is quite obvious from the triple point diagram that the initial temperature of gas has a very big influence on the vapor pressure. In fact, in cold temperatures jump height is halved as it can be seen in Figure 3-19.

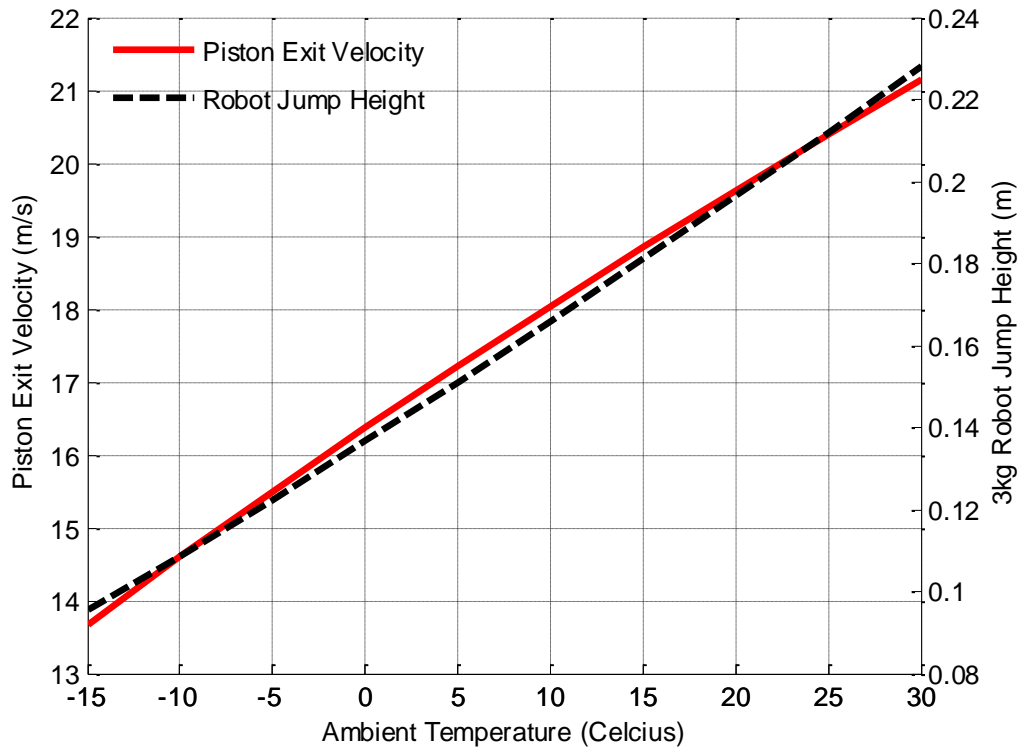


Figure 3-19: Initial Cartridge Temperature versus Piston Exit Velocity and the Robot Jump Height

iii) Piston Diameter and Stroke Length

In the preliminary analysis part, increasing the diameter of the actuator is shown to increase the jump height directly; as net force on piston would increase. Yet, when compressibility was taken into account; Eq. (28) shows that the piston area is also inversely proportional with the pressure build up rate, so an optimum point must exist for this parameter. Same principle also applies for the stroke length.

The model was simulated for different piston diameter and stroke lengths and Figure 3-20 was constructed. Of course, this is the case for 2.8mm given orifice area, since it must not be forgotten that this phenomenon is the result of limited mass due to presence of an orifice. An increase in the orifice area would bring the locus of the maxima of the graphs towards higher piston diameters and this fact can be concluded by comparing Figure 3-20 and Figure 3-21.

With these results, it can be concluded that to get the best out of the stored gas; orifice area and piston area must be designed as unit or they would degrade each other's performance.

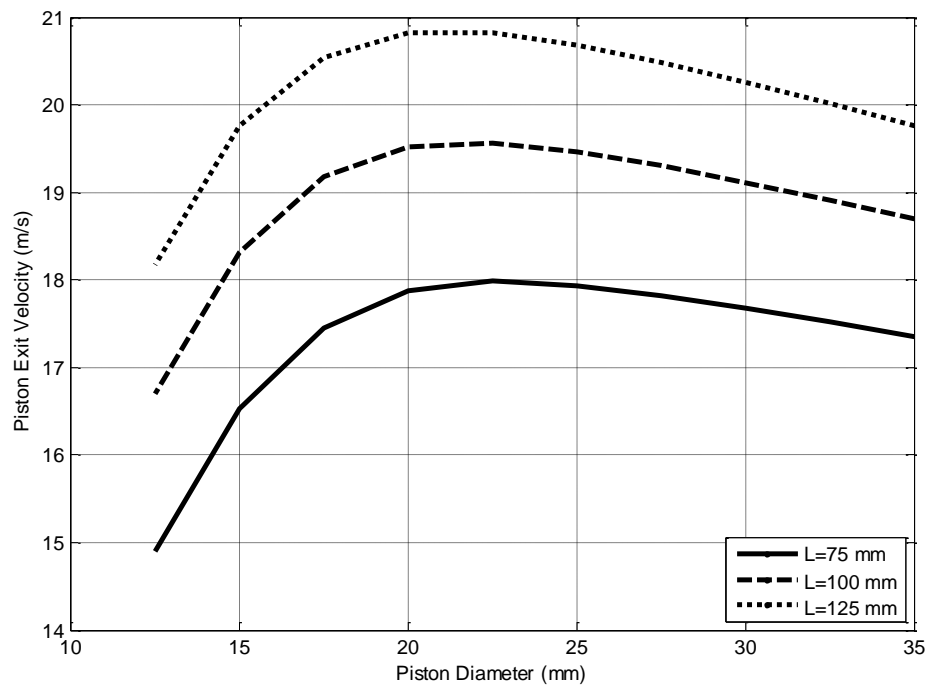


Figure 3-20: Piston Diameter versus Piston Exit Velocity at Various Stroke Lengths and 2.8mm Orifice Diameter

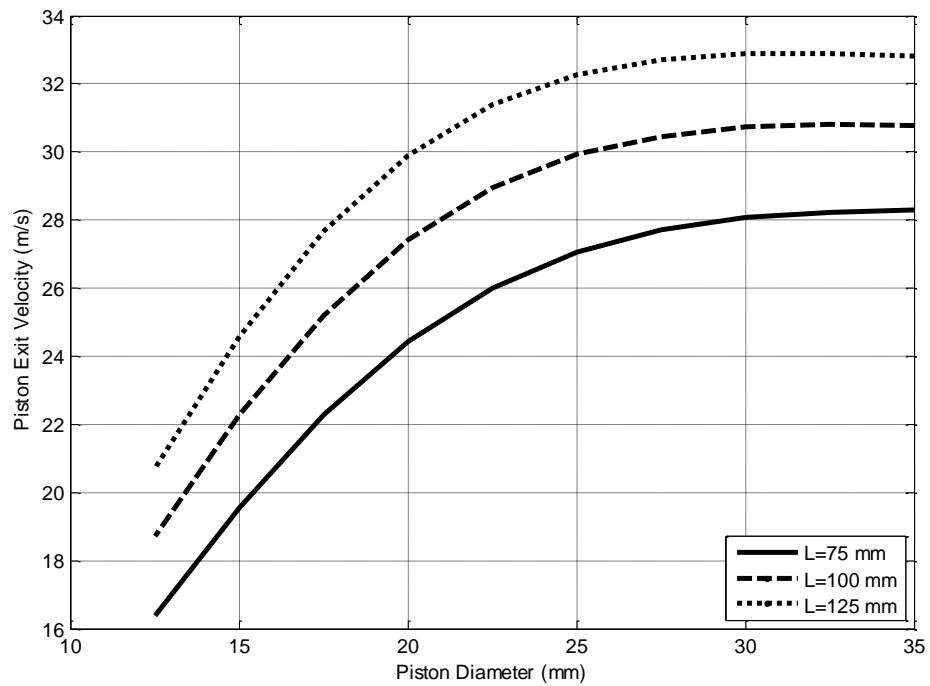


Figure 3-21 Piston Diameter versus Piston Exit Velocity at Various Stroke Lengths and 6mm Orifice Diameter

3.5. Mechanism to Pierce the Cartridge

Now that the piston cylinder arrangement is designed and one single time use cartridge is selected; the cartridge must be pierced to be used. To achieve this, a hammer mechanism is to be constructed, where stored potential energy could be released at an instant to lance the cartridge. Unfortunately, the space after the cartridge is mainly occupied with wheel motors and the main board, the mechanism must be built under the cartridge. To convert the rotational shaft motion to linear motion, a screw mechanism is utilized which charges the main spring. When the required load condition is achieved, the hammer is released; driving a slider crank mechanism which strikes the lance into the cartridge.

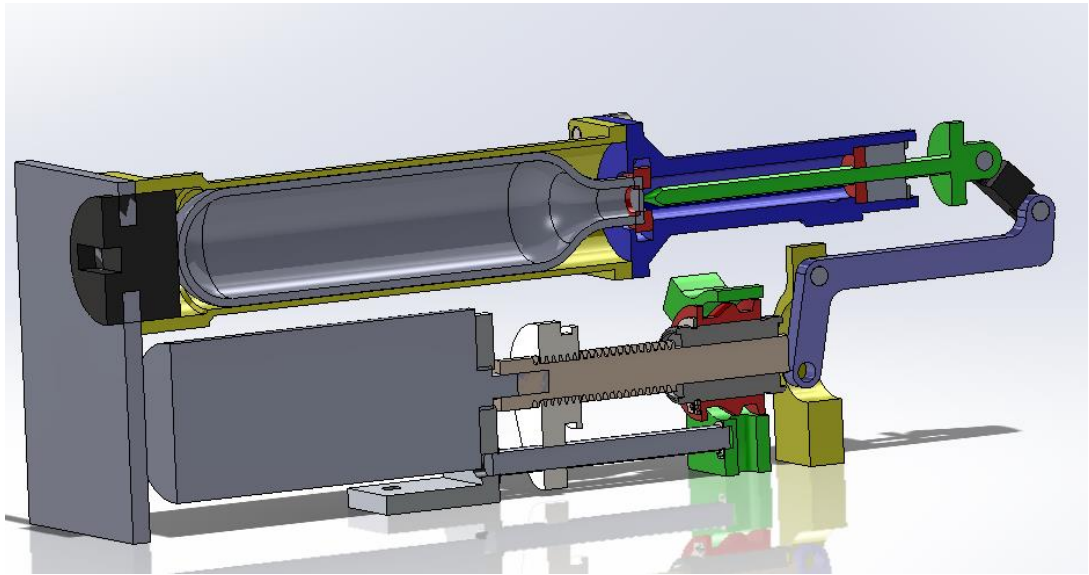


Figure 3-22: Overall CAD Drawing of the Piercing Mechanism

3.5.1. Screw Part of Piercing Mechanism

In this part the main aim is to charge a spring which will strike a hammer into the crank of the next part. The motor turns the screw, and nut starts to load the spring since hammer, which is shown with red color in Figure 3-23, cannot move without a certain amount of force due to ball detents. Assuming friction between ball and hammer is zero, then the force needed to release the hammer can be found by;

$$F_{rel} = F_{spr,b} \cdot \tan \alpha$$

where $F_{spr,b}$ is the force exerted by the spring in the detent, and it is adjustable by the means of a setscrew which is underneath it. Angle α is simply the detent angle. Also as shown in Figure 3-24 ball is still exerting force on the hammer, even after the detent; but this time in the desired direction and it is given by;

$$F_{des} = F_{spr,b} \cdot \tan \beta$$

Motion of the hammer itself is 6mm, and the total force the hammer can exert is the summation of the main spring and detent spring forces.

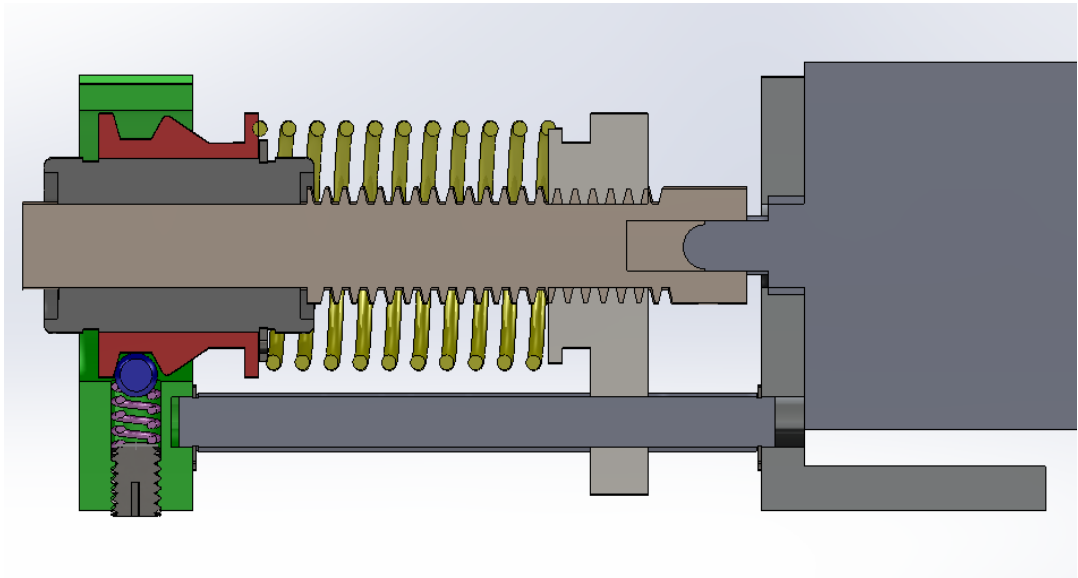


Figure 3-23: Cut-Away Section of the Screw Part of the Piercing Mechanism

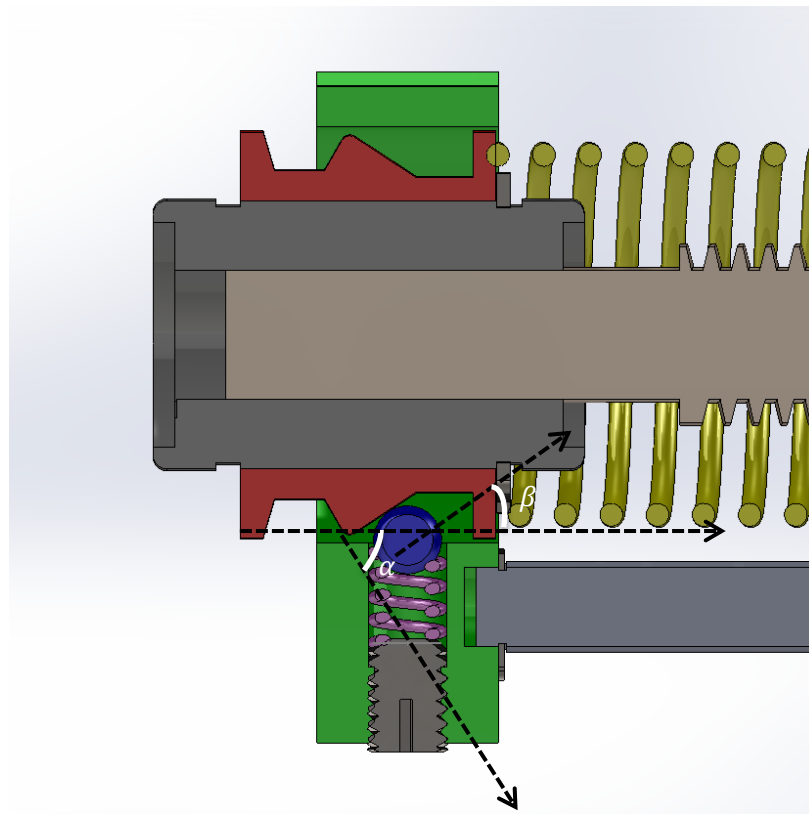


Figure 3-24: Due to Shape of Hammer, Detent Ball Exerts a Force in the Desired Direction

3.5.2. Slider Crank Part of Piercing Mechanism

When the hammer hits the crank of the slider mechanism, it moves the lance into the carbon dioxide cartridge to pierce the cartridge. Kinematically speaking, mechanism can be seen in Figure 3-25 and forces acting on the bodies are on Figure 3-26. Although mechanism acts quickly, dynamic forces are neglected since they are expected to be very small compared to the piercing force. Friction forces are also ignored for the same reason. With these assumptions, notice that link 3 is a two force member so it only transmits forces along its path.

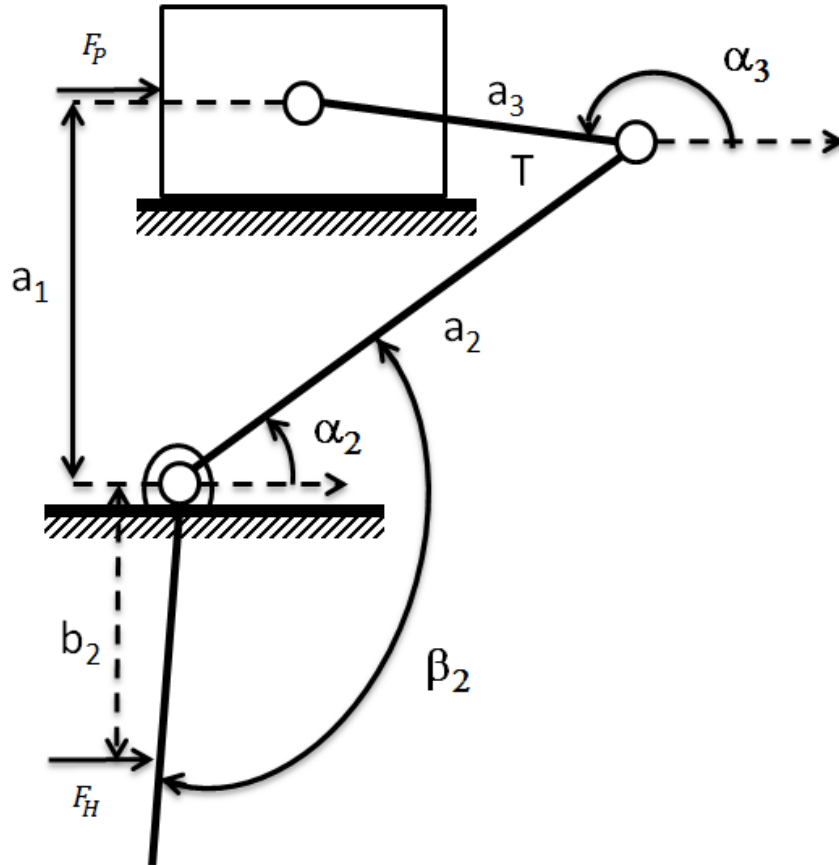


Figure 3-25: Skeleton Diagram of the Slider Crank Mechanism

Angle of link 3 with respect to ground, α_3 , can be found by;

$$\alpha_3 = \pi - \arcsin\left(\frac{a_1 - a_2 \sin(\alpha_2)}{a_3}\right) \quad (30)$$

Summation of the moments of must be zero for link 2 so;

$$F_H \cdot b_2 = F_{32} \cdot a_2 \cdot \sin(\alpha_3 - \alpha_2) \quad (31)$$

And using free body diagram for the slider piercing force F_p can be calculated as;

$$F_p = -F_{23} a_3 \cos \alpha_3 \quad (32)$$

Using (31) and (31)(32) it can be calculated that the overall multiplication factor between the force from hammer and lance is;

$$M = \frac{F_p}{F_H} = \frac{a_3 b_2 \cos(\alpha_3)}{a_2 \sin(\alpha_3 - \alpha_2)} \quad (33)$$

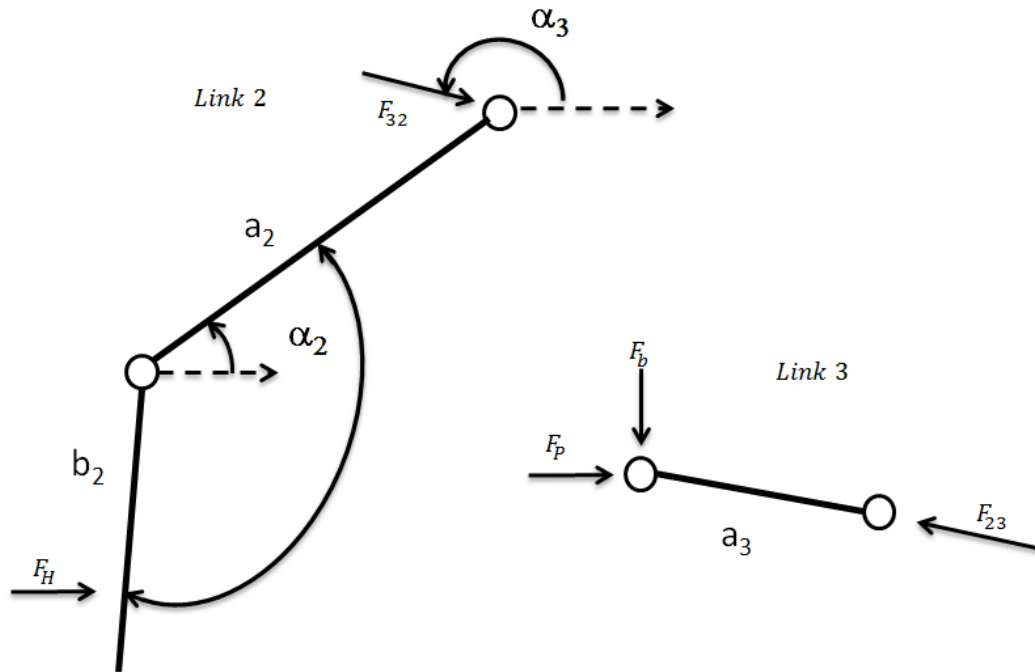


Figure 3-26: Free Body Diagrams of the Link 2 and Link 3

Equation (33) shows clearly that while α_3 is kept close to π , $(\alpha_3 - \alpha_2)$ should be as small as possible. Also, α_3 heavily depends on $a_1 - a_2 \sin(\alpha_2)$ so link lengths should be selected such that $a_1 - a_2 \sin(\alpha_2)$ is as small as possible. Results showing the best possible link lengths without collision with environment are shown in Figure 3-27 where link lengths are selected as;

$$a_2 = 40 \text{ mm} \quad a_3 = 13 \text{ mm} \quad a_1 = 15 \text{ mm} \quad b_2 = 11.5 \text{ mm}$$

3.5.3. Actual Piercing Mechanism

According to the determined link lengths, piercing mechanism was manufactured and most of its components are demonstrated in Figure 3-28. Unfortunately constant problems at the detent part of the mechanism were experienced. Balls which are supposed to release the hammer when sufficient force was applied started to wedge between hammer and static holder; due to marks and manufacturing errors in both pieces. Another problem of the design was that the striker could not open the orifice as much as expected and in fact maximum hole opened on the cartridge with this mechanism was measured to be 1mm.

Since the problems could not be solved, the author started using the mechanism not as a piercer but as a valve with just a little change. A small conical piece with a hole in its center was placed where the striker hits, and with this piece cartridges were pierced by tightening a screw from back. Striker worked in opposite way; it plugged the hole of the new conical piece; thus obstructing the flow of CO2. When the hopping action was required; striker were pulled back to open the flow.

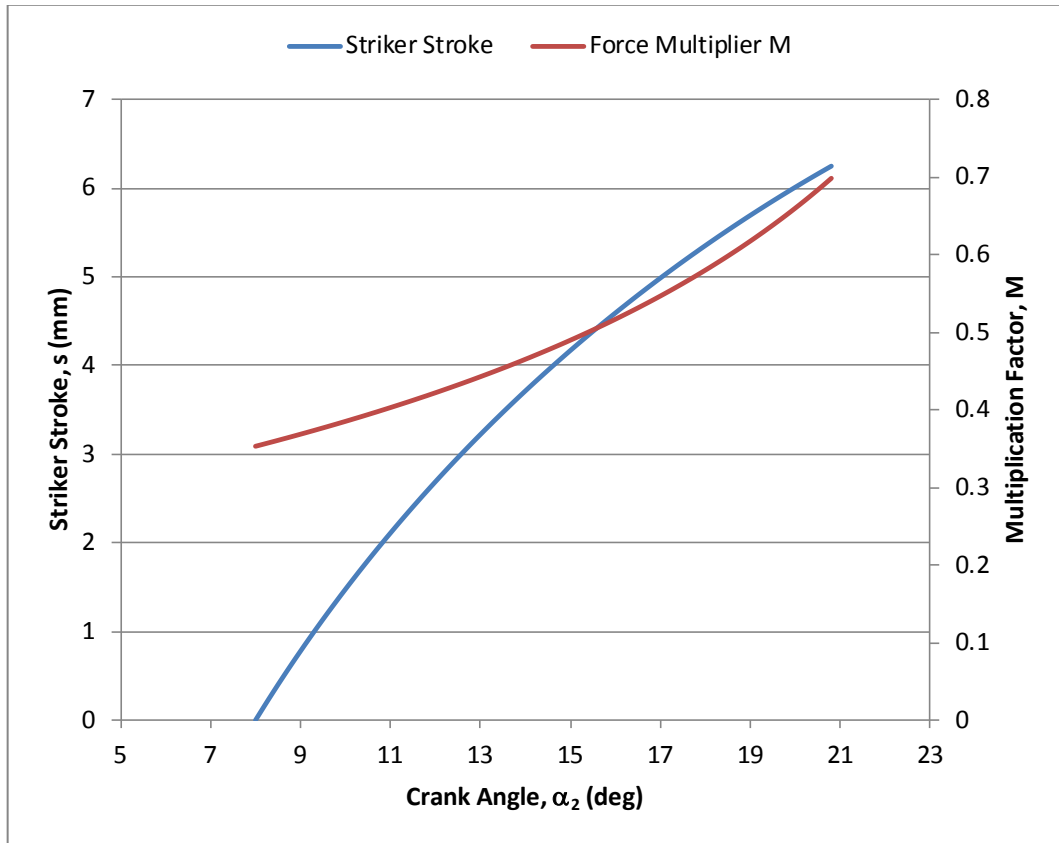


Figure 3-27: Striker Stroke and Multiplication Factor vs. Crank Angle



Figure 3-28: Components of the Manufactured Piercing Mechanism

3.6. Tilt Mechanism

Piston cylinder arrangement can provide the power to jump yet the piston must be brought to an appropriate angle with the ground to give the necessary thrust. For this problem there exists two types of general solution; either rotating the piston with respect to robot or rotating the whole robot with respect to the ground and both of these are sketched in Figure 3-29.

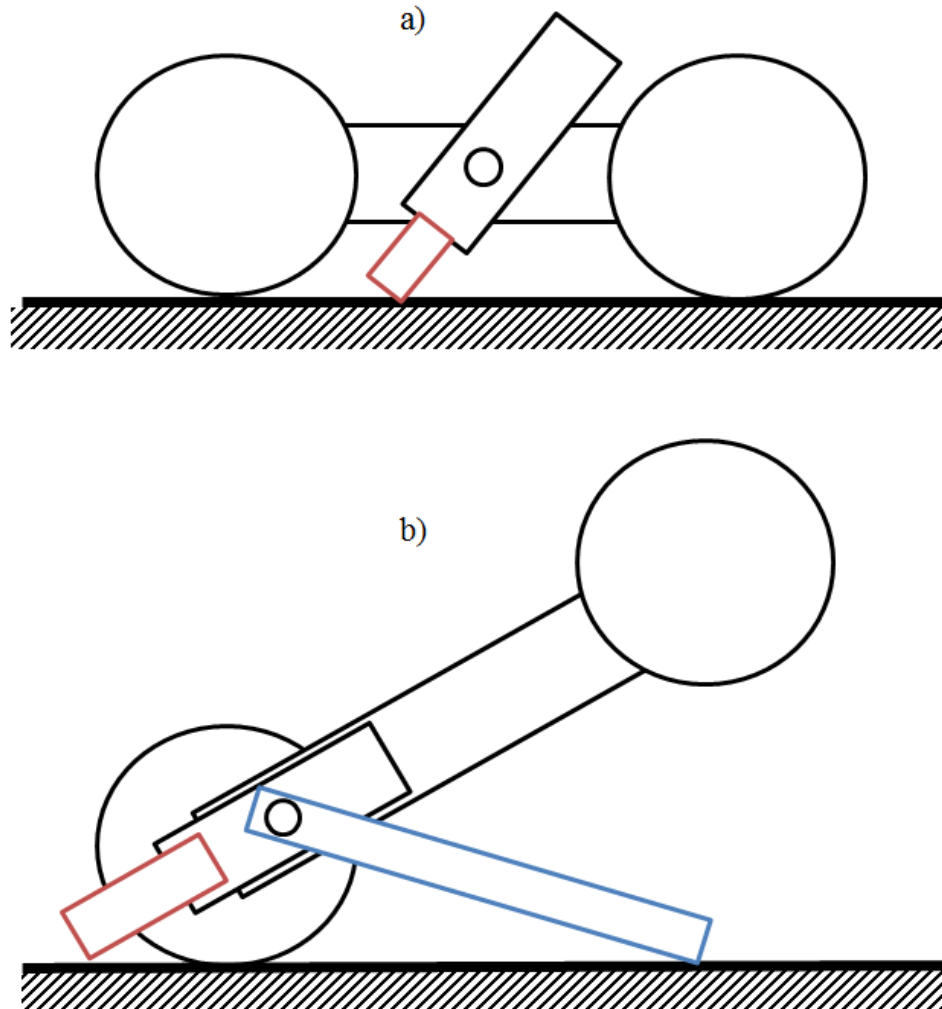


Figure 3-29: Two Possible Design Concepts for Providing Thrust a) Rotating Piston with Respect to Ground b) Rotating Robot with Respect to Ground

Main advantage of just turning with piston cylinder arrangement is the obvious fact that the just rotating the cylinder requires much less energy and power than rotating the whole robot. Also if the center of mass of the robot is at the center of the pivot, jumping will be very well balanced. Yet it has a huge disadvantage of eliminating lots of usable space, as the cylinder sweeps through most of robot. In addition, the piston would be closer to the ground, meaning lower stroke lengths, thus limiting the jump capability. On the other hand, rotating the whole robot with two legs outside of the chassis is better if the robot is standing on the terrain with roll angle other than zero. With these comparison in hand, rotating the whole robot with two legs concept is selected.

3.6.1. Analysis of Tilting Mechanism

Rotating the whole robot using a “leg mechanism” can be modeled using a prismatic and revolute joint for the wheel as in the skeleton diagram shown in the Figure 3-30.

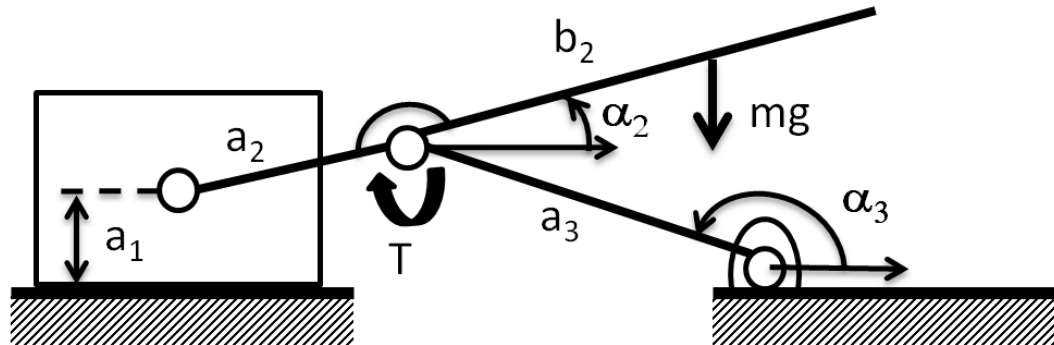


Figure 3-30: Skeleton Diagram of the Tilting Mechanism

Drawing the free-body diagram of the system as shown in Figure 3-31 and friction force, F_{fr} , is expected to be very low since rear wheels are free to rotate on the ground. Another conclusion of the free body diagrams is the fact that if necessary rear wheels can be used to provide more power for this mechanism since that providing power to wheel in the clockwise direction, will create a force in the same direction of F_{fr} , however this will make the tilt control worse and complicate the algorithm. Omitting the F_{fr} static force equilibrium conditions leads to equations (34) and (35) and robot body just becomes a lever.

$$\sum M_{@ Robot F.B.D.} = F_{32} \cdot a_2 \cdot \cos \alpha_2 - m \cdot g \cdot (a_2 + b_2) \cos \alpha_2 = 0 \quad (34)$$

$$\sum M_{@ Robot F.B.D.} = F_{32} \cdot a_3 \cdot \sin \alpha_3 - T = 0 \quad (35)$$

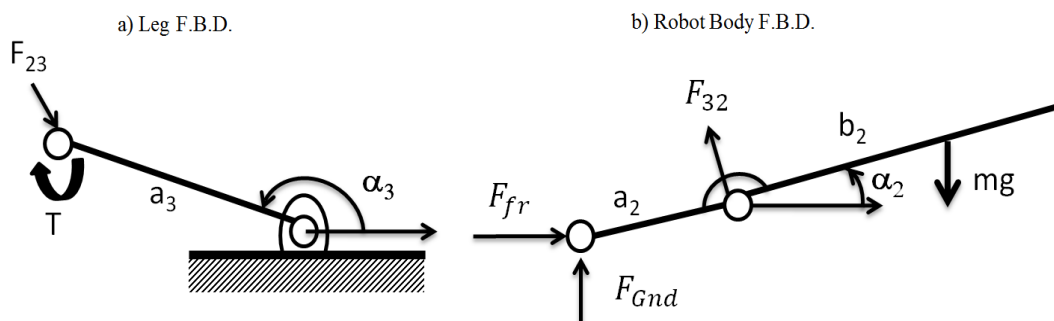


Figure 3-31: Free Body Diagrams of a) Leg and b) Robot Body

From simple geometry, the angle α_3 which is the angle between the tilt foot and the ground can be found in (36). Also, for the robot to be able to tilt up to 90 degrees $a_3 \geq a_2 + a_1$ condition must be satisfied.

$$\alpha_3 = 180 - \text{asin}\left(\frac{a_2 \sin \alpha_2 + a_1}{a_3}\right) \quad (36)$$

Using (35) and (36), torque required to drive the system is derived in (37). Parameter a_1 is the wheel radius and it has been already determined in the previous section. Also, b_2 is the distance of center of mass to bearing center, which is also pre-determined. Another fact that is a_2 and a_3 are not completely independent of each other, since total length of $a_2 + a_3$ must be less than distance between front and rear wheels.

$$T = m \cdot g \cdot \frac{(a_2 + b_2)}{a_2} \cdot a_3 \cdot \sin\left(\frac{a_2 \sin \alpha_2 + a_1}{a_3}\right) \quad (37)$$

3.6.2. Actual Tilt Mechanism

In the actual system, a symmetric tilt mechanism is constructed on both left and right sides of the robot for two reasons: firstly, it was more costly and space consuming to drive the both sides from the same motor and secondly the twin system allows tilting on a inclined plane since both feet does not touch the ground at the same shaft location. CAD drawing of the right side of robots tilt mechanism is shown in Figure 3-32,

Best parameters achieved for a_2 and a_3 are 30mm and 125mm respectively. Also, mass center is tried be kept as close to tilt bearings as possible, and final result is that mass center is around 40mm apart from the bearings. An appropriate motor is selected and installed to the mechanism, thus concluding the design process. Manufactured mechanism can be seen in Figure 3-33 during the conducted tests.

Another challenge of the design was to keep this mechanism as light as possible. Despite the attempts, mechanism contributes 430g to the weight of the robot which is quite significant. Weight list of the components can be examined in the following Table 3-2.

Table 3-2: Weight List of the Components in Tilt Mechanism

Tilting Subsystem	Amount	Unit Weight (g)	Total Weight (g)
Tilt Motor	2	95.6	191.2
Motor Shaft Bushing	2	2.0	4.0
Bevel Gear	4	17.0	68.0
Motor Bracket	2	6.6	13.2
Tilt Shaft	2	9.6	19.2
Tilt Foot	2	11.7	23.4
Spacer	4	2.0	8.0
Flange Bearing	2	26.5	53.0
Block Bearing	2	25.0	50.0
Tilt Mechanism Total			430

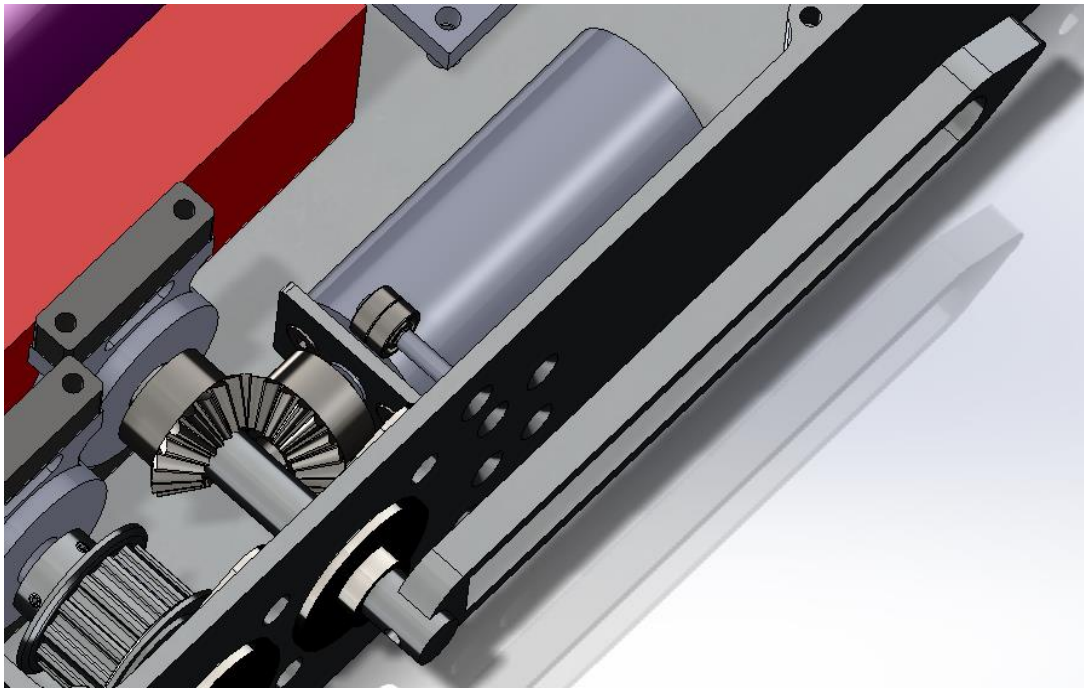


Figure 3-32: CAD drawing of the Tilt Mechanism

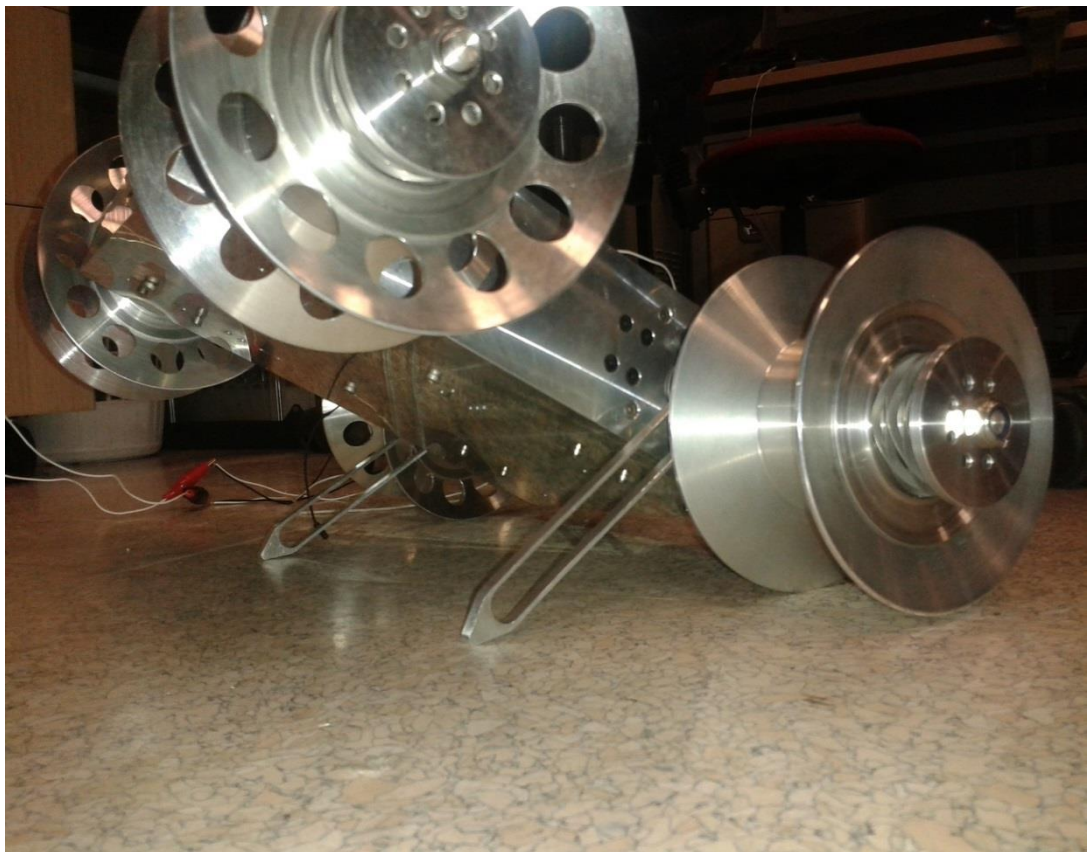


Figure 3-33: Tilt Mechanism in Action during Tests

3.7. Results of the Overall Hopping System

Overall hopping system performed reasonably in terms of jump height yet other problems occurred. Jump height was measured by utilizing a graph paper at a perpendicular surface near the robot. To seal the robot as good as possible liquid seal were applied to the relevant locations and connections. Piston does not have a O-ring or other means of sealing, since it was experimentally found out that friction induced due to sealing is worse than leakage. Cylinder was made from Aluminium 7075-T651 and piston was made from steel. Piston was grinded to tolerances, yet cylinder was not honed or subject of any other super-finishing operation.

Robot weight was also measured to be 3.5kg before the jump as shown in Figure 3-34. The camera, compass module and upper plate of the robot were the only missing components, and they all account for only around 120g.

Figure 3-35 demonstrates a jump which reached a height of 185mm.



Figure 3-34: Measurement of the Weight of the Robot



Figure 3-35: Figure Showing the Actual Jump of the Robot at its Highest Point

Unfortunately, after a few jumps, low cost gearbox of the tilt mechanism broke down, and when the problem was investigated, the gears in the gearbox were fractured. From this point on tests had to be performed by manually tilting the robot.



Figure 3-36: Fractured Gears of the Left Tilt Motor's Gearbox

CHAPTER 4

ELECTRONICS SYSTEM

4.1. Introduction

The electronic system of this robot is another challenging task which needs to be carried out to be able to run the robot. It is composed of many elements, where every single one of them requires special attention to be able to run them. The author has limited amount of time, money and energy thus components were selected only if they are affordable and rather easy to run. As this design is just a prototype rather than a mass manufactured product, whole electronics system is based on getting a prototyping board for the microcontroller and connecting other devices on it by soldering or other means.

4.2. Microcontroller And Wireless Communication Board

Selecting an appropriate microcontroller board is the most important part of the electronics of this robot. There are quite a few alternatives in the market with different price range and abilities, yet the Digi Electronics Rabbit RCM5400w which is shown in Figure 4-1 and its prototyping board seemed to be best option for the author.



Figure 4-1: Rabbit RCM5400w Board

The board can communicate with the standart 802.11g 2.4 GHz Wi-Fi networks so it can be transfer the data from camera to PC very effectively. Also, it has its own RF circuitry, antenna, and power supply for the antenna so its Wi-Fi channel is ready to use. Moreover,

the board has 4 PWM outputs for driving the motors and incremental encoder and input capture abilities for reading feedbacks. In addition to these, the prototyping board has onboard voltage regulators on its own so that it can operate on different voltage levels without the need of additional circuitry. Another requirement, RS-232 channel for communicating with the compass module is also readily provided. Prototyping board has enough space for motor drivers to be mounted and it also provides excess 5V for feeding the compass module. Dimensions of the prototyping board (97x103 mm) are a bit larger than the authors wishes yet making the chassis a few millimeters longer cannot be even considered as a tradeoff when compared to designing and manufacturing a new printed circuit board. As a result cabling was messy, as seen in Figure 4-2 yet it was only a few hours of work for the author.

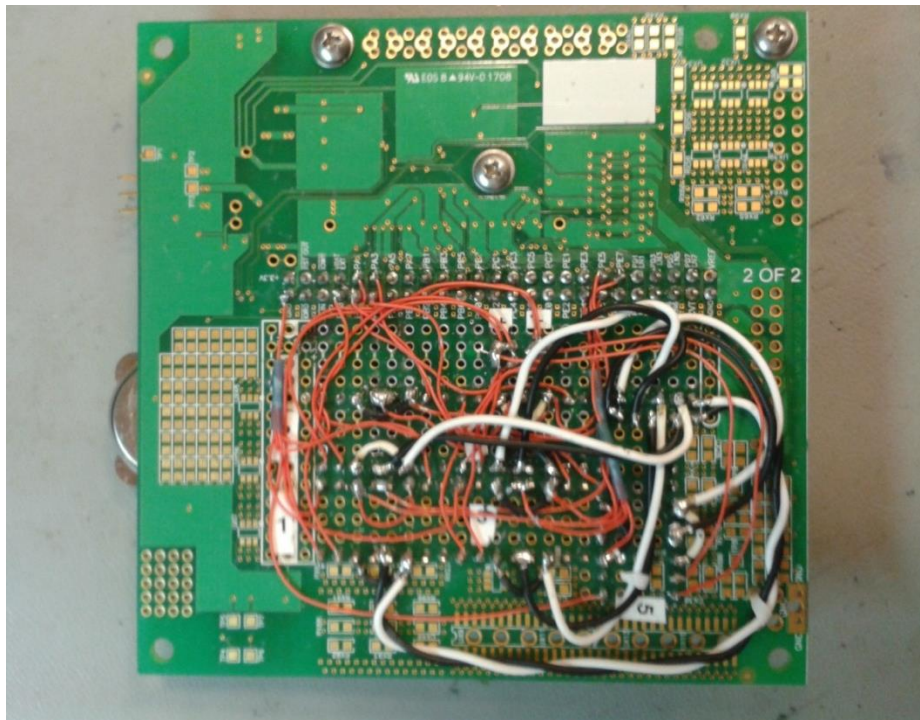


Figure 4-2: Cabling Work Done at the Back Side of the Prototyping Board

Although suspension system does most of the work to absorb the impact energy when the robot hits ground; it is still better to be safe than sorry, and shock protection for the boards should be supplied. Hard disk drive mounts and other low pass gel absorbers are searched, yet the gel absorbers are extremely expensive (more than 10\$ each, approximately 50\$ to protect the PCB), especially when bought in small quantities. So, the boards are mounted with O-Rings [36] to provide old fashioned and cheap anti shock protection.

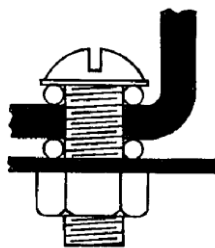


Figure 4-3: Mounting the PCB with the O-Rings [36]

4.3. Battery

Operating voltage of the robot is selected to be 7.4V has the advantages of

- 6V motors can be used and they are much cheaper and easier to find compared to their 12V counterparts
- TI DRV8833 integrated circuit can be used (see section 4.4)
- Rabbit 5400w prototype board has LM2575 integrated circuit connected to its voltage input which can work with 7.4V

Actual battery is bought from “Türk Hava Kurumu” which is national aviation institute of Turkey. Their batteries are heavily used in model airplanes and known to be quite well qualified. The actual battery [37], shown in Figure 4-4, has the capacity of 3400mAh and its size is 110x34x20 mm which well suits the robot of this size. Additional details about the battery can be obtained in section A.4.

Also, since the Li-Po batteries cannot be charged by directly connecting to a power supply, a balanced charger as shown in Figure 4-5 is necessary to charge them.



Figure 4-4: Li-Po Battery used in the Robot



Figure 4-5: Balanced Battery Charger

4.4. Motor Drivers

To be able to control the DC motors, a driver circuitry is necessary. For this purpose, instead of designing and manufacturing his own circuitry, the author decided to use IC motor drivers' breakout boards. Texas Instruments' DRV8833 was selected after the search for an appropriate driver which can work efficiently at the required battery levels. Schematic and connections of the breakout board can be seen in Figure 4-6 and when the outputs are paralleled, the driver can supply 3A continuous and 4A peak currents, which is appropriate for the selected motors. Datasheet of the integrated circuit can be found in section A.4.

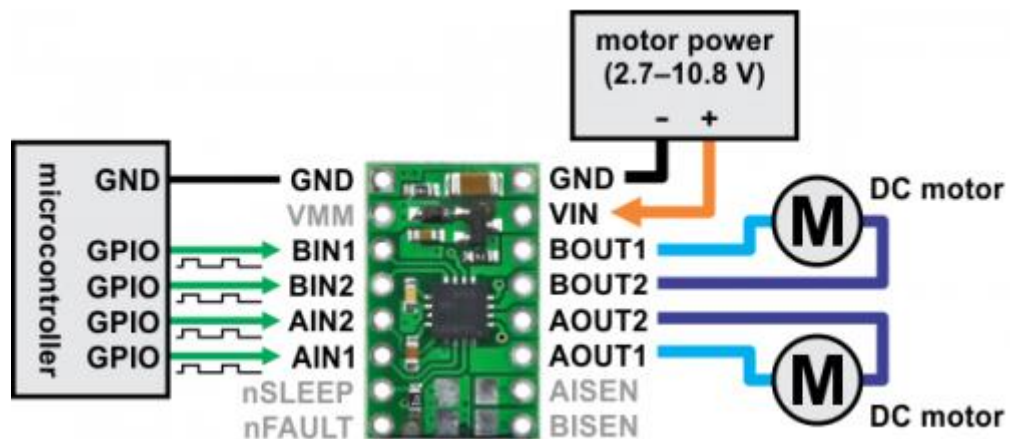


Figure 4-6: Schematic of the Motor Driver Breakout Board

Although 5 different motors are controlled and the microcontroller has only 4 PWM modules, actually at any instant no more than 2 motors are operating. This is where the sleep pin kicks into action; it has become the key to control the motors with same PWM outputs. For instance, left wheel and left foot motors are connected to the same PWM output of the Rabbit 5400w, but when the wheels are operating the sleep pin of the feet motor becomes high, shutting the driver down. Same theory applies to the right side motors and the hammer motor.

4.5. Compass Unit

Compass unit has two main duties;

- Provide heading readings to be able to make robot go straight
- Provide pitch reading for the tilting mechanism to work correctly

Both of these readings does not have to be in high resolution or high accuracy but the unit must be able to withstand some shock. The author has selected Ocean Server OS 5000-S compass unit which has a rugged design and can survive up to 10000g shocks. The unit is shown Figure 4-7 and its place in the robot is in Figure 4-8. It is quite close to the wheel motors but the sensor can be easily hard iron and soft iron calibrated using the software it provides; which is one of the main reasons why it was selected. Full datasheet of the unit can be found in section A.6.



Figure 4-7: Ocean Server OS-5000S Compass Unit

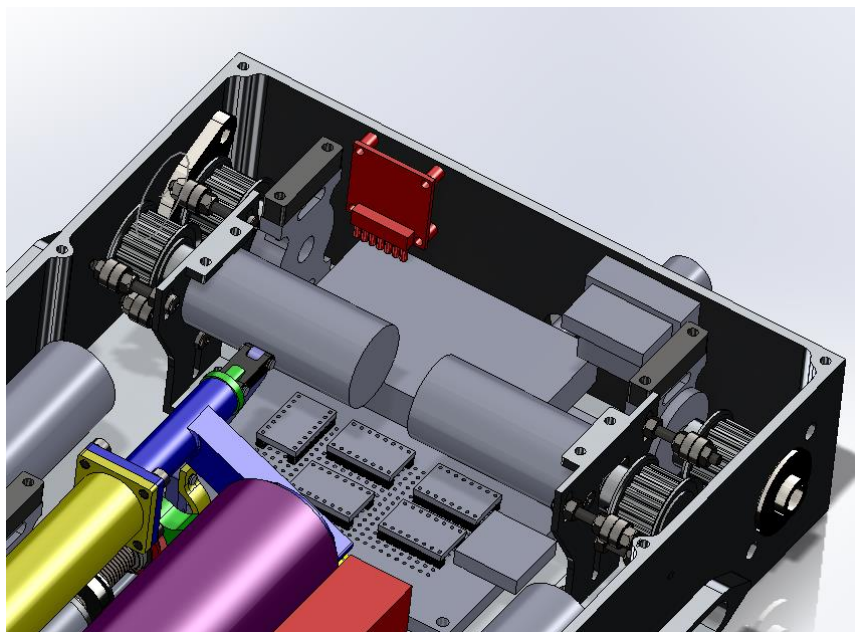


Figure 4-8: Placement of the Compass Unit inside the Robot

4.6. Software

Rabbit 5400w is programmed with Dynamic C which is a design environment “specially designed for programming embedded systems, and features quick compile and interactive debugging” [38]

Control algorithm used in the robot has no feedback information from any of the motors in the system. The only feedback is the compass module and all of the control loops are closed from the feedback of the compass.

4.6.1. Graphical User Interface for Test Purposes

To be able to run and test the robot using the Wi-Fi network, a graphical user interface is prepared in C#. A screenshot from the GUI can be seen Figure 4-9 and it basically lets the

author to control the robot from the joystick while observing the feedbacks. Real time graphic is constructed using the interactive visualization tools taken from “D₃-Dynamic Data Display” [39] code.

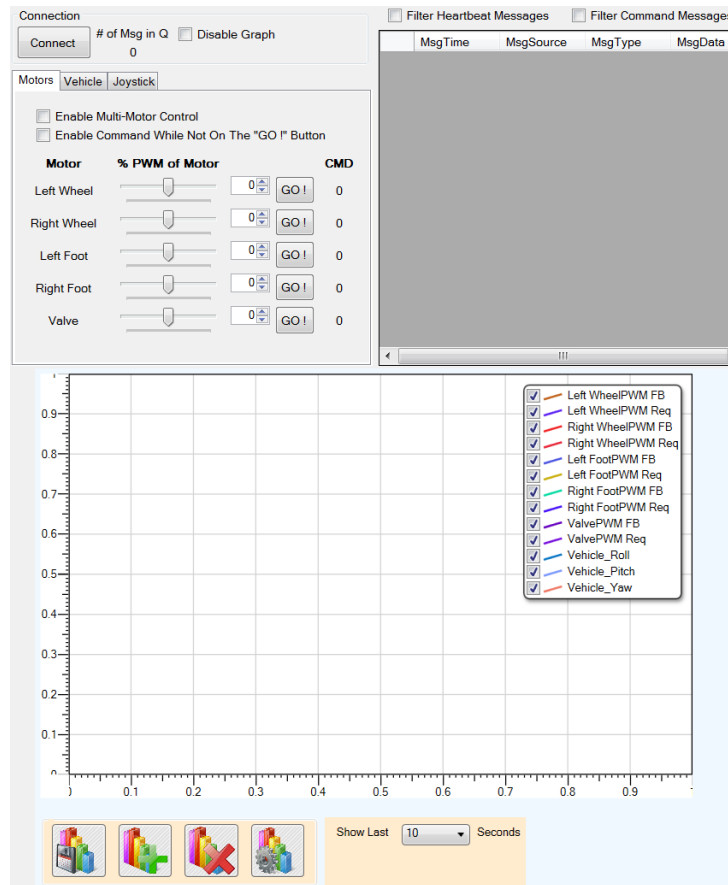


Figure 4-9: A Screenshot of the GUI Designed for Testing the Robot

4.7. Remarks

The overall approach for the electronics design of the robot gave quite good fruits. Being able to solder necessary circuits to the prototype has saved the author from the effort of making new printed circuit boards. Compass module worked well enough for the simple control of the wheels and tilting mechanism. Although a camera was obtained, it could not be used inside the system due to time constraints.

CHAPTER 5

CONCLUSION AND RECOMMENDATIONS

The aim of the work presented in this thesis was to produce a small robot which has the aim of reconnaissance and surveillance. The robot was designed to have an inexpensive jumping capability using CO₂ gas to overcome obstacles and have in-wheel suspension to survive falls and throwing impacts. The following sections sum up the work done and presents ideas for how to make the robot better.

5.1. Conclusions and Recommendations

Main challenge of this thesis was trying to keep the robot lightweight yet sturdy while keeping it within the budget. Unfortunately, when these three design paradigms contradict, and they contradict all the time, the author's decisions were based on keeping the costs down.

When realizing the conical wheel idea, the problems faced were limited by the practical reasons rather than the design itself. Width of the wheel could have been at least the half size, yet length **W** which is shown in Figure 5-1, was due to using off the shelf products. Designing a suitable bearing for the occasion would take too much time and cost too much money, whereas using already available products in the market just costs a few dollar. So for this first prototype; which is a proof of concept, standard linear bearings and RC car tires were used.

Ideally, instead of using linear bearings and using shaft keyways and a key to transmit the torque to the cone; a spline shaft and a bearing should have been used. Spline shaft option was eliminated due to financial reasons since the suppliers demanded extraordinary figures such as more 100€ for just a meter of spline shaft for low quantity orders. Same rule applies for the rubber manufacturers as well; they tend to turn down the small quantity orders as it does not worth the molding process

No coatings were used between the cones which led to the wear issues at the wheels, thus affecting the performance and increasing the sliding friction. To overcome this problem, another set of wheels with balls between the outer and the inner cones were designed yet did not manufactured due to time and financial constraints.

Decision of the transmitting of the locomotion power using timing belts worked quite well and despite the impacts the robot has taken, motor and its shaft has remained intact. Yet there are doubts about this design, since if a PCB were used instead of the prototyping board, thus emptying the space underneath the motors, this space would be dead zone and an obstacle on the way to reducing the weight.

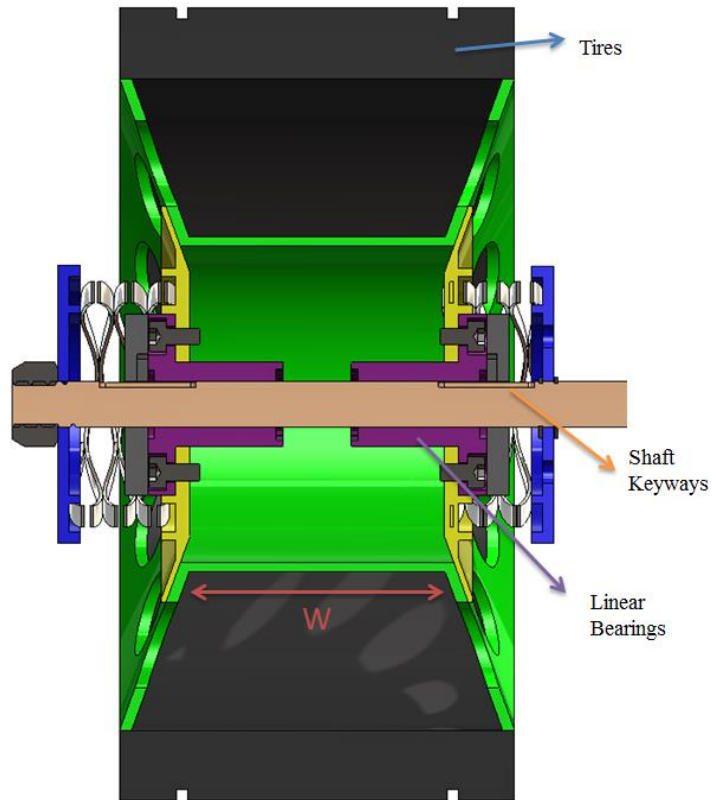


Figure 5-1: Main reason behind length L was the author's inability to develop his own linear bearings and his inability to find suitable tires for a smaller wheel

The problems about the jumping mechanism arose due to author's inexperience in the pneumatic design field and the uncertainties about the CO₂ cartridges. Most of the off the shelf seals are not suitable for 60 bar gas pressure as the author terribly observed. During the trials of the jumping mechanism, additional liquid seals had to be applied to the components again and again every time they are disassembled. Although very useful, as shown in Figure 5-2 it is quite messy.

Also as another remark, component geometries of the system had to be as simple as possible to lower the machining costs. As the system is a prototype, casting or manufacturing options which produces complex geometries economically, were not viable options.



Figure 5-2: Main joints of the hopping system are supported with liquid seal

5.2. Future Work and Recommendations

As this thesis focused on the low cost proof of concept of the robot, there is much room for optimization for the weight, in wheel suspension and jumping performance of this robot.

Weight could be lowered by utilizing more advanced engineering materials such as carbon fiber. Using higher voltages and selecting actuators with higher power density could also contribute to the weight reduction efforts. Wheels could be driven directly by torque motors, and to lower the weight two or three wheeled configuration may be more successful. The designed tilt mechanism adds up a lot of weight to the robot as well; just rotating the hopping actuator would require small motor and less components, thus reducing the weight.

Much of the concerns about the weight and the suspension are already delivered in the previous sections, yet the actual improvement area lies in the jumping mechanism. Much bigger cartridges can be used, for example 88g ones, and using better controlled valve multiple jumps could be achieved, and the jumps could be much more controlled. Also, instead of using carbon dioxide cartridges, dry ice (solid carbon dioxide) could be used, which is also readily commercially available. In addition to these, vapor pressure loss at cold temperatures could be compensated by wrapping heaters around the CO₂ cartridges, in an effort to increase the vapor pressure before jump.

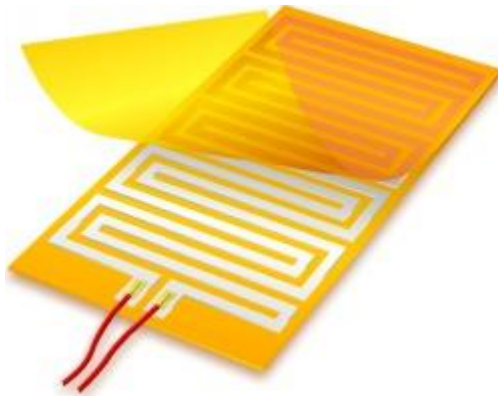


Figure 5-3: Heaters could be used to reliably jump at cold temperatures

Another potential for search and rescue use of the robot is to make it connectable to a large gas tank with a hose. If the robot is connected to a rather infinite supply, theoretically it can perform as many jumps as the user wants, assuming that electrical system is also connected with appropriate cabling. Much more efficient rescue operations could be performed in debris; while rescuers trying to detect the victims are perfectly safe

Also, more useful payloads could be attached to the robot to make it more versatile. Depth sensors or stereovision could be added for mapping the environment and identifying the surrounding objects.

REFERENCES

- [1] Allen G., "I, throwbot: U.S. Army set to test new lightweight and lobable cyber assistants in Afghanistan"
<http://www.dailymail.co.uk/sciencetech/article-2046107/Throwable-robots-U-S-Army-set-test-new-lightweight-cyber-assistants-Afghanistan.html>, Oct. 7 2011, [11 Jan. 2012]
- [2] Klobucar J., 2012, "ReconRobotics Awarded \$13.9 Million Contract by the U.S. Army", http://www.reconrobotics.com/contact/press_news_6-27-12.cfm, 27 Jun. 2012, [5 Jul. 2012]
- [3] Clements J., Kirkland L., "U//FOUO U.S. Army - Marine Corps Unmanned Ground Systems Presentation." <http://publicintelligence.net/AMCB-UGVs.pdf>, 12 Sep. 2011, [7 Nov. 2012]
- [4] Micire M., Murphy R., Casper J., "Issues in Intelligent Robots for Search and Rescue", SPIE Ground Vehicle Technology II, Apr. 2000, vol. 4, pp. 41-46.
- [5] Tsukagoshi, H., Tanaka, T., Sasaki, M., and Kitagawa, A., "Development of the Jump & Rotation Mobile Robot – 5th report: Improvement of the remote operation", Japan Society of Mechanical Engineers, Robotics and Mechatronics Division, No. 03-4, Paper Digests IP1-2F-A6, 2003.
- [6] "Basic module iSnoop® Throw it!"
http://www.optimes.net/index.php?option=com_content&view=article&id=106&Itemid=93&lang=en, [8 Mar. 2013]
- [7] "TOUGHBOT", <http://www.omnitech.com/pdf/TOUGHBOT.pdf>, [8 Mar. 2013]
- [8] "iRobot receives military order for FirstLook robots"
<http://investor.irobot.com/phoenix.zhtml?c=193096&p=irol-newsArticle&ID=1669434&highlight=1.5>, 6 Mar. 2012, [15 June 2012]
- [9] Won C., "Robotic Platform", US Patent 6263989, July 24, 2001.
- [10] Stoeter S. A., Papanikolopoulos N., "Kinematic Motion Model for Jumping Scout Robots", IEEE Transactions On Robotics, vol. 22, no. 2., 2006
- [11] Drenner A., Burt I., Dahlin T., Kratochvil B., McMillen C., Nelson B., Papanikolopoulos N., Rybski P.E., Stubbs K., Waletzko D., Yesin K.B.; "Mobility enhancements to the Scout robot platform", ICRA '02, Volume 1, May 2002, pp.1069 – 1074

- [12] "News: MacroUSA". <http://www.macrousa.com/index.php/news>, 16 May 2012, [21 Mar 2013]
- [13] Hambling D., "Anti-Pirate Robots to Board Hostile Ships", http://www.popularmechanics.com/technology/military/robots/anti-pirate-robots-to-board-hostile-ships-14227951?click=pm_latest, 29 Oct. 2012, [24 Dec 2012]
- [14] German J., "Hop to it: Sandia hoppers leapfrog conventional wisdom about robot mobility", http://www.sandia.gov/LabNews/LN10-20-00/hop_story.html, 23 Oct. 2000, [26 Feb. 2012]
- [15] Fischer G. J., Spletzer B., Marron L.C., Kuehl M.A., Feddema J.T., Martinez M.A., "Hopping Robot", US Patent 6,247,546, June 19, 2001.
- [16] Rizzi A.A., Murphy M.P., Giarratana J.J., Malchano M.D., Weagle C.A., Richburg C.A., "Hopping Robot", US Patent 2012/0259460 A1, Oct. 11, 2012.
- [17] "iRobot: FirstLook 110"
<http://www.irobot.com/us/robots/defense/firstlook/~//media/Files/Robots/Defense/FirstLook/iRobot-110-FirstLook-Specs.ashx>, [6 Apr. 2013]
- [18] "Throwbot XT With Audio",
http://www.reconrobotics.com/pdfs/Recon_Robotics_Throwbot_Audio_XT_10-12.pdf, [6 Apr. 2013]
- [19] "Armadillo Micro Unmanned Ground Vehicle",
<http://www.macrousa.com/pdf/armadillo.pdf>, [7 Apr. 2013]
- [20] "Sand Flea Jumping Robot"
http://www.bostondynamics.com/img/SandFlea%20Datasheet%20v1_0.pdf, [7 Apr 2013]
- [21] Lambrecht B. G. A., Horschler A. D., Quinn R. D. , "A Small, Insect-Inspired Robot that Runs and Jumps," ICRA '05, Barcelona, Spain, 2005, pp. 1240-1245.
- [22] R. H. Armour, "A Biologically Inspired Jumping and Rolling Robot," Bath, 2010.
- [23] Kim S.W., An S., Koh J.S., Noh K.C.M., "Flea-Inspired Catapult Mechanism for Miniature Jumping Robots," vol. 28, no. 5, 2012.
- [24] Zhao J., Xi N., Gao B., Mutka M.W., Xiao L., "Development of a Controllable and Continuous Jumping Robot," , Shangai, China, 2011.
- [25] Niiyama R., Nagakubo A., Kuniyoshi Y., "Mowgli: A Bipedal Jumping and Landing Robot with an Artificial Musculoskeletal System" , Rome, Italy, 2007.
- [26] Scarfogliero U., Stefanini C., Dario P., "Design and Development of the Long-Jumping "Grillo" Mini Robot" , Rome, Italy, 2007.
- [27] Dubowsky S., Plante J.S., Boston P., "Low Cost Micro Exploration Robots for Search and Rescue in Rough Terrain" , Gaithersburg, 2006.

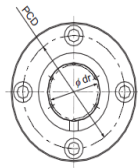
- [28] Evereft H.R., Rudakevychb P., Barnes M., "Throwbot: Design Considerations for a Man-Portable Throwable Robot", SPIE, Unmanned Ground Vehicle Technology VII, vol. 5804, 2005.
- [29] R. Salton J., Buerger S., Marron L., Feddema J., Fischer G., Little C., Spletzer B., Xavier P., A. A. Rizzi, M. P. Murphy, J. Giarratana, M. D. Malchano, C. A. Weagle, "Urban Hopper", SPIE, Unmanned Systems Technology, vol. 7692, 2010.
- [30] Louden B., "Non-Pneumatic Tyre Assembly", US Patent 8,091,596 B2, January 10, 2012.
- [31] Fischer G. J., "Wheeled Hopping Mobility", *SPIE*, Unmanned/Unattended Sensors and Sensor Networks II, vol. 5986, 2005.
- [32] "CO2 Terminal", www.globalccsinstitute.com, [22 Mar 2013]
- [33] ISO 6358, "Pneumatic fluid power - Components using compressible fluids - Determination of Flow-rate characteristics", 1989.
- [34] Fujita T., Kagawa T. Cai M.L., "The Available Energy Incoming in the Action of a Pneumatic Cylinder," *Journal of The Japan Fluid Power System Society*, vol. 33, no. 4, pp. 91-98, 2002.
- [35] Esposito A., "Fluid Power with Applications", Prentice-Hall, 1997.
- [36] Parmley R. O., "Illustrated Sourcebook of Mechanical Components", McGraw Hill, 2000.
- [37] "THK Model Uçak – 24V 3400mAh 25C Battery", <http://thkmodelucak.com/store/product/74v-3400-25c>, [23 Mar. 2013]
- [38] Digi International Inc., Rabbit RCM5400w OEM User Manual, 2008.
- [39] "Dynamic Data Display", <http://dynamicdatadisplay.codeplex.com/>, 13 Dec. 2011, 22 Jul 2013
- [40] "Lee Springs Redux Wave Springs Catalogue", <http://www.leespring.co.uk/downloads/uk/2012/WaveConstSprings.pdf>, [18 May 2013]

APPENDIX

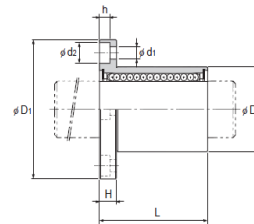
SELECTED PRODUCTS

A.1. Linear Bearings of the Cone Wheel and Piercing Mechanism

Model LMF



Model LMF

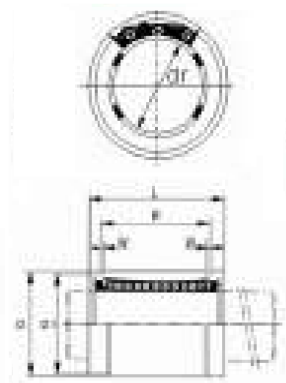


Selected bearing

Model No.	Standard type	Ball rows	Main dimensions						Flange perpendicularity	Eccentricity (max)	Radial clearance tolerance	Basic load rating					
			Inscribed bore diameter		Length		Flange diameter					Mounting hole	C	C ₀	Mass		
dr	Tolerance	D	Tolerance	L	Tolerance	D ₁	Tolerance	μm	μm	μm	N					N	g
LMF 6	4	6	12	0	19	0	28	0	5	20	3.4×6.5×3.3	12	12	-5	206	265	26.5
LMF 8	4	8	15	-0.011	24	0	32	0	5	24	3.4×6.5×3.3	12	12	-5	265	402	40
LMF 10	4	10	19	0	29	0	39	0	6	29	4.5×8×4.4	12	12	-5	313	549	78
LMF 12	4	12	21	-0.009	30	-0.2	42	0	6	32	4.5×8×4.4	12	12	-5	412	598	76
LMF 13	4	13	23	-0.013	32	0	43	0	6	33	4.5×8×4.4	12	12	-7	510	775	94
LMF 16	5	16	28	0	37	0	48	-0.2	6	38	4.5×8×4.4	12	12	-7	775	1180	134
LMF 20	5	20	32	0	42	0	54	0	8	43	5.5×9.2×5.4	15	15	-9	863	1370	160
LMF 25	6	25	40	-0.010	50	0	62	0	8	51	5.5×9.2×5.4	15	15	-9	980	1570	340
LMF 30	6	30	45	-0.016	64	0	74	0	10	60	6.6×11×6.5	15	15	-9	1570	2750	450
LMF 35	6	35	52	0	70	0	82	0	10	67	6.6×11×6.5	20	20	-13	1670	3140	795
LMF 40	6	40	60	0	80	0	96	0	13	78	9×14×8.6	20	20	-13	2160	4020	1054
LMF 50	6	50	80	-0.019	100	-0.3	116	0	13	98	9×14×8.6	20	20	-13	3820	7940	2200
LMF 60	6	60	90	-0.022	110	0	134	-0.3	18	112	11×17.5×10.8	25	25	-13	4710	10000	2960

Figure A-1.1: Selected Linear Bearing of the Wheel

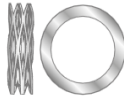
LM6 Linear Bearing



Number of Ball Rows	dr(mm)	D(mm)	B(mm)
4	6	12	13.5
D1(mm)	W(mm)	Cr(kgf)	Cor(kgf)
11.5	1.1	21	27
Weight(kg)	Material: Chrome steel (AISI52100).		
0.006			

Figure A-1.2: Selected Linear Bearing for the Piercing Mechanism

A.2. Wave Spring of the Cone Wheel



REDUX™ WAVE SPRINGS

● Stainless Steel 17-7 PH

LEE STOCK NUMBER	HOLE DIAMETER		ROD DIAMETER		NOMINAL LOAD		WORKING HEIGHT		FREE HEIGHT		WIRE THICKNESS X RADIAL WALL		TURNS	WAVES PER TURN	SPRING RATE		PRICE GROUP	
	MM	IN	MM	IN	N	LB	MM	IN	MM	IN	MM	IN			No.	No.		N/MM
LWM45 110 0991S	45.00	1.772	35.00	1.378	110.00	24.73	3.38	0.133	9.91	0.390	0.46 x 3.63	0.018 x 0.143	3	3.5	16.85	96.210	Y	
LWM45 110 1321S							4.52	0.178	13.21	0.520					4	12.66	72.290	Z
LWM45 110 1651S							5.64	0.222	16.51	0.650					5	10.12	57.780	BB
LWM45 110 1981S							6.76	0.266	19.81	0.780					6	8.43	48.130	BB
LWM45 110 2311S							7.90	0.311	23.11	0.910					7	7.23	41.280	BC
LWM45 110 2642S							9.02	0.355	26.42	1.040					8	6.32	36.090	BD
LWM45 110 2972S							10.16	0.400	29.72	1.170					9	5.62	32.090	BE
LWM45 110 3632S							12.40	0.488	36.32	1.430					11	4.60	26.270	BJ
LWM45 110 4293S							14.66	0.577	42.93	1.690					13	3.89	22.210	BM
LWM45 225 0991S							45.00	1.772	35.00	1.378					225.00	50.58	5.33	0.210
LWM45 225 1321S	6.99	0.275	13.21	0.520	4	36.16					206.470	Z						
LWM45 225 1651S	9.14	0.360	16.51	0.650	5	30.55					174.440	BB						
LWM45 225 1981S	10.80	0.425	19.81	0.780	6	24.95					142.460	BB						
LWM45 225 2311S	12.70	0.500	23.11	0.910	7	21.61					123.390	BC						
LWM45 225 2642S	14.48	0.570	26.42	1.040	8	18.85					107.630	BD						
LWM45 225 2972S	16.26	0.640	29.72	1.170	9	16.71					95.410	BE						
LWM45 225 3632S	19.81	0.780	36.32	1.430	11	13.63					77.830	BJ						
LWM45 225 4293S	23.37	0.920	42.93	1.690	13	11.50					65.660	BM						
LWM45 400 0991S	45.00	1.772	35.00	1.378	400.00	89.92					6.43	0.253	9.91	0.390			0.61 x 3.76	0.024 x 0.148
LWM45 400 1321S							8.38	0.330	13.21	0.520	4	82.88	473.240	Z				
LWM45 400 1651S							11.20	0.441	16.51	0.650	5	75.35	430.240	BB				
LWM45 400 1981S							17.95	0.510	19.81	0.780	6	58.33	333.060	BB				
LWM45 400 2311S							15.37	0.605	23.11	0.910	7	51.63	294.800	BC				
LWM45 400 2642S							17.27	0.680	26.42	1.040	8	43.74	249.750	BD				
LWM45 400 2972S							19.68	0.775	29.72	1.170	9	39.87	227.650	BE				
LWM45 400 3632S							24.26	0.955	36.32	1.430	11	33.15	189.280	BJ				
LWM45 400 4293S							28.45	1.120	42.93	1.690	13	27.63	157.760	BM				

Figure A-2: Selected Wave Spring of the Cone Wheel [40]

A.3. Rabbit 5400w Microcontroller Board Datasheet






Specifications	RCM5400W	RCM5450W	
Features			
Microprocessor	Rabbit® 4000 at 59 MHz		
Data SRAM	512K		
Program Execution Fast SRAM	512K	1 MB	
Flash Memory	512K	1 MB	
Serial Flash Memory	1 MB	2 MB	
Wi-Fi Compliance	802.11b/g standard, ISM 2.4 GHz		
Backup Battery Connection	Supports RTC and data SRAM		
General-Purpose I/O	Up to 39 parallel digital I/O lines configurable with 4 layers of alternate functions		
Additional Inputs	Startup mode (2), reset in		
Additional Outputs	Status, reset out		
External I/O Bus	Can be configured for 8 data lines and 6 address lines (shared with parallel I/O lines), plus I/O read/write		
Serial Ports	6 high-speed, CMOS-compatible ports: <ul style="list-style-type: none"> • All 6 configurable as asynchronous (with IrDA), 4 as clocked serial (SPI), and 2 as SDLC/HDLC • 1 asynchronous clocked serial port shared with programming port • 1 clocked serial port shared with serial flash 		
Serial Rate	Maximum asynchronous baud rate = CLK/8		
Slave Interface	Use the RCM5400W as an intelligent peripheral device slaved to a master processor		
Real Time Clock	Yes		
Timers	Ten 8-bit timers (6 cascadable from the first), one 10-bit timer with 2 match registers, and one 16-bit timer with 4 outputs and 8 set/reset registers		
Watchdog/Supervisor	Yes		
Pulse-Width Modulators	4 channels synchronized PWM with 10-bit counter 4 channels variable-phase or synchronized PWM with 16-bit counter		
Input Capture	2-channel input capture can be used to time input signals from various port pins		
Quadrature Decoder	Incremental encoder modules		
Power (pins unloaded)	3.3VDC ±5%; 625 mA @ 3.3V while transmitting/receiving; 175 mA @ 3.3V while not transmitting/receiving		
Operating Temperature	-30° C to +75° C		
Humidity	5% to 95%, non-condensing		
Connectors	One RP-SMA antenna connector; One 2 × 25, 1.27 mm pitch IDC signal header; One 2 × 5, 1.27 mm pitch IDC programming header		
Board Size	1.84" × 2.85" × 0.55" (47 mm × 72 mm × 14 mm)		
Wi-Fi			
	Region	802.11b	802.11g
Typical Average Antenna Output Power	Americas, Japan	19 dBm	15 dBm
	Other Regions	18 dBm	
Compliance	802.11b/g, 2.4 GHz		
Price (qty. 1); Part Number	\$119; 20-101-1246	\$134; 20-101-1247	
Development Kit; Part Number	\$299; U.S. and International (non-Japan): 101-1262; Japan: 101-1263		
<div style="display: flex; justify-content: space-around; align-items: flex-start;"> <div style="text-align: center;">  <p>RabbitWeb Easily create web interfaces to monitor and control embedded applications</p> </div> <div style="text-align: center;">  <p>Fat File System Popular, network-accessible file system for flash memories</p> </div> <div style="text-align: center;">  <p>Secure Socket Layer Industry standard web security for embedded applications</p> </div> <div style="text-align: center;">  <p>Rabbit Program Update Allows for remote firmware updates from anywhere in the world using an Internet connection</p> </div> <div style="text-align: center;">  <p>Wi-Fi Authentication Provides strongest Wi-Fi security available via WPA-2 and 802.11i</p> </div> </div> <p style="text-align: center; margin-top: 10px;">Visit www.digiembedded.com for part numbers.</p>			

Figure A-3: Datasheet of the Rabbit RCM5400w

A.4. Lipo Battery

23 03 2013

7,4V 3400 25C | THK Model Uçak

Anasayfa | Hakkımızda | Satın Alma Rehberi/Gizlilik | Müşteri Hizmetleri | Mağazalarımız Hakkında | SSS | İletişim

Hesabım

Üyelik

- Oturum Aç
- Üye Ol
- Şifremi Unuttum

Kategoriler

- + Model Uçaklar
- + Helikopterler
- + Radyo Kumandalar
- + Motorlar
- + Yakıtlar
- + Bataryalar
 - Lipo Bataryalar
 - Nicd NiMH Bataryalar
 - Sarj Aletleri
- + Giyim Hediye Eşyalar
- + Yapıştırıcılar-kımyasallar
- + Yedek Parça Ve Aksesuarlar
- + Statik Maketler
- + Kitaplar Ve Dergiler
- + Uçurtmalar

Sanal mağazamızdan alışveriş yapmak ve sipariş vermek çok kolaydır. Öncelikle mağazamıza üye olmanız gerekir. Üyelik ücretsizdir.



7,4V 3400 25C

63,00 TL

Stok Kodu : 15-01-0042

Stok Durumu : 10+

1

Sepete Ekle

Alışveriş Listeme Ekle



Özellikler

Açıklama

- *Ağırlığı:165gr
- *Ölçüleri:110x34x20mm

Tavsiyeler

*Bataryaları Mutlaka Uygun Şarj Aletleri ile Şarj Ediniz.

*Kendi Güvenliğiniz için mutlaka Kullanım kurallarına uyunuz.

Kullanılan elektrolitik içeriği açısından lityum-polimer piller diğer pillerden (NiCd, NiMH) farklılıklar gösterir. Bu gün piyasada bulunan pil hücrelerinde poliüretan veya poliüretandan yapılan süngerimsi ayrırcılar kullanılıyor. Bu süngerimsi yapının içi polimer ile dolduruluyor ve polimer hücrenin içine elektrolitik doldurulduğunda onu emerek jöle haline geliyor.

Lityum esaslı pillerin (li-po) raf ömrü kısadır. Saklama ömrünü uzatabilmek için , %40 dolu olarak 15 derece civarındaki sıcaklıkta saklanmalıdır. İleride kullanım deyip lityum esaslı pil almamak gerekir, kullanımsalar dahi, 2-3 yıl içinde işleri biter. Pilleri daha uzun ömürlü kullanmak için balanslı şarj aletleri ile şarj ediniz. Lityum piller hücre başına 3,70 volt olarak imal edilir. Lityum pillerin daha uzun yaşayabilmesi için şarj esnasında, hücre başına en fazla 4,20V geçmemelidir. 2,75V'un altına da asla düşürülmemelidir. Kapasitelerinin %80'inden fazlası kullanılmamalı. 60 derece çalışma sınırı aşılmamalı. Kullanım sonrası, her bir hücrenin gerilimi 3,70V yapıp 15 dereceden serin bir yerde, rutubetten koruyacak şekilde saklayınız.

İçerik

- * 1 Adet 4mm banana soketli 3400 mAh 25C 7.4V lipo batarya.

Etiketler

lipo

Figure A-4: Datasheet of the Lithium Polymer Battery from the THK Store

A.5. Motor Driver Datasheet

FEATURES

- Dual-H-Bridge Current-Control Motor Driver
 - Capable of Driving Two DC Motors or One Stepper Motor
 - Low MOSFET On-Resistance: HS + LS 360 mΩ
- Output Current (at $V_M = 5\text{ V}$, 25°C)
 - 1.5-A RMS, 2-A Peak per H-Bridge in PWP and RTY Package Options
 - 500-mA RMS, 2-A Peak per H-Bridge in PW Package Option
- Outputs Can Be Paralleled for
 - 3-A RMS, 4-A Peak (PWP and RTY)
 - 1-A RMS, 4-A Peak (PW)
- Wide Power Supply Voltage Range: 2.7 V – 10.8 V
- PWM Winding Current Regulation/Limiting
- Thermally Enhanced Surface Mount Packages (PWP and RTY)

APPLICATIONS

- Battery-Powered Toys
- POS Printers
- Video Security Cameras
- Office Automation Machines
- Gaming Machines
- Robotics

ELECTRICAL CHARACTERISTICS

$T_A = 25^\circ\text{C}$ (unless otherwise noted)

PARAMETER		TEST CONDITIONS	MIN	TYP	MAX	UNIT
POWER SUPPLY						
I_{VM}	VM operating supply current	$V_M = 5\text{ V}$, $xIN1 = 0\text{ V}$, $xIN2 = 0\text{ V}$		1.7	3	mA
I_{VMQ}	VM sleep mode supply current	$V_M = 5\text{ V}$		1.6	2.5	μA
V_{UVLO}	VM undervoltage lockout voltage	V_M falling			2.6	V
V_{HYS}	VM undervoltage lockout hysteresis			90		mV
LOGIC-LEVEL INPUTS						
V_{IL}	Input low voltage	nSLEEP			0.5	V
		All other pins			0.7	
V_{IH}	Input high voltage	nSLEEP	2.5			V
		All other pins	2			
V_{HYS}	Input hysteresis			0.4		V
R_{PD}	Input pull-down resistance	nSLEEP		500		kΩ
		All except nSLEEP		150		
I_{IL}	Input low current	$V_{IN} = 0$			1	μA
I_{IH}	Input high current	$V_{IN} = 3.3\text{ V}$, nSLEEP		6.6	13	μA
		$V_{IN} = 3.3\text{ V}$, all except nSLEEP		16.5	33	
t_{DEG}	Input deglitch time			450		ns
nFAULT OUTPUT (OPEN-DRAIN OUTPUT)						
V_{OL}	Output low voltage	$I_O = 5\text{ mA}$			0.5	V
I_{OH}	Output high leakage current	$V_O = 3.3\text{ V}$			1	μA
H-BRIDGE FETS						
$R_{DS(ON)}$	HS FET on resistance	$V_M = 5\text{ V}$, $I_O = 500\text{ mA}$, $T_J = 25^\circ\text{C}$		200		mΩ
		$V_M = 5\text{ V}$, $I_O = 500\text{ mA}$, $T_J = 85^\circ\text{C}$		325		
		$V_M = 2.7\text{ V}$, $I_O = 500\text{ mA}$, $T_J = 25^\circ\text{C}$		250		
		$V_M = 2.7\text{ V}$, $I_O = 500\text{ mA}$, $T_J = 85^\circ\text{C}$		350		
	LS FET on resistance	$V_M = 5\text{ V}$, $I_O = 500\text{ mA}$, $T_J = 25^\circ\text{C}$		160		
		$V_M = 5\text{ V}$, $I_O = 500\text{ mA}$, $T_J = 85^\circ\text{C}$		275		
		$V_M = 2.7\text{ V}$, $I_O = 500\text{ mA}$, $T_J = 25^\circ\text{C}$		200		
		$V_M = 2.7\text{ V}$, $I_O = 500\text{ mA}$, $T_J = 85^\circ\text{C}$		300		
I_{OFF}	Off-state leakage current	$V_M = 5\text{ V}$, $T_J = 25^\circ\text{C}$, $V_{OUT} = 0\text{ V}$	-1		1	μA
MOTOR DRIVER						
f_{PWM}	Current control PWM frequency	Internal PWM frequency		50		kHz
t_R	Rise time	$V_M = 5\text{ V}$, $16\ \Omega$ to GND, 10% to 90% V_M		180		ns
t_F	Fall time	$V_M = 5\text{ V}$, $16\ \Omega$ to GND, 10% to 90% V_M		160		ns
t_{PROP}	Propagation delay INx to OUTx	$V_M = 5\text{ V}$		1.1		μs
t_{DEAD}	Dead time ⁽¹⁾	$V_M = 5\text{ V}$		450		ns
PROTECTION CIRCUITS						
I_{OCP}	Overcurrent protection trip level		2	3.3		A
t_{DEG}	OCP Deglitch time			2.25		μs
t_{OCP}	Overcurrent protection period			1.35		ms
t_{TSD}	Thermal shutdown temperature	Die temperature	150	160	180	$^\circ\text{C}$

Figure A-5: Datasheet of Texas Instruments DRV8833

A.6. Ocean Server OS5000-S Compass Datasheet

Parameter	Value
Azimuth accuracy	<0.5 deg RMS, 0.1 deg resolution
Inclination (pitch and roll) accuracy	< 1 deg, 0.1 deg resolution
Inclination range	+/- 80 degrees, (output for full rotation at decreased accuracy pitch +/- 90 degrees, roll +/- 180 degrees)
Temperature range	-40C to +85C operating, Humidity: 20-80% RH non-condensing
Shock (Operating)	3,000 G, 0.5 ms, 10,000 G 0.1ms
Data Refresh Rate	0.01 Hz to 40Hz sentence output rate
Size	1" x 1" x 0.3" module
Weight	~ 2 grams
Supply Voltage	3.3V – 5VDC (Will operate with up to 15VDC using 3x the power)
Power consumption	30 ma @3.3V (-S variant) 35 ma @5V (-US variant, in USB mode)
Serial Data Interface	RS-232C levels, TTL and USB 2.0 based on Variant 4800 – 115000 baud, 8 bit, 1 stop, no parity (19200 default)
Sentence Format	NMEA0183 Style, four sentence formats, supporting xor parity (\$HCHDT, \$OHPR, \$C, comma delimited. Supports Acceleration & Magnetic sensor output in X,Y,Z
Magnetic Compensation Routines	Hard Iron and Soft Iron calibrations supported, note: Soft iron (V1.4 or later firmware)

Figure A-6: Specifications of the OS5000-S